

CHEMISTRY-TRANSPORT COUPLING IN FLAME  
DYNAMICS AND EMISSIONS

SILI DENG

A DISSERTATION  
PRESENTED TO THE FACULTY  
OF PRINCETON UNIVERSITY  
IN CANDIDACY FOR THE DEGREE  
OF DOCTOR OF PHILOSOPHY

RECOMMENDED FOR ACCEPTANCE  
BY THE DEPARTMENT OF  
MECHANICAL AND AEROSPACE ENGINEERING  
ADVISERS: PROFESSOR CHUNG K. LAW  
PROFESSOR MICHAEL E. MUELLER

SEPTEMBER 2016

© Copyright by Sili Deng, 2016.

All rights reserved.

## Abstract

Chemical kinetics and fluid dynamics are crucial components of combustion, governing the efficiency, stability, and emissions of many practical combustion devices. Particularly, this dissertation advances the understanding of the coupling effects between chemical kinetics and transport in flame dynamics (Chapters 2 and 3) and soot emissions (Chapters 4 and 5) at engine relevant conditions. For both topics, foundational studies on chemical kinetics were first carried out in relatively simple, laminar, low-dimensional configurations with well characterized flow fields to understand low-temperature cool flame chemistry and soot chemistry. Complexities from flows were then considered, and chemistry-transport coupling was investigated at engine relevant conditions to elucidate the role of low-temperature chemistry in autoignition-affected flame dynamics and the role of hydrogen addition in soot evolution in bluff body flames, leveraging the understanding obtained in the chemical kinetics studies.

The first half of this dissertation focuses on low-temperature chemistry and its role in flame dynamics. Specifically, in Chapter 2, experimental studies, supported by computations, were conducted on the coupling of low-temperature chemistry and transport in the ignition, extinction, and associated steady burning in nonpremixed DME/air counterflow flames. The presence of low-temperature chemical reactivity was detected nonintrusively, and the ignition temperature was determined subsequently. At elevated pressures, which promote low-temperature chemistry, the hysteresis in ignition and extinction behavior of nonpremixed cool flames was observed and quantified for the first time. The thermal and chemical structure of the cool flame was computationally analyzed to elucidate the dominant chemical pathways during the ignition and extinction processes. Effects of strain rate, fuel and oxygen concentration, and ambient pressure on the cool flame were investigated. Possible reasons for the discrepancies between experiments and computations were discussed to fa-

cilitate further cool flame studies and the development of low-temperature chemical models.

The role of low-temperature chemistry in autoignition-affected flame dynamics was then computationally investigated in Chapter 3. Laminar nonpremixed DME/air coflow flames were investigated at elevated temperatures and pressures with various boundary temperatures and velocities. The stabilization mechanism for steady flames and the flame dynamics for the forced oscillating cases were analyzed. Besides the tribrachial structure typically observed at nonautoignitive conditions, a multibrachial thermal structure was observed due to autoignition. Consequently, a stabilization regime diagram was proposed, including frozen flow, kinetically stabilized (autoignition), autoignition-propagation-coupled stabilized, kinematically stabilized (tribrachial flame), and burner stabilized regimes. The transition of the combustion mode was elucidated through the computational investigations of sinusoidally forced oscillating cases. Transition between a multibrachial autoignition front and a tribrachial flame occurs periodically and exhibited a hysteresis. First-stage low-temperature chemistry is less affected by flow dynamics with only second-stage autoignition and flame chemistry, which accounts for the majority of the heat release, coupled with flow oscillation. The understanding of the role of low-temperature chemistry in flame dynamics under laminar autoignitive conditions lays the foundation for future studies at turbulent conditions in practical engines.

The second half of this dissertation focuses on soot emissions. To understand the fuel effects on soot chemistry, in Chapter 4, the sooting limits of nonpremixed *n*-heptane, *n*-butanol, and methyl butanoate flames were determined experimentally in a liquid pool stagnation-flow configuration. In addition, complementary simulations with detailed polycyclic aromatic hydrocarbon (PAH) chemistry and a detailed soot model, based on the Hybrid Method of Moments (HMOM), were performed and compared with the experimental critical strain rates for the sooting flames. Argon

dilution was used to keep the thermal environment for the three fuel cases nearly the same to elucidate the chemical effects. Both experiment and simulation showed that *n*-heptane and *n*-butanol had similar sooting characteristics, while methyl butanoate had the least sooting propensity. Further sensitivity and reaction pathway analysis demonstrated that the three fuels share similar PAH chemical pathways, and C<sub>5</sub> and C<sub>6</sub> ring formation from the intermediate chain species was found to be the rate-limiting step. The differences in sooting propensity were due to the role of fuel bounded oxygen and the fuel breakdown processes. The findings in this chapter provide guidance to the design of diesel/biofuel blendings to reduce soot emissions.

Finally, in Chapter 5, the evolution of soot in a turbulent nonpremixed bluff body ethylene/hydrogen flame was investigated using a combination of experiments and Large Eddy Simulations and compared with a neat ethylene counterpart. With hydrogen addition, the maximum soot volume fractions in the recirculation zone and jet-like region significantly decreased. Flamelet calculations demonstrated that hydrogen addition suppressed soot formation due to the reduction of the C/H ratio, resulting in an estimated fourfold reduction in soot volume fraction due to chemical effects. Soot reduction in the downstream jet-like region of the flame was quantitatively consistent with this chemical effect. However, soot reduction in the recirculation zone was substantially larger than this analysis suggests, indicating an additional hydrodynamic effect. Large Eddy Simulation was used to further investigate soot evolution in the recirculation zone and to elucidate the role of hydrogen addition. For the same heat release rate and similar jet Reynolds number as the neat ethylene case, the addition of hydrogen required a higher jet velocity, and this led to a leaner recirculation zone that inhibited soot formation and promoted soot oxidation. The findings in this chapter further validated the comprehensive soot model for turbulent sooting flames and advanced the understanding of soot evolution in recirculating flows.

## Acknowledgements

My Ph.D. journey would not have begun without the support of parents. They are my first and best teachers in my life, who have demonstrated the courage to face challenges, perseverance through hard times, and pursuit of excellence. This dissertation is dedicated to my parents and family for their belief in me.

I have been very fortunate to join Law Combustion Group and work closely with Professor Chung K. Law. I am always amazed by his dedication to work and the breadth and depth of his research. He is a great scholar who taught me to appreciate the beauty of science, conduct rigorous research, and take initiative. He has brought out the best in me through daily discussions about my research progress, introducing internal and external research resources to me, and exposing me to networking opportunities. To help me develop a computational skillset, he recommended that I join the Computational Turbulent Reacting Flow Laboratory and be co-advised by Professor Michael E. Mueller since my fourth year in graduate school. I am very grateful for his thoughtful suggestions on my career development.

I truly appreciate the patience and guidance that Professor Michael E. Mueller has given to me along my endeavor. He spent a tremendous amount of time passing on his knowledge and skills to me and holding my hand to get me started in computational research as soon as possible. The freedom and trust he has given to me allows me to consolidate what I have learnt in both groups, master new tools, and propel my research in new directions. I am also very thankful for him generously sharing his experience with me on pursuing a job in academia and establishing a research group, which will benefit my future career.

It has been a privilege to pursue my Ph.D. degree in such an intellectually challenging and nourishing environment, the Department of Mechanical and Aerospace Engineering at Princeton University. I would like to thank the faculty, staff, and my peers in the department for their guidance, support, and companionship throughout

the years. Specifically, I am very grateful to Professors Harvey Lam and Alexander Smits for helping me prepare for my general examinations, and Professors Daniel Nosenchuck, Yiguang Ju, Craig Arnold, and Frederick Dryer for serving as my general examiners. Furthermore, I would like to thank my Ph.D. committee members, Professors Yiguang Ju and Marcus Hultmark for their advice over the years. I am particularly thankful to Professors Suk Ho Chung and Yiguang Ju for their feedback and suggestions to improve this dissertation.

My colleagues in LCG and CTRFL have helped me transition from a little sister who seeks for support and suggestions to a big sister who can finally give back to the group. I would not have mastered the counterflow experiments so quickly without the assistance of Dr. Wei Liu, Mr. Jeremy Koch, and Professor Peng Zhao. They have not only passed on their knowledge and experience to me but also made themselves available through phone calls whenever I need their opinions. Mr. Delin Zhu, the lab manager of LCG, more generally known as the lab magician, allows me to quickly try out new ideas and always amazes me with his masterpiece designs. I have also enjoyed collaborating with Professor Dong Han, Mr. Wenkai Liang, and Dr. Fujia Wu on chemical kinetics. I am indebted to my colleagues, who keep me company while doing experiments at night, challenge me during group meetings, proofread my manuscripts, help me debug programs, give me feedback during presentation rehearsals, share thoughts about research and life with me, and engage me in group activities. I have had to walk through this Ph.D. journey by myself, but I know that I am not all by myself.

I have been very fortunate to have the opportunity to collaborate with many outstanding researchers outside Princeton University during my Ph.D. study: Professor Qing Chan at the University of New South Wales, Dr. Nader Qamar at FCT-Combustion, Professors Bassam Dally, Zeyad Alwahabi, and Graham Nathan at the University of Adelaide, and Professor Zhen Huang at Shanghai Jiao Tong University.

I would also like to acknowledge several faculty and friends for the helpful discussions and technical support during my first research project on nonpremixed cool flames. The discussions with Professor Richard Miles in MAE, Professor Claire Gmachl in EE, and Professor Marshall Long at Yale University were very helpful for the design of the detection system. I am very grateful to Dr. Ben Wu in EE for lending me optical detectors, filters, and cables, Dr. Yu Song in EE for helping me implement the infrared camera, and Dr. Jun Xiong in Physics for helping me with the LABVIEW program for automatic control.

Finally, this thesis would not be possible without the financial support of Combustion Energy Frontier Research Center, funded by the U.S. Department of Energy, and Air Force Office of Scientific Research. I would also like to acknowledge additional support from Princeton Climate and Energy Scholarship and Gordon Wu Prize for Excellence. This dissertation carries T-3327 in the records of the Department of Mechanical and Aerospace Engineering.

# Contents

Abstract . . . . .	iii
Acknowledgements . . . . .	vi
List of Tables . . . . .	xii
List of Figures . . . . .	xiii
<b>1 Introduction</b>	<b>1</b>
1.1 Chemistry-Transport Coupling in Flame Dynamics . . . . .	2
1.1.1 Low-Temperature Chemistry and Cool Flames . . . . .	3
1.1.2 LTC in Nonpremixed Flames . . . . .	4
1.1.3 Nonpremixed Flame Stabilization and Oscillation . . . . .	6
1.1.4 LTC in Flame Stabilization . . . . .	8
1.2 Chemistry-Transport Coupling in Soot Emissions . . . . .	10
1.2.1 Soot Mechanisms and Emissions . . . . .	10
1.2.2 Role of Fuel Structure in PAH Chemistry and Soot Emissions	12
1.2.3 Combined Role of Fuel and Turbulence in Soot Emissions . .	14
1.3 Organization of the Dissertation . . . . .	16
<b>2 Nonpremixed Counterflow Cool Flames</b>	<b>19</b>
2.1 Experimental Investigation . . . . .	19
2.2 Computational Investigation . . . . .	22
2.3 Nonpremixed Cool Flames at Atmospheric Conditions . . . . .	24

2.3.1	Identification of the Cool Flame . . . . .	24
2.3.2	Determination of Ignition Temperature . . . . .	27
2.4	Nonpremixed Cool Flames at Elevated Pressure . . . . .	32
2.4.1	Improvement of the Experimental Methodology . . . . .	32
2.4.2	Hysteretic Ignition and Extinction Behavior . . . . .	33
2.4.3	Analysis of Thermal and Chemical Structures . . . . .	37
2.4.4	Uncertainty Analysis . . . . .	42
2.4.5	Effects of Pressure and Oxygen Concentration . . . . .	45
2.5	Summary . . . . .	49
<b>3</b>	<b>Flame Dynamics at Engine Conditions</b>	<b>52</b>
3.1	Computational Details . . . . .	53
3.2	Flame Stabilization: Boundary Temperature Effects . . . . .	55
3.2.1	Thermal and Chemical Structure . . . . .	55
3.2.2	Computational Diagnostics and Analysis . . . . .	61
3.2.3	Stabilization Mechanism . . . . .	70
3.3	Flame Stabilization: Boundary Velocity Effects . . . . .	72
3.3.1	Thermal and Chemical Structure . . . . .	73
3.3.2	Stabilization Mechanism . . . . .	76
3.3.3	Autoignition and Flame Interaction . . . . .	77
3.3.4	Stabilization Regime Diagram . . . . .	82
3.4	Flame Dynamics in Oscillating Flows . . . . .	83
3.4.1	Thermal Structure . . . . .	84
3.4.2	Differentiation of Combustion Mode . . . . .	85
3.4.3	Effects of Oscillation Frequency . . . . .	91
3.5	Summary . . . . .	97

<b>4 Sooting Limits of Laminar Stagnation-Flow Flames</b>	<b>99</b>
4.1 Experimental Methodology . . . . .	100
4.2 Computational Methodology . . . . .	102
4.2.1 Chemical Model . . . . .	103
4.2.2 Soot Model . . . . .	106
4.3 Results: Sooting Limits . . . . .	110
4.4 Mechanistic Analysis . . . . .	111
4.4.1 Volume Fraction Response to Strain Rate . . . . .	112
4.4.2 Sensitivity and Reaction Pathway Analysis . . . . .	113
4.4.3 Rate-Limiting Steps for PAH Formation . . . . .	116
4.5 Summary . . . . .	117
<b>5 Soot Evolution in Turbulent Bluff Body Flames</b>	<b>121</b>
5.1 Experimental Methodology . . . . .	122
5.2 Computational Methodology . . . . .	123
5.3 Results and Discussion . . . . .	126
5.3.1 Overall Flame Structure . . . . .	126
5.3.2 Effects of Hydrogen Addition . . . . .	128
5.4 Summary . . . . .	134
<b>6 Conclusions</b>	<b>137</b>
6.1 Major Contributions . . . . .	137
6.1.1 Characterization of Nonpremixed Cool Flames . . . . .	137
6.1.2 Demonstration of Autoignition-Affected Flame Dynamics . . . . .	139
6.1.3 Characterization of Nonpremixed Sooting Limits . . . . .	142
6.1.4 Demonstration of Hydrogen-Affected Soot Emissions . . . . .	143
6.2 Recommendations for Future Work . . . . .	144
<b>Bibliography</b>	<b>148</b>

# List of Tables

3.1	Computational domain and number of grid points for steady cases with the same flow velocities but different boundary temperatures . . . . .	57
3.2	Computational domain and number of grid points for steady cases with the same boundary temperature but different flow velocities. . . . .	72
3.3	Induction time at different harmonic oscillation frequencies. The defi- nition of the induction time is illustrated in Fig. 3.21 . . . . .	95
4.1	Oxidizer stream composition in mole fractions to maintain the same adiabatic flame temperature of the three fuels with the same oxygen concentration in the oxidizer stream. . . . .	102

# List of Figures

1.1	Figure 8 in Law and Zhao [82]. The global response S-curve plotted as maximum temperature versus air-side boundary temperature. The strain rate varies from 20 to 100 to 200 /s, and the pressure is 1 atm.	5
1.2	A schematic plot of the tribrachial flame structure in a coflow mixing layer. . . . .	6
1.3	A schematic drawing of the physical and chemical processes that govern soot evolution. . . . .	11
1.4	Transmission electron microscopy (TEM) images of soot aggregate from Jensen <i>et al.</i> [67]. . . . .	12
2.1	Schematic of the nonpremixed DME/air counterflow system for the detection of cool flames and quantification of the cool flame ignition temperatures. . . . .	21
2.2	Schematic of the nonpremixed counterflow configuration for S-curve analysis. . . . .	23
2.3	“M” shaped signal observed with the PMT-oscilloscope system from the counterflow chamber at atmospheric pressure. The fuel stream consists of 30% DME and 70% nitrogen, and the oxidizer is air. a. Switch Air/DME to Air/N <sub>2</sub> ; b. Switch Air/N <sub>2</sub> to Air/DME; c. Switch Air/DME to N <sub>2</sub> /DME; d. Switch N <sub>2</sub> /DME to Air/DME. . .	25

2.4	Formaldehyde chemiluminescence intensity at different air boundary temperatures under various strain rates. . . . .	26
2.5	Maximum formaldehyde mole fraction of 30% DME at different air boundary temperatures under various strain rates. . . . .	27
2.6	A/B: Heated air/ $N_2$ against DME counterflow IR images at ignition (atmospheric pressure, strain rate 60 /s); C/D: Difference between A/B and B. . . . .	28
2.7	Calculated and observed ignition temperatures of 30% DME under various strain rates at atmospheric pressure. . . . .	29
2.8	Sensitivity analysis on low and high strain rate cases at atmospheric pressure: DME mole fraction is 30%. . . . .	30
2.9	Ignition temperatures of various DME concentrations under the strain rate of 60 /s at atmospheric pressure. . . . .	31
2.10	S-curve analysis of the response of nonpremixed counterflow of 50% DME and 50% nitrogen versus heated air at the 2 atm and pressure-weighted strain rate of 80 /s. . . . .	35
2.11	Flame images demonstrating the hysteretic nature of ignition and extinction of cool flames with air temperature. DME cool flame at 2 atm and pressure-weighted strain rate of 84 /s; DME volume fraction in the fuel stream is 50%, and the oxidizer stream is air. . . . .	36
2.12	Experimental and computed ignition and extinction temperatures at 2 atm and various strain rates. The computed extinction temperature is shifted up by 250 K for better illustration. DME volume fraction in the fuel stream is 50%, and the oxidizer stream is air. . . . .	37
2.13	Thermal structures in the computed flow field at three representative points on the S-curve shown in Fig. 2.10. Fuel stream boundary conditions are specified at $x = 0$ in the computation. . . . .	38

2.14 Species profiles in the computed flow field at three representative points on the S-curve shown in Fig. 2.10: methoxymethylperoxy radical. Fuel stream boundary conditions are specified at $x = 0$ in the computation.	40
2.15 Species profiles in the computed flow field at three representative points on the S-curve shown in Fig. 2.10: formaldehyde. Fuel stream boundary conditions are specified at $x = 0$ in the computation. . . . .	41
2.16 Species profiles in the computed flow field at three representative points on the S-curve shown in Fig. 2.10: hydroxyl radical. Fuel stream boundary conditions are specified at $x = 0$ in the computation. . . . .	42
2.17 Reaction sensitivity analysis at three representative points on the S-curve shown in Fig. 2.10. . . . .	43
2.18 Revisit of Fig. 2.12 with modified reaction rates in the chemical mechanism. Note that the line plots with the modified reaction rates are presented without shifting. . . . .	44
2.19 S-curve analysis for various ambient pressures and pressure-weighted strain rate of 100 /s. DME volume fraction in the fuel stream is 50%, and the oxidizer stream is air. . . . .	46
2.20 Ignition and extinction temperatures at various strain rates and pressures in experiments and computations with the original chemical model. Some of the computed extinction temperatures are shifted up for better illustration. DME volume fraction in the fuel stream is 50%, and the oxidizer stream is air. . . . .	47
2.21 Ignition and extinction temperatures at various strain rates and pressures in experiments and computations with the modified chemical models. Some of the computed extinction temperatures are shifted up for better illustration. DME volume fraction in the fuel stream is 50%, and the oxidizer stream is air. . . . .	48

2.22 S-curve analysis for various oxygen concentrations and the pressure-weighted strain rate of 100 /s. DME volume fraction in the fuel stream is 50%, and the ambient pressure is 2 atm. . . . .	49
2.23 Ignition and extinction temperatures at various strain rates and oxygen concentrations in experiments and computations with the original chemical model. Some of the computed extinction temperatures are shifted up for better illustration. DME volume fraction in the fuel stream is 50%, and the ambient pressure is 2 atm. . . . .	50
2.24 Ignition and extinction temperatures at various strain rates and oxygen concentrations in experiments and computations with the modified chemical models. Some of the computed extinction temperatures are shifted up for better illustration. DME volume fraction in the fuel stream is 50%, and the ambient pressure is 2 atm. . . . .	51
3.1 A schematic of the coflow configuration adopted in all of the steady and unsteady cases. . . . .	53
3.2 Velocity, temperature, and $H_2O_2$ profiles along $Z_{st}$ on the nominal and two times coarser (in each direction) meshes for an air temperature of 800 K. . . . .	56
3.3 Heat release rate [ $J/m^3\cdot s$ ] profiles for the steady cases with the same flow velocities but different boundary temperatures. The iso-contours of $Z_{st}$ , $Z = 0.2$ , and $Z = 0.3$ are outlined from right to left in solid lines, respectively. The CEMA sampling points at 800 and 1100 K are indicated along the iso-contours. . . . .	57
3.4 A schematic of the thermal structure of the 800 K case. LPF, RPF, and NPF denotes the lean premixed, rich premixed, and nonpremixed flame branches on the tribrachial structure, respectively. LB and RB denotes the leaner and richer branches of the reacting front, respectively.	58

3.5	Hydroxyl (OH) radical mass fraction profiles for the steady cases with the same flow velocities but different boundary temperatures. The mixture fraction iso-contours are the same as in Fig. 3.3. . . . .	60
3.6	Methoxymethylperoxy ( $\text{CH}_3\text{OCH}_2\text{O}_2$ ) radical mass fraction profiles for the steady cases with the same flow velocities but different boundary temperatures. The mixture fraction iso-contours are the same as in Fig. 3.3. . . . .	60
3.7	Hydroperoxyl ( $\text{HO}_2$ ) radical mass fraction profiles for the steady cases with the same flow velocities but different boundary temperatures. The mixture fraction iso-contours are the same as in Fig. 3.3. . . . .	61
3.8	Hydrogen peroxide ( $\text{H}_2\text{O}_2$ ) mass fraction profiles for the steady cases with the same flow velocities but different boundary temperatures. The mixture fraction iso-contours are the same as in Fig. 3.3. . . . .	61
3.9	Normalized participation index at 800 K and 1100 K. Sampled locations are indicated in Fig. 3.3. . . . .	63
3.10	$\frac{\chi(Z)}{f(Z; Z_{\text{st}})}$ , using Eq. 3.6, from the two-dimensional calculations at 800 K.	68
3.11	Comparison between 2D-CFD and 1D-LFA results for the steady cases with the same flow velocities but different boundary temperatures. . . . .	69
3.12	Extended regimes of the stabilization mechanism as the coflow boundary temperature increases. . . . .	72
3.13	Heat release rate [ $\text{J}/\text{m}^3\text{-s}$ ] profiles for steady cases with the same boundary temperature but different flow velocities. The iso-contours of $Z_{\text{st}}$ , $Z = 0.2$ , and $Z = 0.3$ are outlined from right to left in solid lines, respectively. The CEMA sampling points for 2.4 and 8.0 m/s cases are marked along the iso-contours. . . . .	73
3.14	Normalized participation index at 2.4 and 8.0 m/s. Sampled locations are delineated in Fig. 3.13. . . . .	75

3.15 Comparison between 2D-CFD and 1D-LFA results for the steady cases with the same boundary temperature but different flow velocities. . . . .	76
3.16 LFA profiles along $Z_{st}$ , $Z = 0.2$ , and $Z = 0.3$ of the 8.0 m/s case. . . . .	79
3.17 LFA results on the mixture fraction dependent total and first stage ignition delay times of the 8.0 m/s case. . . . .	81
3.18 A qualitative regime diagram for the stabilization mechanisms as the boundary temperature and inlet velocity vary. . . . .	82
3.19 Heat release rate [W/m <sup>3</sup> ] profile evolution during one oscillation cycle at 100 Hz. The iso-contours of $Z_{st} = 0.1$ , $Z = 0.2$ , and $Z = 0.3$ are outlined from right to left in solid lines, respectively. . . . .	84
3.20 Normalized displacement velocity (red) and leading point location (blue) time history profiles at 100 Hz. . . . .	87
3.21 Normalized displacement velocities at various inlet velocities for two steady cases and the 100 Hz oscillating unsteady cases. . . . .	89
3.22 Comparison of hydrogen peroxide mass fraction profiles along the $Z = 0.14$ and $Z = 0.24$ iso-contours at steady state and at 100 Hz during the decreasing-velocity cycle (left) and increasing-velocity cycle (right). .	90
3.23 Normalized leading point location time history profiles at 25, 50, and 100 Hz. . . . .	93
3.24 Normalized displacement velocities at various inlet velocities for four steady cases and three oscillating unsteady cases at different frequencies. Induction periods for the unsteady cases can also been defined similar to Fig. 3.21 but are not shown here for clarity. . . . .	94
3.25 Temperature, methyoxyethylperoxy radical, and hydrogen peroxide mass fraction profiles along the $Z = 0.24$ iso-contour at 3.2 m/s. DV: decreasing-velocity, and IV: increasing-velocity. . . . .	98

4.1	Schematic of the liquid pool stagnation-flow apparatus [91]. The heating system was not activated in the current study. . . . .	101
4.2	Mechanism validation of <i>n</i> -butanol laminar flame speeds, against the experimental (symbols) and computational (dotted lines) results from Liu <i>et al.</i> [88]. $P = 1$ atm and $T = 353$ K. . . . .	105
4.3	Mechanism validation of methyl butanoate laminar flame speeds, against the experimental (symbols) and computational (dotted lines) results from Liu <i>et al.</i> [88]. $P = 1$ atm and $T = 353$ K. . . . .	106
4.4	Mechanism validation for <i>n</i> -heptane against the extinction strain rates measurements in nonpremixed stagnation-flow systems. . . . .	107
4.5	Mechanism validation for <i>n</i> -butanol against the extinction strain rates measurements in nonpremixed stagnation-flow systems. . . . .	108
4.6	Mechanism validation for methyl butanoate against the extinction strain rates measurements in nonpremixed stagnation-flow systems. .	109
4.7	Temperature (solid line) and $f_V$ (dash-dotted line) profiles at the strain rate of $16\text{ s}^{-1}$ and $X_{O_2} = 0.2$ . . . . .	112
4.8	Experimental (symbols) and computational (lines) CSRs. . . . .	113
4.9	The responses of the integrated $f_V$ to strain rate at $X_{O_2} = 0.2$ . . . . .	114
4.10	Sensitivity of the maximum naphthalene mass fraction to kinetics at the strain rate of $16\text{ s}^{-1}$ and $X_{O_2} = 0.2$ . Top: Intermediate chain radical reactions. Bottom: Ring formation reactions. . . . .	118
4.11	Chemical pathways for naphthalene formation at the strain rate of $16\text{ s}^{-1}$ and $X_{O_2} = 0.2$ . . . . .	119
4.12	Fuel specific pathways for $C_3H_6$ and $A-C_3H_5$ formation at the strain rate of $16\text{ s}^{-1}$ and $X_{O_2} = 0.2$ . From left to right: <i>n</i> -heptane, <i>n</i> -butanol, and methyl butanoate. The numbers indicate the relative contribution (in percentages) to the formation of the “downstream” species. . . . .	119

4.13 Key intermediate species profiles at low strain rates ( $16 \text{ s}^{-1}$ ) and CSRs:	
$X_{O_2} = 0.2$ . . . . .	120
5.1 Photographs of the neat ethylene (left) and ethylene/hydrogen (right) bluff body flame and the corresponding collages of the time-averaged LII images of the soot volume fraction distribution. Three distinct regions are identified as follows: RZ (recirculation zone), NZ (neck zone), and JZ (jet-like zone). . . . .	127
5.2 Total soot volume per unit height obtained from the radial integration of the time-averaged soot volume fraction from the LII measurements at each height. For clarity, only every second measurement point is shown. . . . .	128
5.3 PAH mass fraction profiles calculated with steady flamelets at $\chi = 1 \text{ s}^{-1}$ . . . . .	129
5.4 Radial profiles of the time-averaged soot volume fraction. Only every fourth experimental measurement point is shown for clarity. The ethylene flame is reproduced from [107], and the ethylene/hydrogen flame is from this work. Both experimental and computational results for the ethylene/hydrogen flame are scaled up by a factor of ten. . . . .	131
5.5 Streamlines in the recirculation zone of the neat ethylene flame (top) and ethylene/hydrogen flame (bottom) in the LES. . . . .	132
5.6 Top: radial profile of the time-averaged mixture fraction in the LES at different heights. Black horizontal lines correspond to the stoichiometric mixture fractions of these two flames and almost overlap. Bottom: characteristic inverse time scales of the soot processes from the steady flamelet calculations at $\chi_{\text{st}} = 1 \text{ s}^{-1}$ . Vertical lines correspond to the mixture fraction in the flat regions of the radial plot. . . . .	133

5.7 Time-averaged soot volume fraction source term [ppm/s] in the recirculation zone of the ethylene/hydrogen flame in the LES. The magenta lines correspond to the stoichiometric mixture fraction contours. . . . 135

# Chapter 1

## Introduction

The utilization of combustion has been a crucial part of civilization. From an engineering point of view, the efficiency, reliability, and emissions of combustion processes are still to be further improved. The combustion processes in a gas turbine engine, for example, involve fuel and air mixing, stabilization of the flame, and emissions of incomplete combustion products and nitrogen oxides. From a fundamental research point of view, understanding and optimizing each of these processes to achieve high-efficiency low-emission combustion is not trivial. This is due to the fact that combustion is interdisciplinary: it is a scientific discipline that studies the coupling between chemical kinetics and fluid dynamics, both of which are challenging by themselves.

On chemical kinetics, due to the large number of intermediate species and elementary reactions during the thermal pyrolysis and oxidation of fuels, the development and validations of chemical models are very challenging. As shown in the Lu-Law diagram [93], the size of the chemical model grows significantly with increasing size of fuel molecules. To date, some large chemical models contain as many as a few thousand species and tens of thousand reactions [93].

On fluid dynamics, complexities lie in turbulence, multi-time and multi-length scale transport, and the nonlinear nature of the Navier-Stokes equations. Especially in turbulent reacting flows, temporally and spatially well resolved measurements are only available for certain quantities, while detailed numerical simulations that can capture the unsteadiness and fine structures in the flow field can be computationally intensive due to the broad range of length/time scales that requires many orders of magnitude in resolution.

However, as already mentioned, in practical combustion systems, where realistic fuel mixtures react in turbulent flows, chemical kinetics and fluid dynamics are strongly coupled, which brings in further complexities. Therefore, simplifications of chemistry or flow are often made to reduce ambiguities in such systems to unravel the coupling effects. For example, the role of chemical kinetics are often studied in homogeneous systems, where transport is negligible. Conversely, in turbulent combustion studies, simple fuels are often used to minimize the uncertainty in chemistry.

The overall objective of this dissertation is to elucidate the chemistry-transport couplings in combustion and emission at practical engine relevant conditions. Specifically, flame dynamics (ignition/extinction/stabilization) and soot emissions are investigated. For both topics, the complexity of the coupling effect is gradually increased by first studying detailed chemical kinetics in one-dimensional laminar flows and then advancing to multi-dimensional (turbulent) configurations.

## 1.1 Chemistry-Transport Coupling in Flame Dynamics

The first half of this dissertation focuses on the coupling effects of chemical kinetics and transport in flame dynamics. An overarching issue here is the potential role of low-temperature chemistry in constituting a flame structure, the interaction of such

a low-temperature flame with flow, and their relevance in practical engine combustion. To approach this question, a general overview on low-temperature chemistry and resulting cool flames is presented first. Evidence showing that low-temperature chemistry can be important for flame dynamics (ignition/extinction/stabilization) are then provided to further motivate this part of work.

### 1.1.1 Low-Temperature Chemistry and Cool Flames

Cool flames, first reported in 1817 [27], are controlled by low-temperature chemical kinetics that have been extensively studied ever since [55]. Such low-temperature chemistry (LTC) is ubiquitous for most hydrocarbon fuels and has been shown to be closely related to the negative temperature coefficient (NTC) phenomenon observed in autoignition processes [18, 62] and engine knock [54]. Practical hydrocarbon-based fuels generally have two-stage ignition processes, in which the first stage ignition is governed by low-temperature chemistry and the second stage ignition by high-temperature chemistry. In both low- and high-temperature regimes, the ignition delay time decreases as the initial temperature increases. However, in the intermediate-temperature regime, the transition of the ignition chemistry results in increased overall ignition delay time as the initial temperature increases. Negative temperature coefficient refers to the phenomenon that the ignition delay time of a fuel/air mixture increases with increasing initial temperature within a certain low-to-intermediate temperature range in relation to its adiabatic flame temperature. This range is typically between 600 and 800 K at 1 atm, which is relatively low compared to a typical flame temperature of 2000 K. Therefore, the terminologies of low-temperature chemistry, NTC chemistry, and cool flame chemistry are often used interchangeably.

The fundamental understanding of low-temperature chemistry and cool flame dynamics can be important for combustion phasing control in the recent development of homogeneous charge compression ignition (HCCI) engines [95] and reactivity con-

trolled compression ignition (RCCI) engines [78]. For example, cool flames and NTC phenomena have been mostly observed in homogeneous systems such as rapid compression machines [141, 102, 30], shock tubes [18, 61, 150], flow reactors[77, 21] and stirred reactors [23, 151, 75]. Without the complexity of inhomogeneity and transport, low-temperature chemical kinetics can be studied in these systems for chemical model development. However, in practical combustors such as diesel and gasoline direct injection (GDI) engines, combustion processes are governed by both transport and chemical kinetics. At such conditions, the characteristic mixing time scales are comparable to the chemical reaction time scales, and the convective-diffusive processes may affect the initiation and development of cool flames. It is reasonable to expect that, in chemically reacting flow, when the characteristic transport time becomes comparable to the NTC chemical time, the two processes will be strongly coupled to affect the local response. By the same reasoning, when the characteristic mixing time becomes relatively long, NTC chemistry will be decoupled from the transport processes, and the system response will recover to that of the homogeneous mixture.

### 1.1.2 LTC in Nonpremixed Flames

Cool flames in nonpremixed systems have been recently studied in counterflow flames [82, 167, 158, 68] and microgravity droplet combustion [111, 39, 112]. Specifically, Law and Zhao [82] and Zhao and Law [167] computationally investigated nonpremixed counterflow cool flames of *n*-heptane and identified the existence of a secondary S-curve dominated by low-temperature chemistry at low strain rates or high pressures, as shown in Fig. 1.1. The steady-state response of a one-dimensional reactive system subjected to heat loss can be studied via the S-curve analysis [81]. In such an analysis, a system response such as the maximum temperature or radical concentration is monitored for variations of an imposed parameter such as the air temperature, for a given strain rate of the flow, or the system Damköhler number.

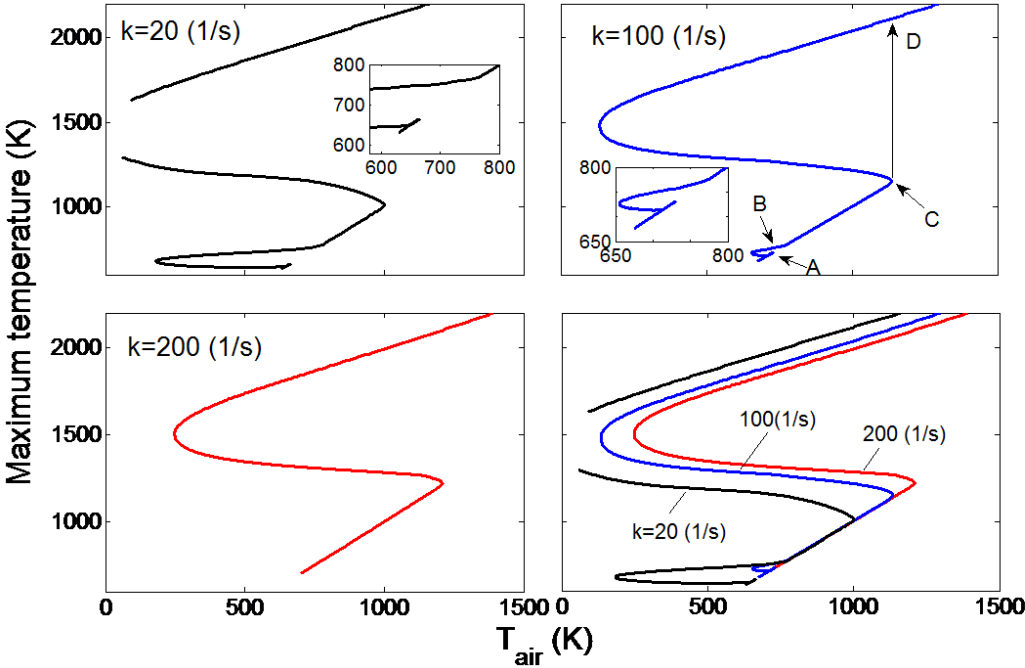


Figure 1.1: Figure 8 in Law and Zhao [82]. The global response S-curve plotted as maximum temperature versus air-side boundary temperature. The strain rate varies from 20 to 100 to 200 /s, and the pressure is 1 atm.

For a global one-step overall reaction with large activation energy, the intrinsically nonlinear Arrhenius kinetics frequently yields multiple solutions characterized by an S-shaped response curve, with the lower and upper turning points respectively designate the ignition and extinction states of the system. Such triple-branch S-curves also frequently emerge for simulations using detailed reaction mechanisms, while more complex response curves with additional turning points have also been obtained, for example for hydrogen oxidation [79, 43] and methane oxidation [90]. However, as shown in Fig. 1.1, the secondary S-curve, computationally obtained by Law and Zhao, has its own ignition and extinction turning points and grafts on the lower branch of the primary S-curve. This secondary S-curve predicts the existence of nonpremixed cool flames at certain conditions.

Moreover, in microgravity droplet combustion, it was found that the visible flame of large *n*-heptane, *n*-octane, and *n*-decane droplets could transit to a quasi-steady

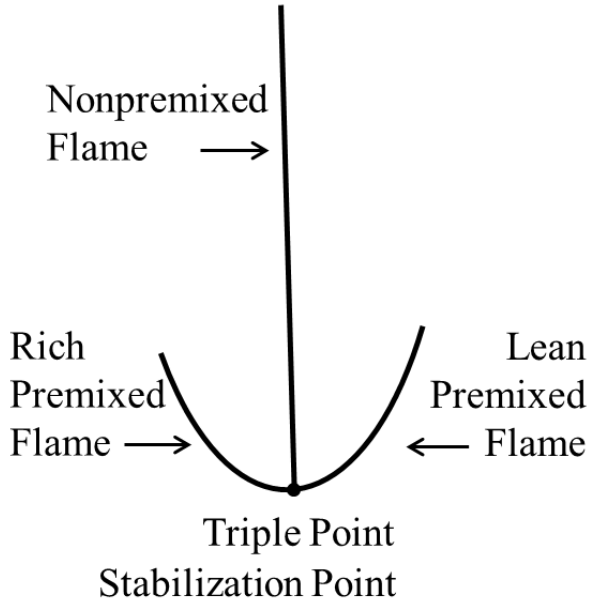


Figure 1.2: A schematic plot of the tribrachial flame structure in a coflow mixing layer.

low-temperature-burning mode after extinction of the hot flame due to radiation, suggesting the existence of steady droplet burning sustained by a cool flame [112].

In Chapter 2 of the dissertation, the computationally predicted nonpremixed counterflow cool flames were experimentally explored. Ignition and extinction states of nonpremixed cool flames were quantified to provide validation data for further development of low-temperature chemical models. Computations with detailed chemistry and transport were then conducted to elucidate the thermal and chemical structure of the nonpremixed cool flames, which lays the foundation for understanding the coupling effects of low-temperature chemistry and transport in more complex flows and flame stabilization.

### 1.1.3 Nonpremixed Flame Stabilization and Oscillation

Nonpremixed jet flames have been extensively studied to understand combustion processes in rocket and diesel engines. The stabilization and structure of jet flames deter-

mine the lift-off height of the flame and are therefore integral to engine design. Due to the mixing process of the fuel and oxidizer streams in lifted flames at nonautoignitive conditions, the combustion mode is partially premixed, leading to the observation of a two-dimensional tribrachial flame (also known as triple flame) [10]; specifically, a lean and a rich premixed flame wings with a trailing diffusion flame branch, as shown in the schematic plot in Fig. 1.2. The point where the three branches intersect is called the triple point and is generally considered to be the stabilization point for nonautoignitive situations. The dynamic balance between the local flame propagation speed and the incoming flow speed is characterized as the stabilization mechanism. A recent review by Chung [17] discussed the stabilization, propagation, and instability of tribrachial flames, including the effects of concentration gradient [32, 59, 51], velocity gradient [76], and burned gas expansion [130, 83, 124, 69]. These studies, however, were limited to nonautoignitive conditions, while real engines operate at elevated pressures and temperatures, where autoignition is activated and could interact with the tribrachial flame.

Chung and co-workers [16, 14, 15] further conducted a series of experiments to investigate the autoignition characteristics of laminar C<sub>1</sub> to C<sub>4</sub> fuel jets in a heated air coflow and found that, above certain coflow temperatures, lifted flames could be established through autoignition. In these studies, both the tribrachial structure for most autoignited cases and a repetitive behavior of extinction and reignition at the critical condition near blowout were observed. It has been found that the ignition delay time plays an important role for the stabilization of autoignited lifted flames, in such a way that the autoignited liftoff height was correlated with the square of the ignition delay time in some of the investigated cases.

Besides the elevated temperature and pressure effects that initiate autoignition, unsteady flow motion can also modify the flame structure in nonpremixed coflows. For example, in the experimental investigation of Strawa and Cantwell [144], flow

instability and flame breakup was achieved by imposing a small-amplitude, periodic velocity fluctuation to nonpremixed jet flames at elevated pressures and low Reynolds numbers. Later, in the computational study of Sánchez-Sanz *et al.* [131], perturbation frequency effects on the thermal and chemical properties of the flame in such periodically time-varying flows were evaluated. Three regimes were found depending on the flame's Strouhal number,  $S = Df/2U$ , with  $D$  and  $f$  denoting the fuel jet diameter and perturbation frequency, respectively. For small Strouhal numbers ( $S = 0.1$ ), perturbations can travel far downstream, resulting in an oscillating flame. Flame surface flickering was observed when  $S \approx 0.2$ , and vigorous flame pinch-off was observed at  $S = 0.5$ . Larger values of  $S$  confine the oscillation to the jet's near-exit region with the pulsation having minimal effects on temperature and concentration values. The unsteadiness in flickering flames also increases pollutant formation, such as soot [138] and carbon monoxide [142]. Mohammed *et al.* [103] followed by Dworkin *et al.* [37] conducted computational and experimental studies of 20 Hz periodically-forced methane/air coflow diffusion flames. Acetylene production increased [103] and the oxidation of CO to CO<sub>2</sub> was inhibited [37] in the downstream region of the flame at certain times during the flame's cyclic history.

#### 1.1.4 LTC in Flame Stabilization

As reviewed in previous sections, low-temperature chemistry can induce two-stage ignition and is promoted at elevated pressures. Consequently, NTC-affected stabilization of nonpremixed lifted jet flames can be potentially important, yet few studies have performed any detailed analysis. Krisman *et al.* [80] recently conducted a numerical study of dimethyl ether (DME)/air mixing layer at 40 atmospheres and air coflow temperatures ranging from 700 to 1500 K and observed multibrachial structures in the heat release rate profiles. The mixture fractions (local composition states) corresponding to the stabilization points defined based on the hydroxyl radical (OH) mass

fraction, and the first stage autoignition kernels based on the methoxymethylperoxy radical ( $\text{CH}_3\text{OCH}_2\text{O}_2$ ), were compared with the most reactive mixture fractions computed from homogeneous autoignition under the same initial conditions. A transport budget analysis based on selected species was performed to differentiate deflagration from autoignition.

In light of the reported multibrachial structure, showing a modified flame shape from autoignition in the mixing layer, further investigation is warranted to identify the detailed chemical structure and stabilization mechanism of the multibrachial flame. For example, tools for computational diagnostics, especially for identifying locally dominant chemical reactions, can be employed to understand the controlling chemistry. Moreover, a direct comparison to homogeneous autoignition is insufficient to understand the transport processes in the current configuration. In the two-dimensional mixing layer, transport processes in two directions are important: parallel and normal to the mixture fraction gradient, which are due to the transverse stratification of temperature and species and streamwise flow and (flame back) diffusion, respectively. These considerations would significantly improve the understanding of the role of autoignition upstream of the flame structure and quantitatively identify the controlling kinetics and stabilization mechanism.

In Chapter 3 of this dissertation, nonpremixed coflow flame dynamics under autoignitive conditions were computationally investigated. Leveraging the understanding of low-temperature chemistry obtained from nonpremixed counterflow cool flame studies in Chapter 2, the role of NTC chemistry in flame stabilization at engine relevant conditions will be elucidated. Moreover, the dominant stabilization mechanism at various flow conditions and the effect of unsteadiness on flame dynamics will be investigated to demonstrate the coupling of fluid dynamics and chemical kinetics to further facilitate future turbulent studies.

## 1.2 Chemistry-Transport Coupling in Soot Emissions

The second half of this dissertation focuses on the coupling effects of chemical kinetics and transport in sooting flames. A general question that governs the subsequent investigations is how soot evolution happens in practical engine combustion. To approach this question, a general overview on soot formation and emission is presented first. Fuel and flow effects on soot evolution are then reviewed to further motivate this part of work.

### 1.2.1 Soot Mechanisms and Emissions

In addition to flame dynamics, emissions from combustion processes are also subject to the coupling effects of chemical kinetics and flow dynamics. One of the dominant pollutants that appears in the form of particulate matter (PM) is carbon black or soot. Soot particles are undesired products of rich combustion in a wide variety of engineering and natural systems, including transportation and propulsion engines, power generation devices, and fires. Significant exposure to these black nanoparticles is known to cause heart diseases or lung cancer [33]. In addition, particles emitted from aircraft engines enhance nucleation in the formation of contrails and other atmospheric aerosols [66, 135]. Because of the adverse effects on human health and the environment, stringent regulations on emissions from automotive and aircraft engines have been proposed by governments worldwide.

The evolution of soot particles is governed by both physical and chemical processes, and the exact mechanisms of soot evolution remain open questions in varying degrees. A general soot model includes inception, growth, collision, and destruction of soot particles, as shown in the schematic drawing in Fig. 1.3. During the inception process, gaseous soot precursors nucleate to form the first soot particle [133, 159, 9].

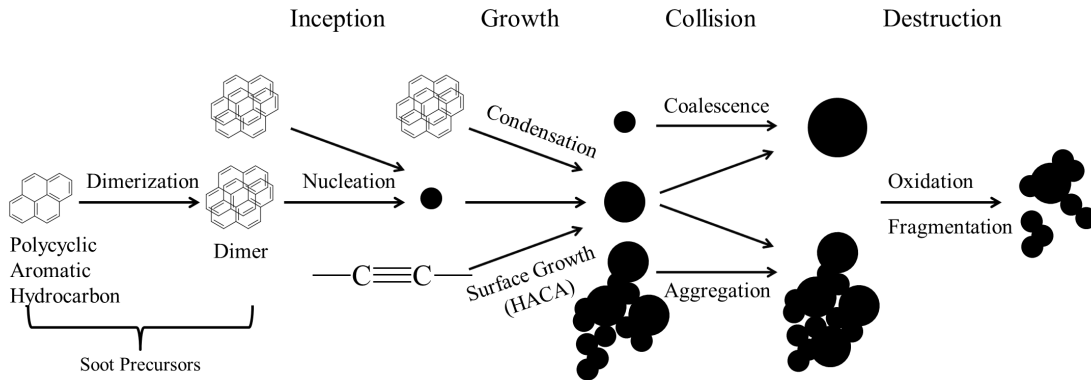


Figure 1.3: A schematic drawing of the physical and chemical processes that govern soot evolution.

Most soot models consider that these precursors originate in benzene and grow by addition of carbon atoms following the H-abstraction  $\text{C}_2\text{H}_2$ -addition (HACA) mechanism [45]. Large hydrocarbon molecules are formed from the continuing growth of carbon atoms and appear in ring structures, generally referred as polycyclic aromatic hydrocarbons (PAH) [133]. The subsequent soot growth processes are also closely related to PAH and acetylene, through physical condensation [117, 100, 101] and chemical surface growth with the HACA mechanism [45], respectively. The collision between soot particles also modifies soot morphology. Two extreme cases are demonstrated in Fig. 1.3: two small soot particles completely merge to a big spherical particle, or they just barely stick to each other, preserving the total surface area. Experimentally, soot particles have been found to be both spheres [165] and fractal aggregates [67], as shown in Fig. 1.4. Finally, if the soot particles are exposed to oxidizers such as oxygen and hydroxyl radical, soot fragmentation and oxidation may occur [71, 113], resulting in the destruction of soot particles.

Understanding of soot mechanism has been acquired through experiment and modeling. While experiments provide data to guide model development and validation, modeling provides insights to help design experiments, improve experimental techniques and understand some of the mechanisms inaccessible in experiments. How-



Figure 1.4: Transmission electron microscopy (TEM) images of soot aggregate from Jensen *et al.* [67].

ever, large uncertainties are still associated with soot models in both the gas phase PAH chemistry and soot dynamics. Due to limited optical access in sooting flames for online species measurement, validation data for PAH chemical model development is limited. Therefore, how these large PAH species are formed from smaller species during the fuel breakdown processes needs to be investigated in well-controlled laminar experiments to obtain fundamental understanding of PAH chemical kinetics. This will then allow the development of relatively high-fidelity soot models to be utilized in, for example, turbulent sooting flame computations to investigate soot evolution in practical engines, for detailed characterization of the flow field and soot would not be available due to experimental limitations.

### 1.2.2 Role of Fuel Structure in PAH Chemistry and Soot Emissions

The utilization of biofuels, which are potential partial replacements for liquid fuels derived from fossil fuels, is garnering wide attention not only because these fuels are

renewable, locally producible, and carbon neutral [88] but they also hold potential for positive impacts on particulate matter emission control. Biofuels, including bioalcohols and biodiesels, mainly consist of oxygenated hydrocarbons, such as ethers, alcohols, and esters. When used as additives in conventional diesel fuels, PM emissions have been found to decrease as oxygenated additive concentrations increase [53].

However, the precise role of oxygenated additives on the reduction of soot emission has not yet come to a scientific consensus. For example, Frijters and Baert [47] attributed the PM reduction to the fuel oxygen content, which reduced the local equivalence ratio and, by implication, the flame temperature. However, even with the same oxygen content, the oxygenates have different efficiencies in the reduction of soot precursor, as Westbrook *et al.* [157] found through simulations of premixed *n*-heptane and oxygenates flames. Furthermore, Pepiot *et al.* [118] proposed a structural group contribution approach to interpret diesel engine experimental data and quantify the soot reduction tendency of oxygenated fuels. As noted by the authors, the aromatics contained in the conventional diesel fuels have very strong sooting tendencies, which are moderated through substitution by the clean-burning oxygenated additives; this replacement effect should be identified and quantified to reveal the role of the oxygen moieties.

Conversely, a number of studies show that oxygenated fuels do not necessarily have lower sooting tendencies than regular hydrocarbons. McEnally and Pfefferle [97, 98] found that methane coflow nonpremixed flames doped with butanol isomer produce more soot than the undoped ones. As only 1000 ppm of each test compound was added to the methane stream, the study was able to identify the direct chemical effects of the additives. It was subsequently found that the effect of carbon chain length on soot formation is often larger than the direct chemical effects of oxygen and branches in the carbon chain in promoting soot formation. Similar conclusions were reached by Camacho *et al.* [13] by probing the evolution of the detailed particle size

distribution function in a set of laminar premixed flames of *n*- and *i*-butane/butanol with fixed C/O ratio and maximum temperature.

To further explore the sooting characteristics of oxygenated fuels and understand the chemical pathways for soot formation processes, additional well-controlled fundamental experiments and detailed chemical kinetic analyses need to be performed. In particular, it is recognized that, besides the thermal and replacement effects of oxygenated additives, the residence times of soot precursors are also expected to influence the sooting propensities [148, 154] since soot formation is a kinetically controlled process [149].

In Chapter 4 of the dissertation, to investigate the important pathways of soot formation, experimental and computational study first focused on the sooting limits (a residence time effect) of three neat liquid diesel/biofuel components in a stagnation-flow liquid pool system. With the knowledge on the chemical kinetics of laminar sooting flames, the chemistry-transport coupling effect on soot evolution in turbulent flows was further investigated in Chapter 5.

### 1.2.3 Combined Role of Fuel and Turbulence in Soot Emissions

Soot formation, growth, and oxidation have been extensively studied in laminar configurations, since flow conditions are better controlled and characterized, which enables detailed analysis of soot evolution [153]. However, most practical devices operate under turbulent conditions. The understanding of soot evolution in turbulent reacting flows and the small-scale interactions among soot, turbulence, and chemistry has been aided by Direct Numerical Simulation (DNS). In the past, these studies have been limited to two-dimensional configurations and/or empirical soot models to limit the computational cost [161, 86, 85, 6], but, recently, Attili *et al.* [1] performed the first three-dimensional DNS of turbulent nonpremixed jet flames employing a high-order

statistical model of soot and a detailed chemical mechanism, which includes the soot precursor naphthalene, and investigated Damköhler number effects on soot formation and growth [2]. Nevertheless, similar to all combustion DNS studies, the Reynolds number was limited to 15,000, which is lower than most practical combustion systems.

To investigate jet flames at high Reynolds numbers, a combination of experiments [128, 127, 84, 164] and Large Eddy Simulation (LES) [38, 109, 160] has been used. However, the jet flame configuration does not contain the more complex fluid dynamics found in practical combustion systems such as recirculating flow. To bridge this gap, recent experiments and LES have been used to understand the role of recirculating flow on soot evolution in simple, canonical geometries. Mueller *et al.* [107] experimentally and computationally investigated a turbulent nonpremixed bluff body ethylene flame. Unlike jet flames, surface growth with HACA mechanism was found to dominate in the recirculation zone, highlighting the significance of hydrodynamics on soot evolution.

It is further noted that during the thermal decomposition of hydrocarbon fuels, addition of hydrogen slows down soot formation [147]. Extensive laminar studies have been conducted with simplified flow conditions to understand the overall suppression of soot formation in hydrogen-enriched diffusion flames and have attributed such suppression to both dilution and chemistry effects, through the change of the flame temperature and the shift of the balance of the C<sub>2</sub>H<sub>2</sub>-addition reactions [28, 36, 57, 58, 166]. It would be interesting to investigate whether such chemical effects will couple with turbulence in turbulent sooting flames.

In Chapter 5 of the dissertation, a combination of experiments and computations will be utilized to investigate chemical and hydrodynamic effects of fuel composition on the soot evolution in nonpremixed turbulent bluff body flames. The comparisons between experiments and computations will further validate the LES model and eluci-

date the important role of chemistry-transport coupling in soot evolution in turbulent flow with complex geometry.

## 1.3 Organization of the Dissertation

This dissertation is aimed to advance the understanding on the coupling effects of chemistry and transport on flame dynamics and emissions for practical applications. The first part of the dissertation focuses on flame dynamics at engine relevant conditions. Specifically, in Chapter 2, cool flames and low-temperature chemistry in nonpremixed counterflows are investigated both experimentally and computationally. Leveraging the understanding of low-temperature chemical kinetics in relatively simple flows, in Chapter 3, flame dynamics in laminar nonpremixed coflow flames under elevated temperatures and pressures are investigated, and the role of low-temperature chemistry in flame stabilization and oscillation is explored. The second part of the dissertation focuses on soot emissions with engine relevant fuels in complex flows. Similar to the structure in flame dynamics studies, in Chapter 4, experimental and computational investigations of sooting limits of liquid diesel, bioalcohol, and biodiesel fuels in stagnation-flows are presented. The same soot model is used to investigate soot evolution in nonpremixed turbulent bluff body flames and compared with experiments, in Chapter 5. Finally, in Chapter 6, the conclusions of this dissertation are drawn, and suggestions are made for the direction of future work.

During the preparation of this dissertation, the following work has been compiled for peer-reviewed journal publication.

- **Chapter 2:**

1. S. Deng, P. Zhao, D. Zhu, C.K. Law, NTC-affected ignition and low-temperature flames in nonpremixed DME/air counterflow, *Combustion and Flame* **161** (2014) 1993-1997.

2. S. Deng, D. Han, C.K. Law, Ignition and extinction of strained non-premixed cool flames at elevated pressures, *Combustion and Flame* (2016) under review.

- **Chapter 3:**

3. S. Deng, P. Zhao, M.E. Mueller, C.K. Law, Autoignition-affected stabilization of laminar nonpremixed DME/air coflow flames, *Combustion and Flame* **162** (2016) 4471-4478.
4. S. Deng, P. Zhao, M.E. Mueller, C.K. Law, Stabilization of laminar non-premixed DME/air coflow flames at elevated temperatures and pressures, *Combustion and Flame* **162** (2016) 4471-4478.
5. S. Deng, P. Zhao, M.E. Mueller, C.K. Law, Flame dynamics in oscillating flows under autoignitive conditions, *Combustion and Flame* **168** (2016) 75-82.

- **Chapter 4:**

6. S. Deng, J.A. Koch, M.E. Mueller, C.K. Law, Sooting limits of non-premixed *n*-heptane, *n*-butanol, and methyl butanoate flames: Experimental determination and mechanistic analysis, *Fuel* **136** (2014) 122-129.

- **Chapter 5:**

7. S. Deng, M.E. Mueller, Q.N. Chan, N.H. Qamar, B.B. Dally, Z.T. Alwahabi, G.J. Nathan, Hydrodynamic and chemical effects of hydrogen addition on soot evolution in turbulent nonpremixed bluff body ethylene flames, *Proceedings of the Combustion Institute* **36** (2017) under review.

- **Not included in this dissertation:**

8. P. Zhao, W. Liang, S. Deng, C.K. Law, Initiation and propagation of laminar premixed cool flames, *Fuel* **166** (2015) 477-487.
9. D. Han, S. Deng, W. Liang, P. Zhao, F. Wu, Z. Huang, C.K. Law, Laminar flame propagation and nonpremixed stagnation ignition of toluene and xylenes, *Proceedings of the Combustion Institute* **36** (2017), in press.

# Chapter 2

## Nonpremixed Counterflow Cool Flames

As reviewed in Chapter 1.1.1, the invariable existence of nonuniformities in practical combustion systems requires consideration of the coupled effects of chemistry and transport on cool flames. Consequently, in this chapter, nonpremixed counterflow cool flames studies are presented. The primary objective is to experimentally explore the existence of nonpremixed cool flame. The investigation is a challenging one because of the weak reactivity and the correspondingly weak exothermicity involved. Upon the affirmation of the exploration of the nonpremixed cool flame, characterization of the ignition and extinction behavior of the cool flame is performed and compared with computations to facilitate further studies on cool flames.

### 2.1 Experimental Investigation

Dimethyl ether (DME) was selected as the fuel for the present study because it is gaseous and is one of the simplest hydrocarbons exhibiting NTC behavior. Furthermore, detailed reaction mechanisms for low- and high-temperature DME oxidation [22, 41, 21, 169] have been developed and validated for burner stabilized

flames [70], nonpremixed counterflow flame ignition [171], laminar flame speeds [129], and studies using rapid compression machines [102]. This allows the computational simulation and thereby guidance and verification of the experimentation with moderate confidence. In particular, computations presented in Sec. 2.2 were conducted using a skeletal mechanism of 39 species [5] reduced from the detailed mechanism of Zhao *et al.* [169].

A schematic of the experimental setup is shown in Fig. 2.1; detailed descriptions of the counterflow experimental apparatus are given in [42, 87]. Briefly, the apparatus consists of two vertically oriented opposing quartz nozzles with diameters of 20 mm separated by 20 mm. A heated air or N<sub>2</sub> stream is issued from the upper nozzle and impinges against a room-temperature N<sub>2</sub>-diluted DME steam issued from the lower nozzle. Both upper and lower streams are shielded by coflowing N<sub>2</sub> to minimize disturbance from the environment. In a typical counterflow ignition experiment, ignition is achieved by gradually increasing the air boundary temperature until a visible flame appears. The exit temperature, measured by a thermocouple with radiation correction [170], is then defined as the ignition temperature. Single-point laser Doppler velocimetry (LDV) is used to measure the axial flow velocity along the centerline to determine the local strain rate (velocity gradient) of the flow.

While the above procedure has been successfully used in previous studies of ignition and the diagnosis of the resulting flame for strongly burning flames, for which the instant of ignition can be observed visually, no bright flame or visually-detectable reaction front could be observed for the present NTC-affected ignition within the temperature range of interests (600-800 K). Furthermore, no discernable heat release was detected by using a thermocouple, ostensibly due to the small amount of heat release from the low-temperature chemistry. In the absence of a visible flame, it was also not clear the extent of the disturbance introduced by the thermocouple to the flow field as well as the ignition kernel.

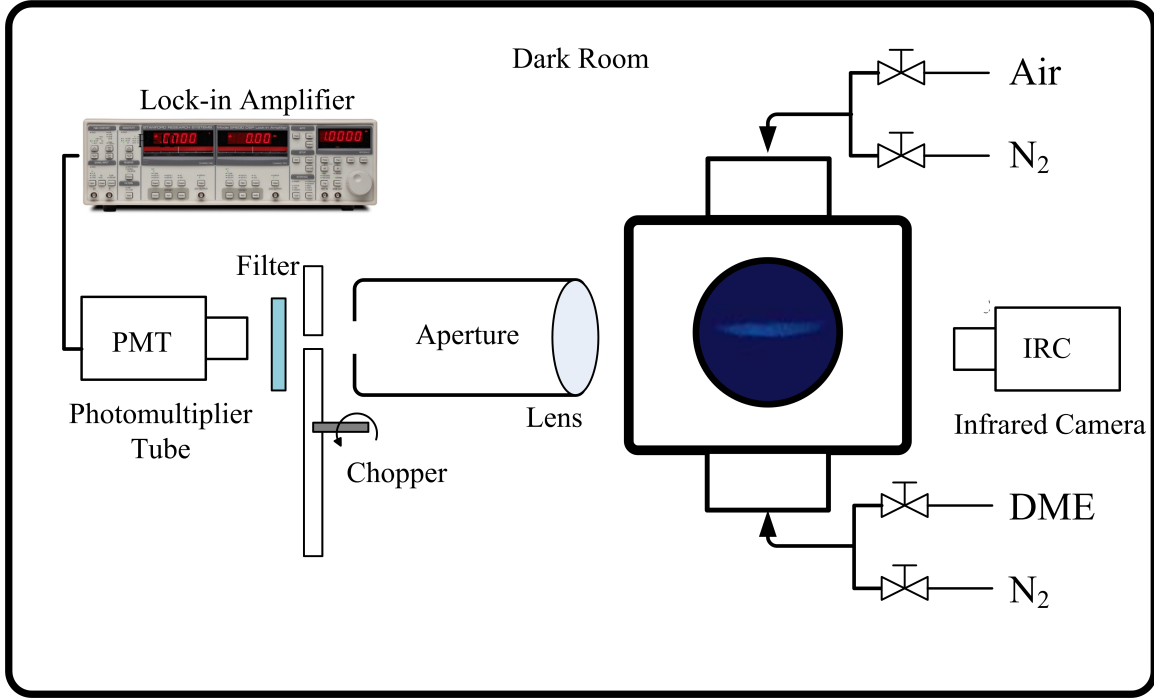


Figure 2.1: Schematic of the nonpremixed DME/air counterflow system for the detection of cool flames and quantification of the cool flame ignition temperatures.

In view of the above limitations, optical detections and measurements were chosen for this work. A photomultiplier tube (PMT) was subsequently applied to detect any NTC-related chemiluminescence, noting that experimental studies in homogeneous systems have shown that the NTC-induced chemistry have characteristic chemiluminescence spectra, with a small amount of heat release [140, 116]. These studies further showed that a large amount of formaldehyde ( $\text{CH}_2\text{O}$  or  $\text{HCHO}$ ) is formed from the low-temperature chemistry and the pale blue chemiluminescence from  $\text{CH}_2\text{O}$  characterizes the associated low-temperature reaction [49]. Based on these characteristics, the experimental setup was designed as shown in Fig. 2.1. Here a Hamamatsu 931B PMT combined with focusing lens system and a Newport filter (10BPF10-400) was used to detect the chemiluminescence corresponding to the characteristic wavelength of formaldehyde (peaks around 400 nm) and to reduce noise light signals from the counterflow chamber. The PMT signal was then collected and processed with a SR510 lock-in amplifier to further diminish the noise. Results based on this experimentation

to demonstrate the existence of the low-temperature chemistry in the counterflow are discussed in Sec. 2.3.1. This is followed by an investigation based on infrared imaging to identify the state of ignition, in Sec. 2.3.2.

## 2.2 Computational Investigation

As introduced in Sec. 1.1.2, the steady-state response of a one-dimensional reactive system subjected to heat loss can be studied with the S-curve analysis [81]. In such an analysis, a system response such as the maximum temperature or radical concentration is monitored for variations of an imposed parameter such as the air temperature, for a given strain rate of the flow, or the system Damköhler number. A typical S-shaped response curve has a lower turning point that designates the ignition state and a upper turning point that corresponds to the extinction state.

Figure 2.2 shows the schematics of the axisymmetric nonpremixed counterflow configuration. The origin of the cylindrical coordinate  $(r, y)$  is at the center of the lower boundary surface. Furthermore, the axial and radial velocity components are designated as  $v$  and  $u$ , respectively.

The governing equations for the counterflow nonpremixed flame are presented by Smooke and co-workers [52, 143]. In brief, the flow is assumed to be laminar, stagnation-point flow in cylindrical coordinates. In practice, the infinite interval for potential flow is truncated and the boundary conditions are applied at  $y = 0$  and  $y = 2L$  for the fuel and oxidizer streams, respectively, where  $L$  denotes the separation distance between the two nozzles. The governing equations for mass, momentum, chemical species, and energy with boundary layer assumptions are considered, and the system is closed with the ideal gas law. The free stream radial and axial velocities at the edge of the boundary layer (the fuel side boundary) are given by  $u_e = ar$  and  $v_e = -2ay$ , where  $a$  is the single strain rate throughout the flow. Upon introducing

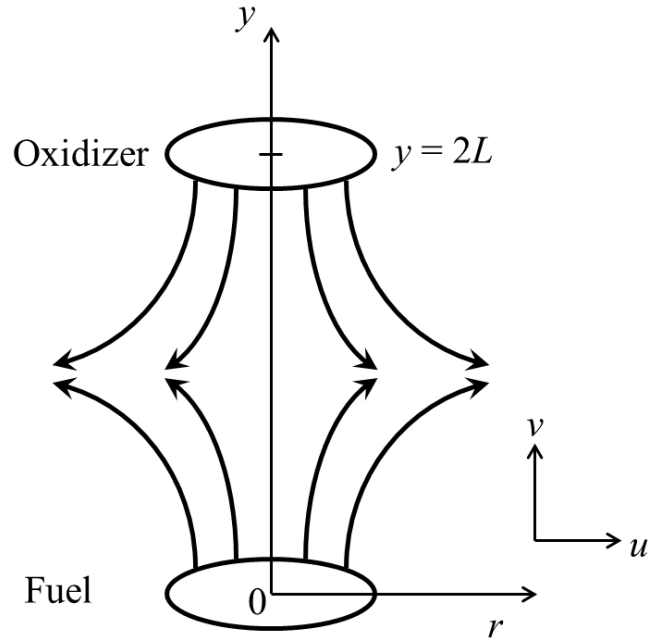


Figure 2.2: Schematic of the nonpremixed counterflow configuration for S-curve analysis.

the notation

$$f' = \frac{u}{u_e}, \quad (2.1)$$

$$V = \rho v, \quad (2.2)$$

where  $f'$  is related to the derivative of a modified stream function [31],  $V$  is the axial mass flux, and  $\rho$  is the gas density, the boundary layer equations can be transformed into a system of ordinary differential equations valid along the stagnation-point streamline  $r = 0$ , summarized below.

$$\frac{dV}{dy} + 2a\rho f' = 0, \quad (2.3)$$

$$\frac{d}{dy} \left( \mu \frac{df'}{dy} \right) - V \frac{df'}{dy} + a(\rho_e - \rho(f')^2) = 0, \quad (2.4)$$

$$\frac{d}{dy} (\rho Y_k V_k) + V \frac{dY_k}{dy} - \dot{\omega}_k W_k = 0, k = 1, 2, \dots, K, \quad (2.5)$$

$$\frac{d}{dy} \left( \lambda \frac{dT}{dy} \right) - c_p V \frac{dT}{dy} - \sum_{k=1}^K \rho Y_k V_k c_{pk} \frac{dT}{dy} - \sum_{k=1}^K \omega_k W_k h_k = 0. \quad (2.6)$$

In these equations,  $\mu$ ,  $\lambda$ , and  $c_p$  are the dynamic viscosity, heat conductivity, and the constant pressure heat capacity of the mixture, respectively. For the  $K$  species in total considered in the chemical mechanism,  $Y_k$ ,  $V_k$ ,  $\omega_k$ ,  $W_k$ ,  $c_{pk}$ , and  $h_k$  denote the mass fraction, diffusion velocity, molar production rate, molecular weight, constant pressure heat capacity, and specific enthalpy of each species, respectively.

The numerical code adopted to solve them employs the damped Newton method and time integration solution scheme [143]. The S-curve marching is performed using the flame-controlling method of Nishioka *et al.* [115] with detailed chemistry [73] and transport database [72].

## 2.3 Nonpremixed Cool Flames at Atmospheric Conditions

### 2.3.1 Identification of the Cool Flame

Validation results for the experimental system are shown in Fig. 2.3. Specifically, when the PMT captures the photons corresponding to the characteristic wavelength of CH<sub>2</sub>O (peaks around 400 nm), it outputs negative impulses to the oscilloscope, with the amplitudes of these impulses representing the light intensity. Figure 2.3 shows that such signal intensity drops after replacing either N<sub>2</sub>-diluted DME with pure N<sub>2</sub> issued from the lower nozzle (at point a) or air with N<sub>2</sub> issued from the upper nozzle (at point c), demonstrating that the signal is due to the simultaneous presence of air and DME. Since replacing air with the same flow rate of N<sub>2</sub> barely affects the temperature profile and the flow field, the signal difference between the air/DME and N<sub>2</sub>/DME cases indicates the existence of NTC chemical activities. It is noted that

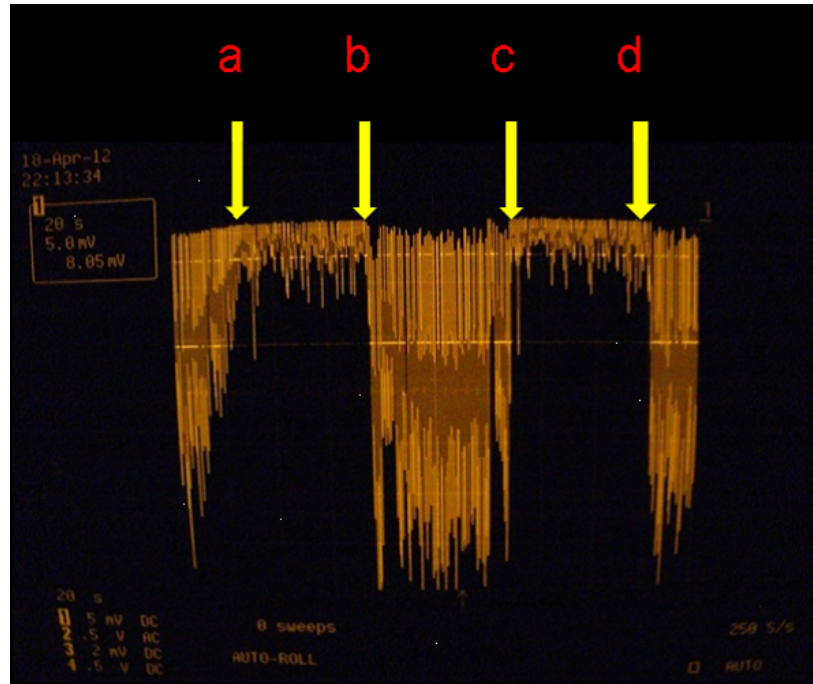


Figure 2.3: “M” shaped signal observed with the PMT-osilloscope system from the counterflow chamber at atmospheric pressure. The fuel stream consists of 30% DME and 70% nitrogen, and the oxidizer is air. a. Switch Air/DME to Air/N<sub>2</sub>; b. Switch Air/N<sub>2</sub> to Air/DME; c. Switch Air/DME to N<sub>2</sub>/DME; d. Switch N<sub>2</sub>/DME to Air/DME.

the signal from N<sub>2</sub>/DME thermal pyrolysis is minimal, such that the difference in the chemically reactive and non-reactive cases can be completely attributed to the low-temperature oxidation chemistry.

In Fig. 2.4, the chemiluminescence intensity from the CH<sub>2</sub>O under the strain rates of 40, 60, and 100 /s were measured as a function of the air boundary temperature. The time-averaged signal was acquired by the lock-in amplifier with an integration time of three seconds to minimize the noise, and the error bars show the standard deviation of the signals based on 1000 samples. The results clearly show that the low-temperature chemistry becomes more pronounced at higher air temperatures and lower strain rates, with more CH<sub>2</sub>O produced and therefore stronger chemiluminescence from it.

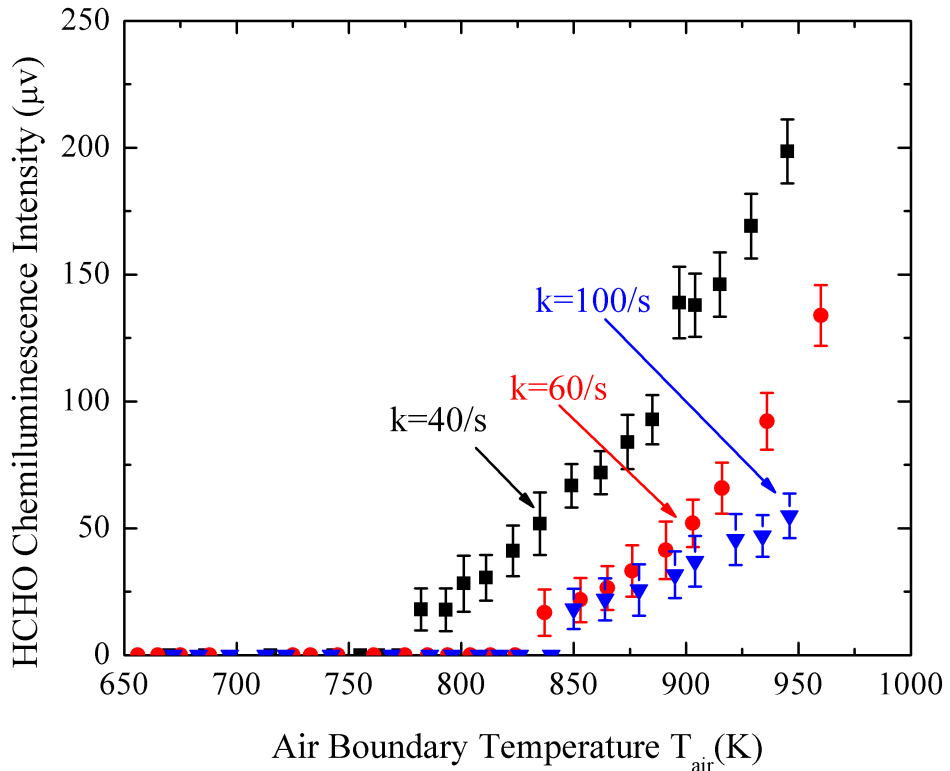


Figure 2.4: Formaldehyde chemiluminescence intensity at different air boundary temperatures under various strain rates.

The above experimental observations are further corroborated by the calculated results of the maximum formaldehyde mole fraction versus the air temperature for 30% DME in nitrogen, for different strain rates. Figure 2.5 shows the calculated secondary S-curve characterized by the low-temperature chemistry. It is seen that the upper branch solution, designating the state of the low-temperature flame, shows the same experimental trend of increasing  $\text{CH}_2\text{O}$  concentration with increasing air temperature and decreasing strain rate. The strongly transport-affected, nonpremixed counterflow have therefore been identified. The fact that this chemical reactivity is localized in a thin flame region is demonstrated in the next section.

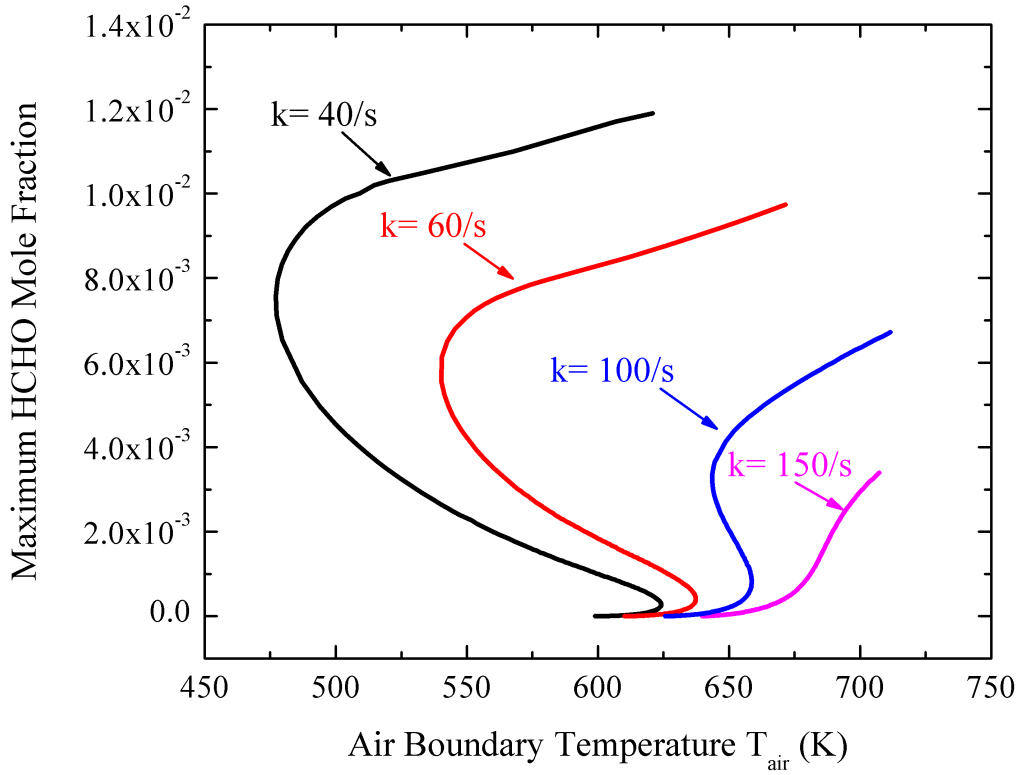


Figure 2.5: Maximum formaldehyde mole fraction of 30% DME at different air boundary temperatures under various strain rates.

### 2.3.2 Determination of Ignition Temperature

Detections of the state of ignition of the NTC-flame are therefore proceeded, as identified by the lower turning points in Fig. 2.5. Since the chemiluminescence intensity from the above experimentation is not strong enough to detect the low level of CH<sub>2</sub>O concentration at ignition, detections of ignitions have been resorted to capturing the infrared radiation from the ignition process by using a highly sensitive infrared camera, FLIR SC640 (with the thermal sensitivity about 60 mK at 303 K), as shown on the right part of Fig. 2.1. The brightness of the IR images in Fig. 2.6 indicates the IR radiation intensity, with the bright color denoting higher radiation intensity than the dark color. Since both the air/DME and N<sub>2</sub>/DME flows now radiate infrared signals

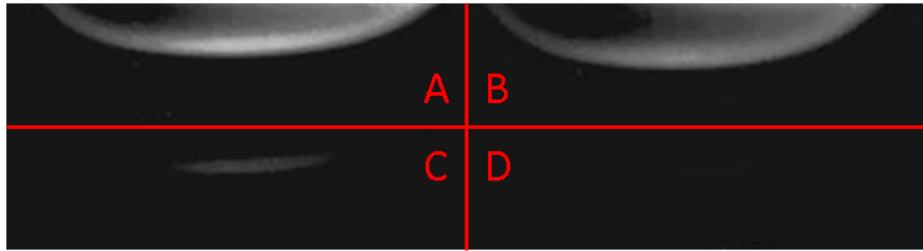


Figure 2.6: A/B: Heated air/ $\text{N}_2$  against DME counterflow IR images at ignition (atmospheric pressure, strain rate 60 /s); C/D: Difference between A/B and B.

when heated due to the excitation of the vibrational modes of the gas molecules in the thermal mixing layer, the background  $\text{N}_2/\text{DME}$  signal needs to be subtracted out from the air/DME signal to isolate/identify the emission due to the low-temperature chemical reactivity. Consequently, by gradually increasing the air boundary temperature, and by setting the IR radiation intensity of the  $\text{N}_2/\text{DME}$  flow as the reference state, the first appearance of an excess signal from the air/DME flow would indicate the onset of ignition. In practice, when the air boundary temperature reaches the regime of interest, only 1 K is increased each time at the air boundary before the flow becomes steady again. It is fairly clear that at a certain temperature, which is defined as the ignition point, the signal from air/DME starts to exceed that of the reference state. Such temperature measurements are repeatable within  $\pm 2$  K. A typical result is shown in Fig. 2.6, in which the A and B panels are the raw IR signals for heated air and  $\text{N}_2$  against DME, which are respectively reactive and nonreactive. Panels C and D respectively show the residue signals of panels A and B after the background signal from panel B is subtracted; the null signal for D is obtained by default. The temperature at which a discernable image of radiation is detected is then identified as that of ignition, as is the case for panels A/C, for the corresponding strain rate.

The localized nature of the IR radiation, shown in panel C, then also supports the notion that the chemical reactivity observed herein has the characteristic of a

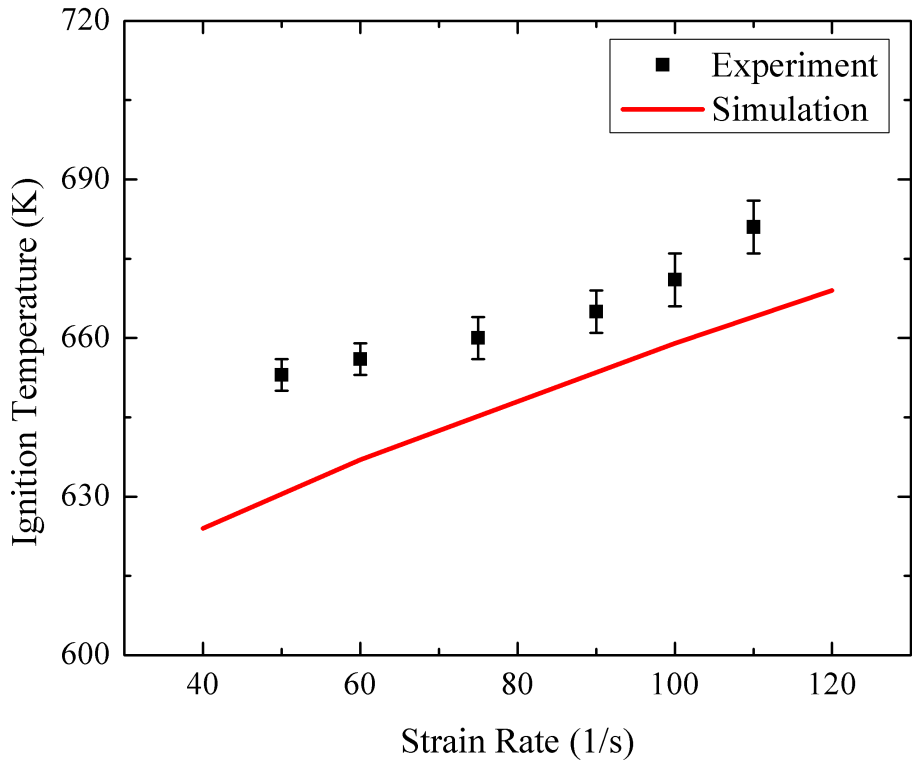


Figure 2.7: Calculated and observed ignition temperatures of 30% DME under various strain rates at atmospheric pressure.

flame, in support of the interpretation of the chemiluminescence signal reported in the previous section.

Figure 2.7 shows the IR measurements of the low-temperature chemistry induced ignition, as determined through the above procedure, as a function of the strain rate. The uncertainty bars account for those from the thermocouple radiation correction as well as reproducibility of the experimental measurements. Due to the moderate flow field temperatures and the high sensitivity of the thermocouple, the uncertainty bars of the ignition temperatures are quite small. These experimental values are then compared with those corresponding to the calculated lower, ignition turning points. Figure 2.7 shows satisfactory agreement, with the average temperature difference being within 20 K.

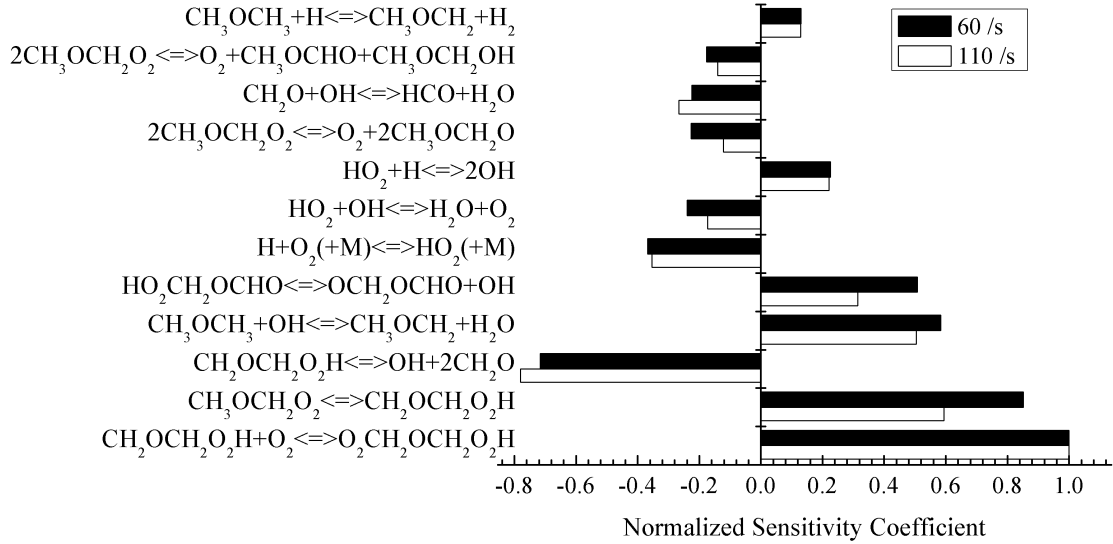


Figure 2.8: Sensitivity analysis on low and high strain rate cases at atmospheric pressure: DME mole fraction is 30%.

Sensitivity analysis was further performed for the state of ignition, as shown in Fig. 2.8. It is seen that the controlling chemistry is indeed the low temperature chemistry, corresponding to the first stage ignition of the homogeneous autoignition process in the NTC-affect regime. More specifically, the first two most important reactions that promote the low-temperature chemistry induced ignition are the oxygen combination reaction  $\text{CH}_2\text{OCH}_2\text{O}_2\text{H} + \text{O}_2 \rightleftharpoons \text{O}_2\text{CH}_2\text{OCH}_2\text{O}_2\text{H}$  and the isomerization reaction  $\text{CH}_3\text{OCH}_2\text{O}_2 \rightleftharpoons \text{CH}_2\text{OCH}_2\text{O}_2\text{H}$ , while the most important retarding reaction is the  $\beta$ -scission reaction  $\text{CH}_2\text{OCH}_2\text{O}_2\text{H} \rightleftharpoons \text{OH} + 2\text{CH}_2\text{O}$ . These two groups of reactions compete for the  $\text{CH}_2\text{OCH}_2\text{O}_2\text{H}$  radicals and as such function oppositely.

In addition to the effects of strain rate on the ignition temperature, the effects of DME concentration have also been evaluated, shown, and compared with the simulation results in Fig. 2.9. The simulation result basically demonstrates the insensitive nature of the NTC-affected ignition temperature to the variation of the boundary DME concentrations over an extensive range of DME concentrations, under a fixed strain rate of 60 /s. The experimental results again show good agreement with the

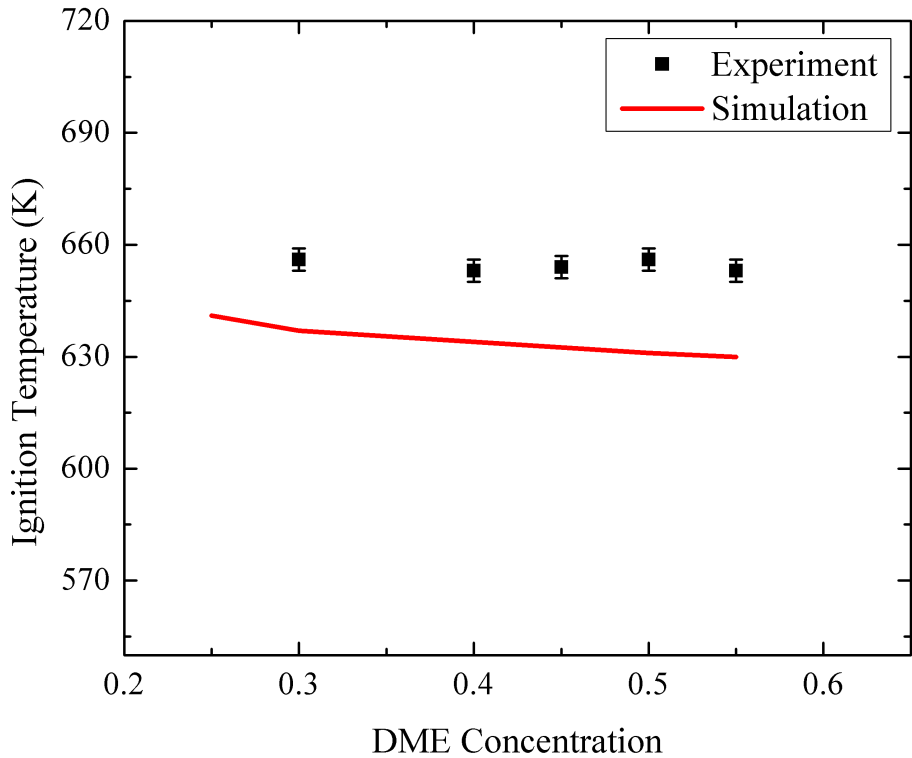


Figure 2.9: Ignition temperatures of various DME concentrations under the strain rate of  $60 \text{ /s}$  at atmospheric pressure.

simulation results. This effect corresponds to the insensitive nature of the equivalence ratio in the low-temperature chemistry, given the fact that the first-stage delay is insensitive to the equivalence ratio in the homogeneous autoignition process [167]. Sensitivity analysis corresponding to different boundary DME concentrations were also carried out, showing the same controlling chemistry as that of Fig. 2.8.

## 2.4 Nonpremixed Cool Flames at Elevated Pressure

Recognizing that low-temperature chemistry is more pronounced at elevated pressure, which for example could affect flame stabilization, as will be shown in Chapter 3, a systematic experimental and computational study on nonpremixed DME cool flames at elevated pressures is presented here. Although the experimental approach presented in Sec. 2.3.1 is able to capture the ignition temperature of nonpremixed cool flame, it has two major limitations. First, the infrared signal is not able to penetrate the quartz window of the counterflow chamber for elevated pressure experiments. Second, due to the experimental procedure of switching between the oxidizer and inert for ignition detection, the extinction temperature of the nonpremixed cool flame cannot be measured. Therefore, the experimental system and the detection method for cool flame ignition and extinction need to be improved.

### 2.4.1 Improvement of the Experimental Methodology

The counterflow system is kept the same as described in Sec. 2.1. To accommodate experiments at elevated pressures, the exhaust valve of the chamber is adjusted to balance the inflow and outflow and maintain the desired chamber pressure.

The major improvement here is the cool flame detection method. A high-sensitivity monochrome CCD camera with high relative response in the UV spectrum (CCE-B013-U) was used to capture the global chemiluminescence from the low-temperature chemical reactions, which indicated the intensity of the cool flame similar to Zhao *et al.* [168]. The exposure time of the UV camera is the same 6 seconds for all cases. The ignition/extinction states of the cool flame were determined by gradually changing the oxidizer boundary temperature for a given fuel/oxidizer flow rate, until the chemiluminescence signal of the cool flame respec-

tively emerged/disappeared as detected by the camera. The ignition and extinction temperatures were quantified with the corresponding oxidizer boundary temperatures measured with an uncoated K-type (Chromel-Alumel) thermocouple after radiation correction as in Sec. 2.1.

In the following discussion, a fuel stream consisting of 50% DME and 50% nitrogen at room temperature was issued from the lower nozzle and impinged onto the heated oxidizer stream from the upper nozzle. The oxygen volume fraction in the oxidizer stream varied from 21% to 25%, and the ambient pressure varied from 2 to 3 atm for ignition and extinction measurements. The global strain rate used in the following discussion is defined as the pressure-weighted gradient of the axial flow velocity [136]. The experimental affirmation of the distinctive ignition and extinction behavior of nonpremixed cool flame is first demonstrated to validate the computational prediction. Then, the thermal and chemical structures of the reacting layer in the counterflow system at cool flame ignition, steady cool flame, and cool flame extinction conditions are analyzed, elucidating the dominant chemical pathways for each condition. Possible reasons for the discrepancies between experiments and computations are discussed. Finally, the effects of ambient pressure and oxygen concentration on ignition and extinction are discussed.

#### 2.4.2 Hysteretic Ignition and Extinction Behavior

What differentiates a strained cool flame from a reacting mixture going through slow oxidation in a heated flow is the hysteretic ignition and extinction behavior. Such hysteretic behavior has already been illustrated with an S-curve analysis shown in Fig. 2.5 but is further explained in Fig. 2.10. The numerical code and chemical model adopted here are the same as in Sec. 2.2. *A posteriori* analysis based on the optically thin radiation model, with radiative properties based on the RADCAL model by Grosshandler of NIST [56] shows that the radiative heat loss is minimal, and therefore

radiation is not included in the current computation. At a fixed strain rate, by gradually increasing the air boundary temperature and hence the reactivity and heat generation rate within the flow, at some point within the flow the temperature will exceed the boundary temperature and eventually lead to self-sustained burning. Such a transition state I is defined as the ignition point, and the condition after ignition that is located on the upper steady branch of the S-curve is designated as point S, representing a steady cool flame. The difference in the maximum temperatures between points S and I primarily results from the heat release from the cool flame. As this temperature decreases from point S, the maximum temperature in the flow field also decreases, following the upper branch trajectory, until the flame extinguishes at point E. The difference in the air boundary temperature between points I (or S) and E demonstrates the hysteresis between the ignition and extinction of the flame.

To capture this computationally predicted hysteresis, the ignition and extinction temperatures were experimentally measured in the counterflow configuration based on the chemiluminescence of the cool flame. Figure 2.11 shows representative images of the ignition and extinction detection for the DME/air cool flame at 2 atm and pressure-weighted strain rate of  $84 \text{ /s}$ . Ignition of the cool flame is achieved by gradually increasing the oxidizer boundary temperature. As shown in the left column of Fig. 2.11, when the oxidizer boundary temperature is slowly increased from 626 K to 637 K (A to D), the chemiluminescence from the low-temperature chemistry suddenly becomes detectable by the UV camera, indicating onset of the cool flame. The oxidizer boundary temperature is then gradually reduced with a temperature interval of 1 K, while maintaining quasi-steadiness at each step. The right column of Fig. 2.11 then shows that, while the cool flame chemiluminescence remains as the boundary temperature is decreased from 637 K to 626 K (E to H), it suddenly vanishes at 626 K, which was thus defined as the extinction temperature.

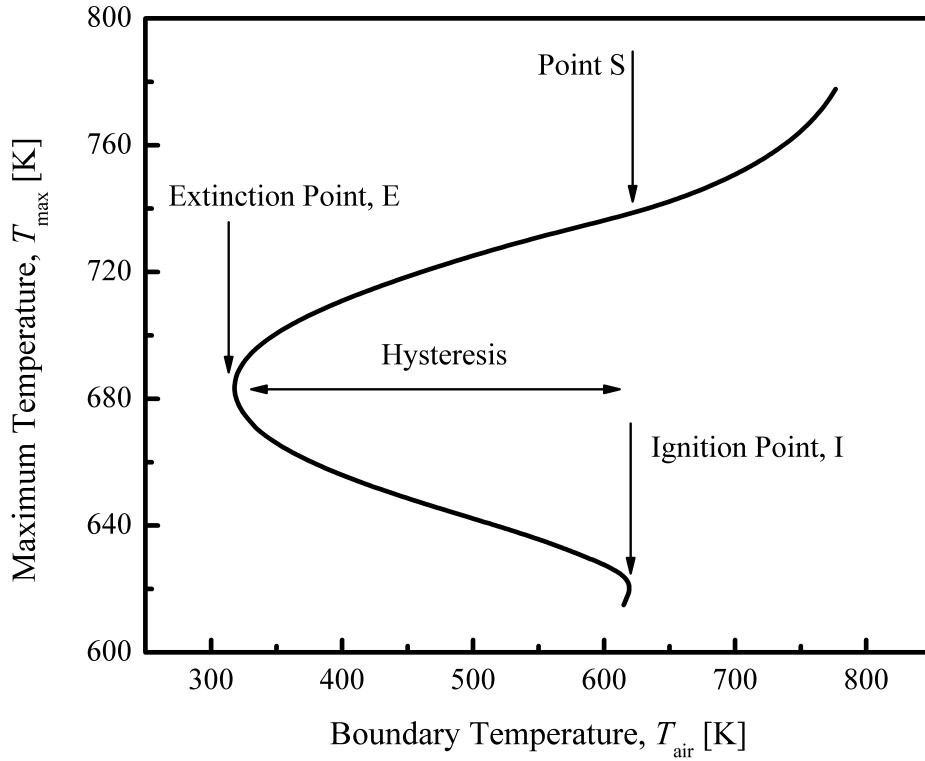


Figure 2.10: S-curve analysis of the response of nonpremixed counterflow of 50% DME and 50% nitrogen versus heated air at the 2 atm and pressure-weighted strain rate of 80 /s.

The same procedure was followed to obtain the ignition and extinction temperatures at various strain rates for comparisons with the computationally predicted values, as shown in Fig. 2.12. Results from experiment and computation then both show that the ignition and extinction temperatures increase with increasing strain rate, due to reduced residence time. Furthermore, the ignition temperature not only is higher than the extinction temperature at a given strain rate, it is also less sensitive to the strain rate, resulting in a less pronounced ignition-extinction hysteresis. Noting that the repeatability of the measurement is within 2 K, which is within the marker size in the figure, and the error bar represents the uncertainty of the radiation correction using different models, comparison between the experimental data should

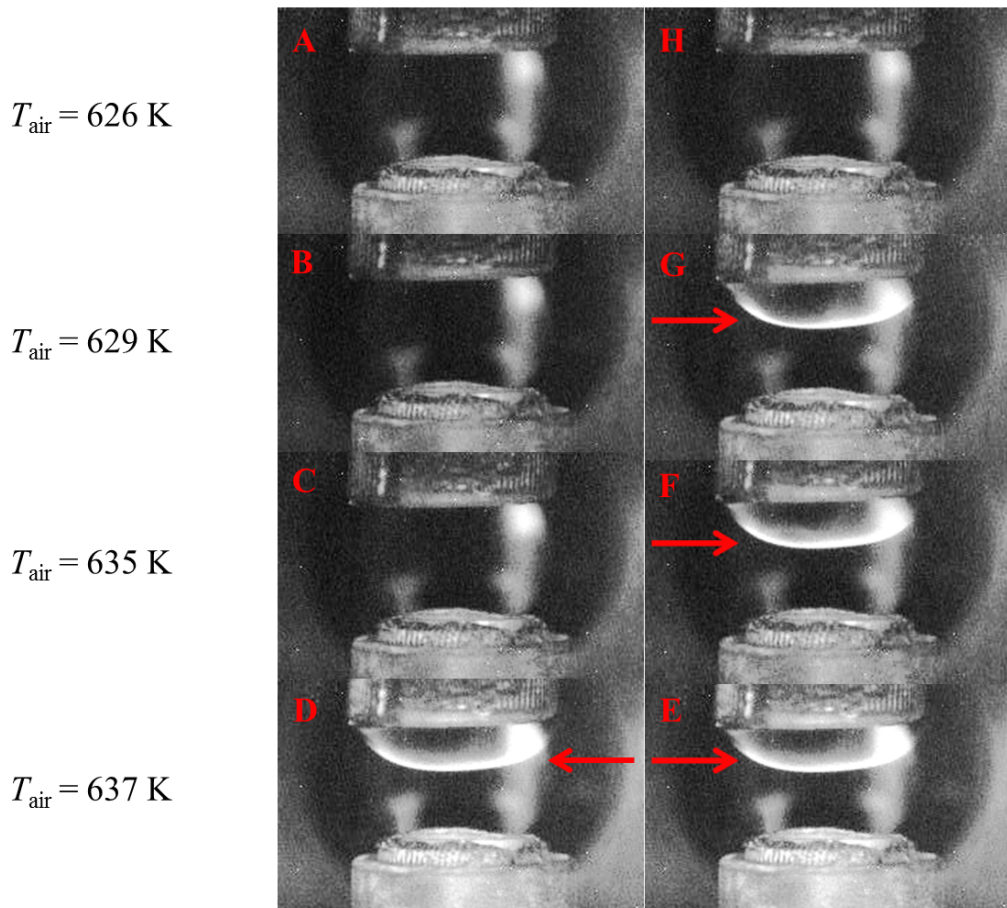


Figure 2.11: Flame images demonstrating the hysteretic nature of ignition and extinction of cool flames with air temperature. DME cool flame at 2 atm and pressure-weighted strain rate of 84 /s; DME volume fraction in the fuel stream is 50%, and the oxidizer stream is air.

be made based on the upper or lower bound of the uncertainty bar across all the measurements.

It is also apparent from Fig. 2.12 that while the experimental and computational results separately exhibit the anticipated physics, namely the extinction temperature is lower than the ignition temperature, and they both increase with increasing strain rate, the quantitative comparison between them is overall poor, both in magnitude as well as the strain-rate sensitivity. Detailed analysis of these discrepancies is deferred to Sec. 2.4.4.

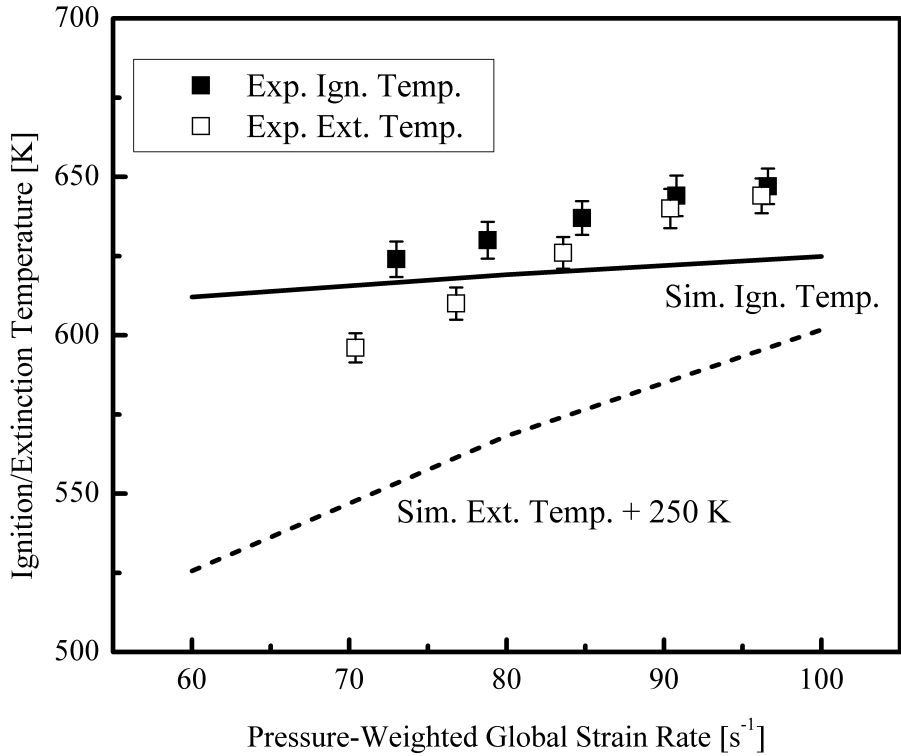


Figure 2.12: Experimental and computed ignition and extinction temperatures at 2 atm and various strain rates. The computed extinction temperature is shifted up by 250 K for better illustration. DME volume fraction in the fuel stream is 50%, and the oxidizer stream is air.

### 2.4.3 Analysis of Thermal and Chemical Structures

In order to elucidate the dominant chemical pathways and evolution of the ignition and extinction processes, the three characteristic points on the S-curve of Fig. 2.10, which respectively represent the states prior to ignition (point I), steady burning (point S), and prior to extinction (point E), were chosen for structural analysis.

As shown in Fig. 2.13, the heat release just prior to the initiation of the cool flame is negligible, and the maximum temperature in the flow field is set by the oxidizer boundary. For both steady flames at points S and E, there are reaction kernels delineated by the heat release profiles. Based on the full width at half maximum of

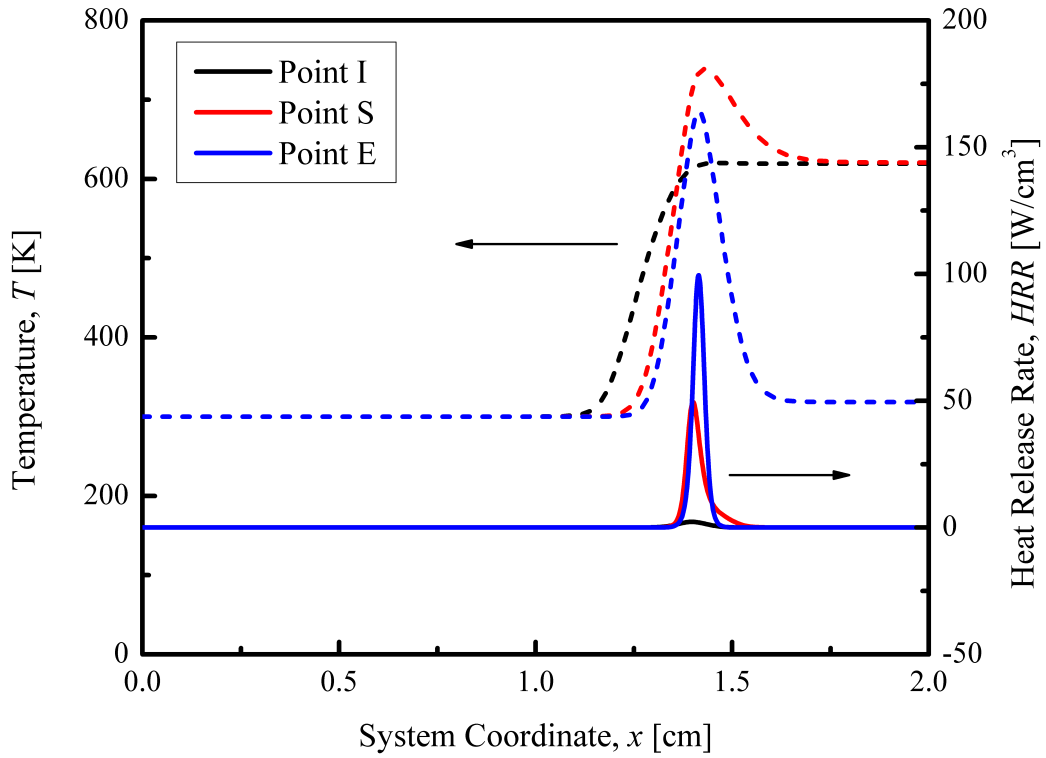


Figure 2.13: Thermal structures in the computed flow field at three representative points on the S-curve shown in Fig. 2.10. Fuel stream boundary conditions are specified at  $x = 0$  in the computation.

the heat release profile, a typical cool flame thickness is about 0.5 mm for the present conditions. At point E, the heat release rate of the cool flame is higher than that at point S, for low-temperature chemistry is favored at relatively lower temperatures. However, the steep gradient of the heat release profile indicates that heat loss to the boundary at point E is more pronounced compared to point S. As the boundary temperature further decreases, such heat loss increases, and chemical reactions cannot keep up with heat loss from the reaction zone, leading to extinction due to the limited residence time in the strained flow.

The profiles of three representative species, specifically, methoxymethylperoxy ( $\text{CH}_3\text{OCH}_2\text{O}_2$ ), formaldehyde ( $\text{CH}_2\text{O}$  or  $\text{HCHO}$ ), and hydroxyl ( $\text{OH}$ ), were then in-

vestigated to elucidate the chemical structures at these three points, I, S, and E, as shown in Figs. 2.14 to 2.16. The methoxymethylperoxy radical was chosen because it is a representative species for the low-temperature chemistry [80]. Comparing the species profiles of the three states, it is seen that the  $\text{CH}_3\text{OCH}_2\text{O}_2$  mass fraction increases upon flame initiation, and, similar to the heat release rate profile, its peak increases as extinction is approached. Moreover, the profile broadens, for low-temperature chemistry is favored at reduced oxidizer boundary temperature. Formaldehyde was selected because it is a major product of the cool flame, with its intensity manifested through its chemiluminescence [168]. It is then seen that: negligible  $\text{CH}_2\text{O}$  is formed prior to ignition, significant amount is formed in the steady flame, and the concentration and hence the intensity of chemiluminescence is reduced as extinction is approached. Finally, the hydroxyl radical was chosen because it represents high-temperature flame chemistry and is also an important radical formed during the chain branching reactions of the low-temperature chemistry. It is then noted that the peak mass fraction of OH is several orders of magnitude smaller than those in a typical hot flame. The ignition of a cool flame is initiated with a peak formation of OH, which subsequently decreases upon ignition. With subsequent heat release from the cool flame, a second peak of OH mass fraction emerges on the oxidizer side of the cool flame peak, which is responsible for the initiation of the hot flame at higher boundary temperatures [82].

Finally, sensitivity analysis was conducted to elucidate the evolution of the dominant chemical pathways during the ignition and extinction processes. The maximum temperature was chosen as the target for sensitivity analysis, and the ratio of the relative change of the maximum temperature to that of the Arrhenius factor of each reaction being perturbed was defined as the sensitivity coefficient. The sensitivity coefficients of all the reactions considered in the chemical mechanism were normalized

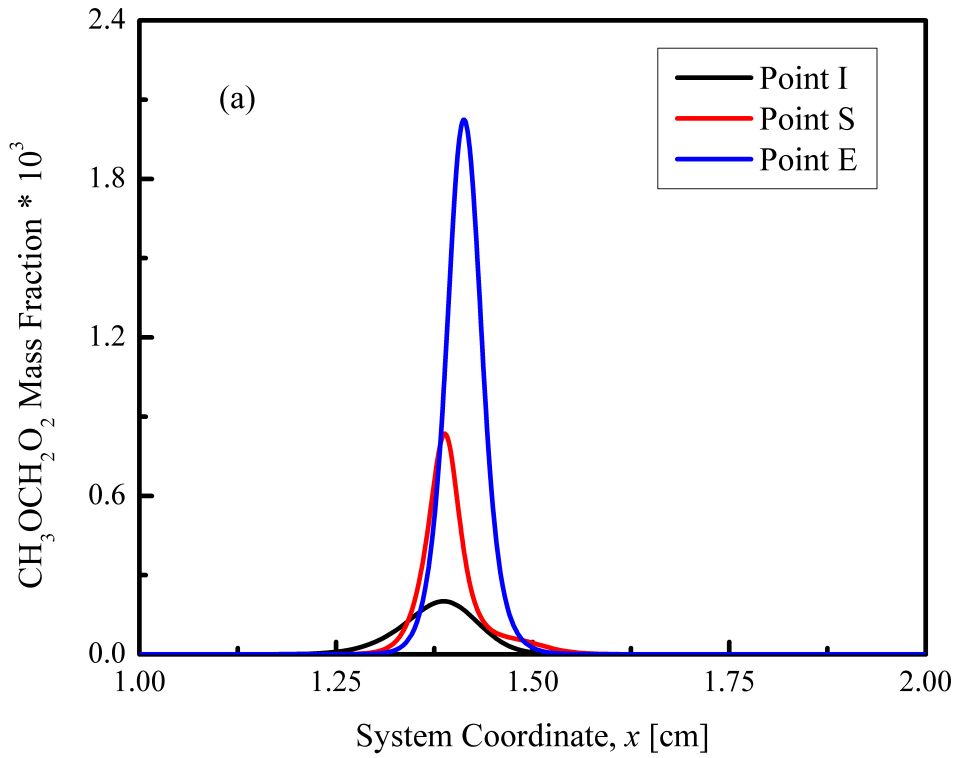


Figure 2.14: Species profiles in the computed flow field at three representative points on the S-curve shown in Fig. 2.10: methoxymethylperoxy radical. Fuel stream boundary conditions are specified at  $x = 0$  in the computation.

by the maximum value such that the normalized sensitivity coefficient is bounded by -1 and 1 to allow for comparisons between the cases.

The normalized sensitivity coefficients ranked by their absolute values for states I, S, and E in Fig. 2.10 are shown in Fig. 2.17. At all three states, low-temperature chemistry is dominant, with the absence of the typical high-temperature chain branching reactions such as  $\text{H} + \text{O}_2 \rightleftharpoons \text{OH} + \text{O}$ . Similar to the ignition analysis in Sec. 2.3.2, the isomerization reaction  $\text{CH}_3\text{OCH}_2\text{O}_2 \rightleftharpoons \text{CH}_2\text{OCH}_2\text{O}_2\text{H}$  and the oxygen addition reaction  $\text{CH}_2\text{OCH}_2\text{O}_2\text{H} + \text{O}_2 \rightleftharpoons \text{O}_2\text{CH}_2\text{OCH}_2\text{O}_2\text{H}$  promote ignition, while the reaction  $\text{CH}_2\text{OCH}_2\text{O}_2\text{H} \rightleftharpoons \text{OH} + 2\text{CH}_2\text{O}$  retards it. However, for the steady cool flames corresponding to points S and E, the relative importance of these reactions shifts.

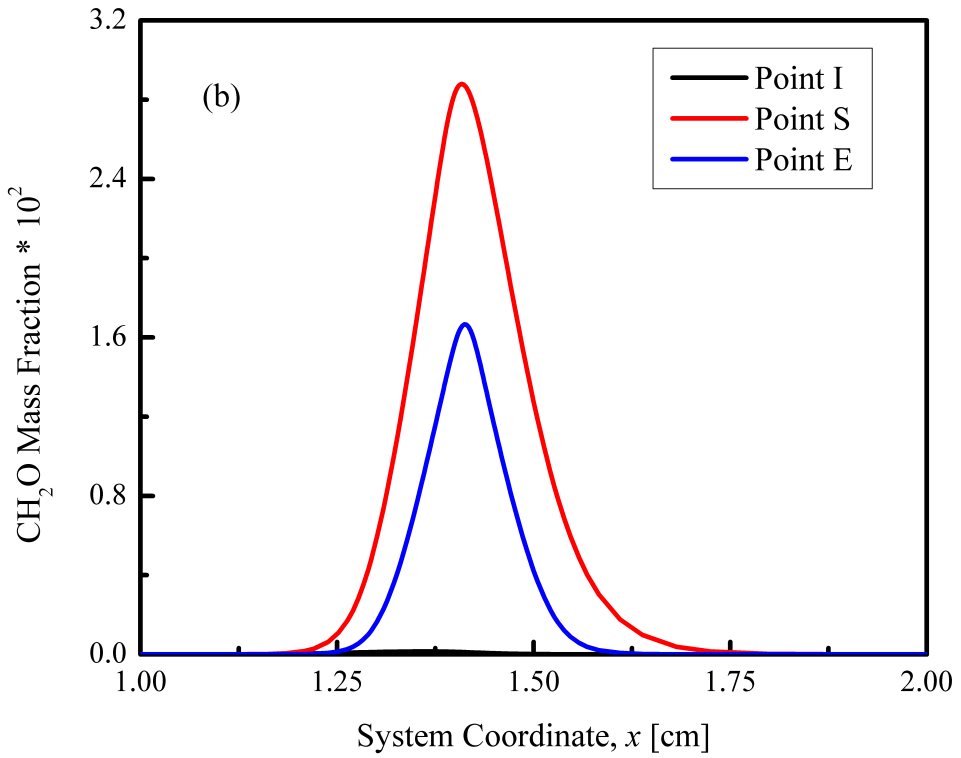


Figure 2.15: Species profiles in the computed flow field at three representative points on the S-curve shown in Fig. 2.10: formaldehyde. Fuel stream boundary conditions are specified at  $x = 0$  in the computation.

First,  $\text{CH}_2\text{OCH}_2\text{O}_2\text{H} + \text{O}_2 \rightleftharpoons \text{O}_2\text{CH}_2\text{OCH}_2\text{O}_2\text{H}$  becomes even more important in steady cool flames. Since the maximum temperature was chosen as the target to evaluate the sensitivity, the exothermic reaction  $\text{CH}_2\text{OCH}_2\text{O}_2\text{H} + \text{O}_2 \rightleftharpoons \text{O}_2\text{CH}_2\text{OCH}_2\text{O}_2\text{H}$  demonstrates a large positive sensitivity coefficient. Conversely, at ignition, reactions that finally lead to radical runaway are more important, for heat release from the mixing layer is negligible at this state, as shown in Fig. 2.13. Second, the isomerization reaction  $\text{CH}_3\text{OCH}_2\text{O}_2 \rightleftharpoons \text{CH}_2\text{OCH}_2\text{O}_2\text{H}$  becomes important again near extinction, for, at extinction, the radical production rates barely keep up with the transport losses and the chain carrying limiting step becomes crucial again.

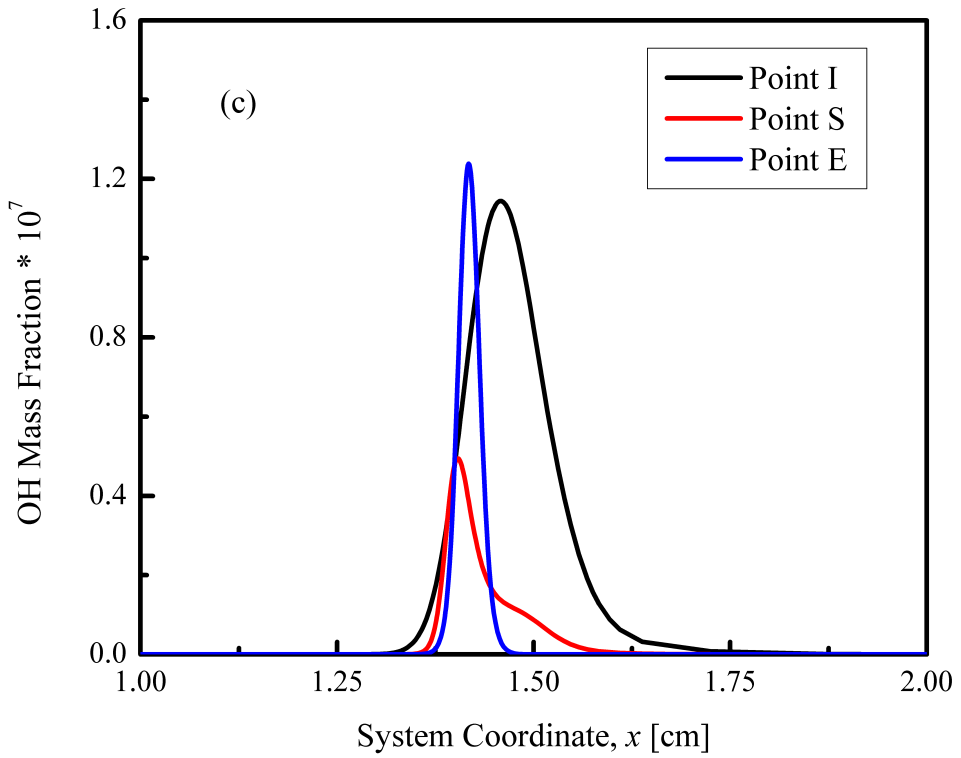


Figure 2.16: Species profiles in the computed flow field at three representative points on the S-curve shown in Fig. 2.10: hydroxyl radical. Fuel stream boundary conditions are specified at  $x = 0$  in the computation.

#### 2.4.4 Uncertainty Analysis

As noted in Fig. 2.12, while the computation is able to capture the experimental observation of the hysteretic feature of ignition and extinction, as well as the increasing trend of ignition and extinction temperatures with increasing strain rate, the quantitative agreement is rather poor. Specifically, the ignition temperature is slightly overpredicted; its sensitivity to strain rate, indicated by the slope of the ignition temperature profile, is substantially underpredicted; and, most importantly, the extinction temperature is significantly underpredicted. Upon extensive exploration of the various experimental and modeling factors that could contribute to such sub-

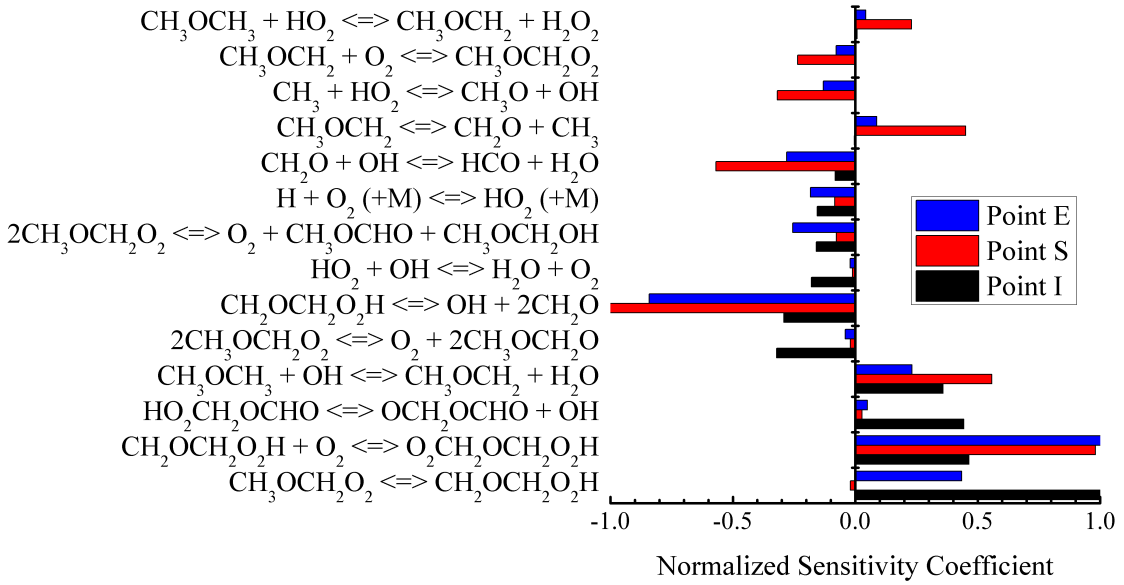


Figure 2.17: Reaction sensitivity analysis at three representative points on the S-curve shown in Fig. 2.10.

stantial disagreements, the uncertainty of the low-temperature chemistry used in the computation has surfaced to be the dominant factor.

To demonstrate the effects of such uncertainty and since the ignition temperatures of the cool flames are fairly well captured, it is reasonable to inspect reactions with large sensitivity coefficients in Fig. 2.17 for the cool flames. This leads to the identification of the reactions:  $\text{CH}_2\text{OCH}_2\text{O}_2\text{H} + \text{O}_2 \rightleftharpoons \text{O}_2\text{CH}_2\text{OCH}_2\text{O}_2\text{H}$  and  $\text{CH}_2\text{OCH}_2\text{O}_2\text{H} \rightleftharpoons \text{OH} + 2\text{CH}_2\text{O}$ . Since cool flames appear to be more robust to extinguish, the preexponential factors of these two reactions were modified by respectively reducing and increasing to 70% and 200% of their original values.

Figure 2.18 then shows that both qualitative and quantitative agreements between experiments and computations are achieved with the modified reaction parameters. Specifically, although the magnitude of the ignition temperature is not very sensitive to the modifications, as expected, its sensitivity to increasing strain rate is enhanced, for the modifications essentially slow down the low-temperature chemistry such that the sensitivity to finite residence time is more pronounced. More importantly, it is

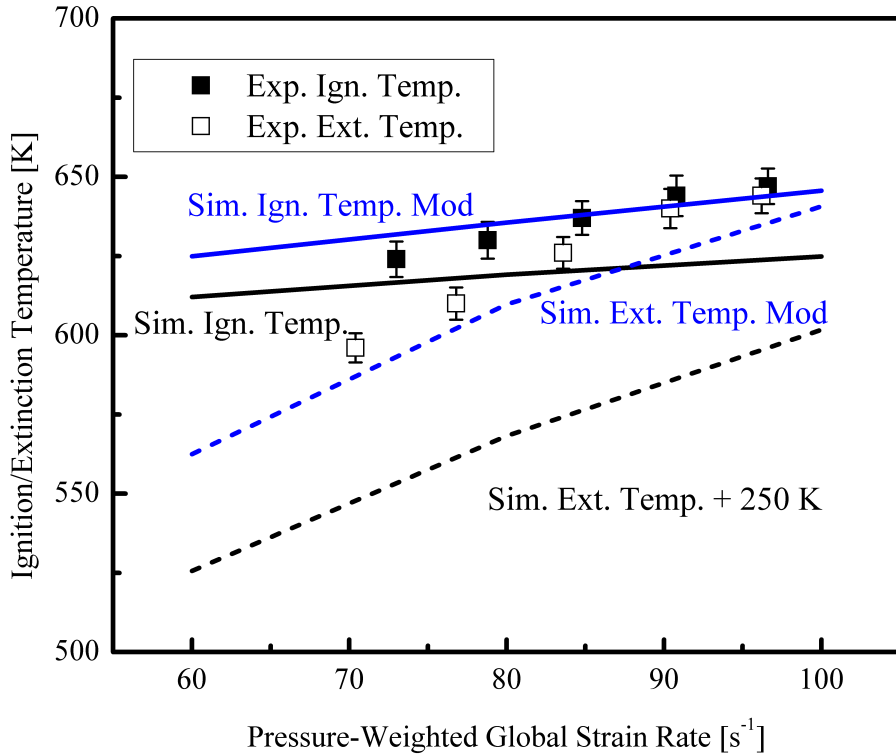


Figure 2.18: Revisit of Fig. 2.12 with modified reaction rates in the chemical mechanism. Note that the line plots with the modified reaction rates are presented without shifting.

seen that good agreement is also achieved for the highly sensitive extinction temperatures, significantly boosting their values but without changing the sensitivity to the strain rate variation.

While the above results appear to be encouraging, it should be noted that the objective of this study is not to propose an improved chemical model with the modified kinetic parameters. What has however been demonstrated is the sensitive nature of the low-temperature chemistry, in that substantial change in the global response can result with even small changes in these preexponential factors. In this regard, it is further noted that, during the development of the low-temperature chemical model, the validation data is limited to those from homogeneous systems. Clearly

additional validation data on cool flames covering a wider range of conditions, which are inherently present in flame systems, is needed for the eventual development of a viable chemical model.

Another factor that could potentially affect the accuracy of the comparison between the experimental and computational results is the experimental detection limit of the UV camera, which could be too high compared to the chemiluminescence emission of the cool flame near extinction. Since the hysteresis temperature window was observed in the experiment at various conditions, the detection threshold of the UV camera should be lower than the chemiluminescence intensity of the steady cool flame upon ignition. Consequently, the ignition temperatures for these cases should be well captured. However, the lower bound of the hysteresis temperature window could be limited by the detection threshold, and therefore, the actual extinction temperatures might not be captured accurately.

#### 2.4.5 Effects of Pressure and Oxygen Concentration

The effects of ambient pressure and oxygen concentration in the oxidizer stream on the ignition and extinction of the cool flames were also investigated. Pressure effects were first computationally studied by fixing the oxygen mole fraction in the oxidizer stream at 21% and fixing the pressure-weighted strain rate at 100 /s, as shown in Fig. 2.19. It is seen that, as the pressure increases from 2 to 5 atm, the ignition temperature decreases and the heat release from the cool flame becomes more pronounced, as indicated by the temperature differences between the ignition turning point and the point on the cool flame branch with the same boundary temperature. Moreover, the extinction turning point shifts to a lower boundary temperature, resulting in an extended hysteresis temperature window. Conversely, the extent of the low-temperature chemistry governed S-curve hysteresis diminishes with decreasing pressure, leading to its absence at 0.5 atm.

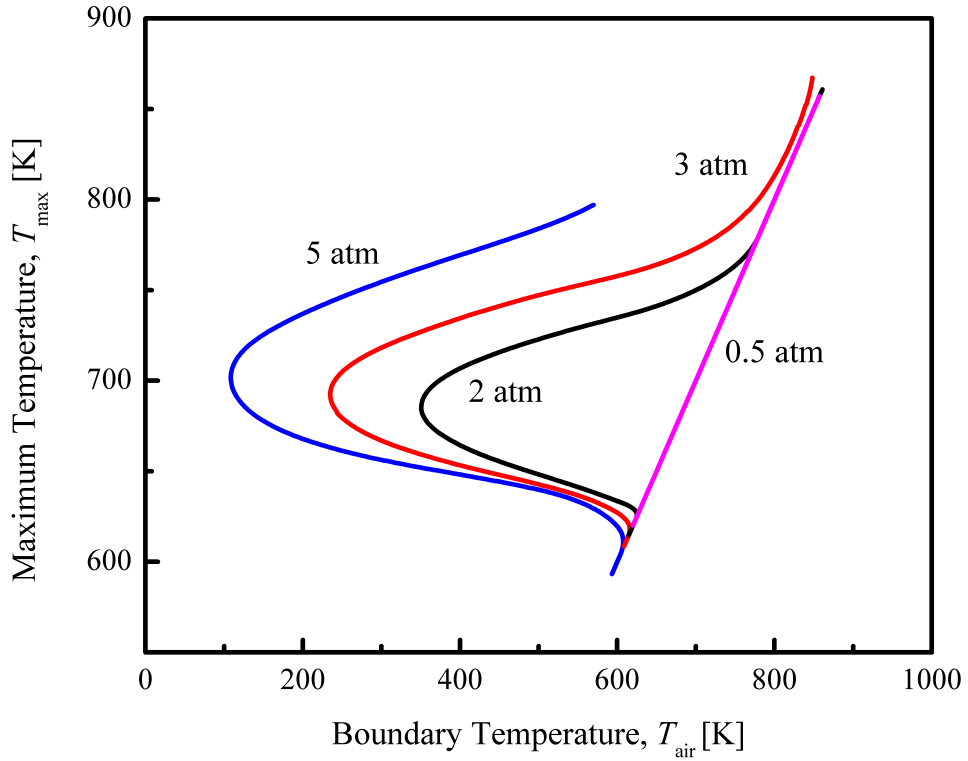


Figure 2.19: S-curve analysis for various ambient pressures and pressure-weighted strain rate of 100 /s. DME volume fraction in the fuel stream is 50%, and the oxidizer stream is air.

The conclusion that elevated pressure promotes low-temperature chemistry is consistent with previous studies with *n*-heptane [82]. Such promotion effect can be explained with the sensitivity analysis in Sec. 2.4.3. Qualitatively, sensitivity analysis conducted for elevated pressures shows similar dominant chemical pathways as Fig. 2.17. At elevated pressures, the balance of the reaction  $\text{CH}_2\text{OCH}_2\text{O}_2\text{H} + \text{O}_2 \rightleftharpoons \text{O}_2\text{CH}_2\text{OCH}_2\text{O}_2\text{H}$  shifts forward and promotes the formation of the important intermediate radicals for low-temperature chemistry. Moreover, the  $\text{CH}_2\text{OCH}_2\text{O}_2\text{H} \rightleftharpoons \text{OH} + 2\text{CH}_2\text{O}$  reaction is retarded at elevated pressures.

Figures 2.20 and 2.21 further show that the experimental ignition and extinction temperatures decrease at elevated pressures. It is seen that while the effects of ele-

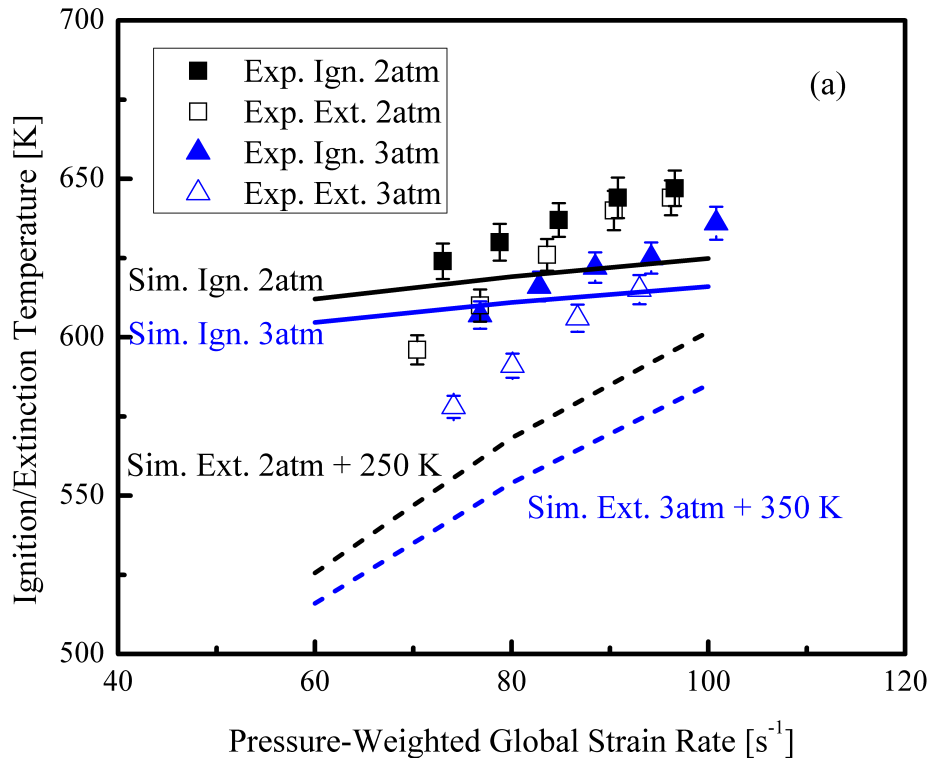


Figure 2.20: Ignition and extinction temperatures at various strain rates and pressures in experiments and computations with the original chemical model. Some of the computed extinction temperatures are shifted up for better illustration. DME volume fraction in the fuel stream is 50%, and the oxidizer stream is air.

vated pressure on ignition temperatures are predicted by computations qualitatively, the effects on extinction temperatures are significantly overpredicted when using the original mechanism (Fig. 2.20). The comparison is improved by using the two modified reactions (Fig. 2.21), although the degree of improvement is less satisfactory as for the case of 2 atm pressure, shown in Fig. 2.18. It is emphasized again that it is preferred that the comparison is left as is, without further tuning the reactions as it does not seem to be justified within the scope of the present study.

Figure 2.22 shows that increasing the oxygen concentration extends the hysteresis temperature window of the cool flame at the same ambient pressure and strain rate, while the ignition temperature is almost unaffected except at very low concentrations.

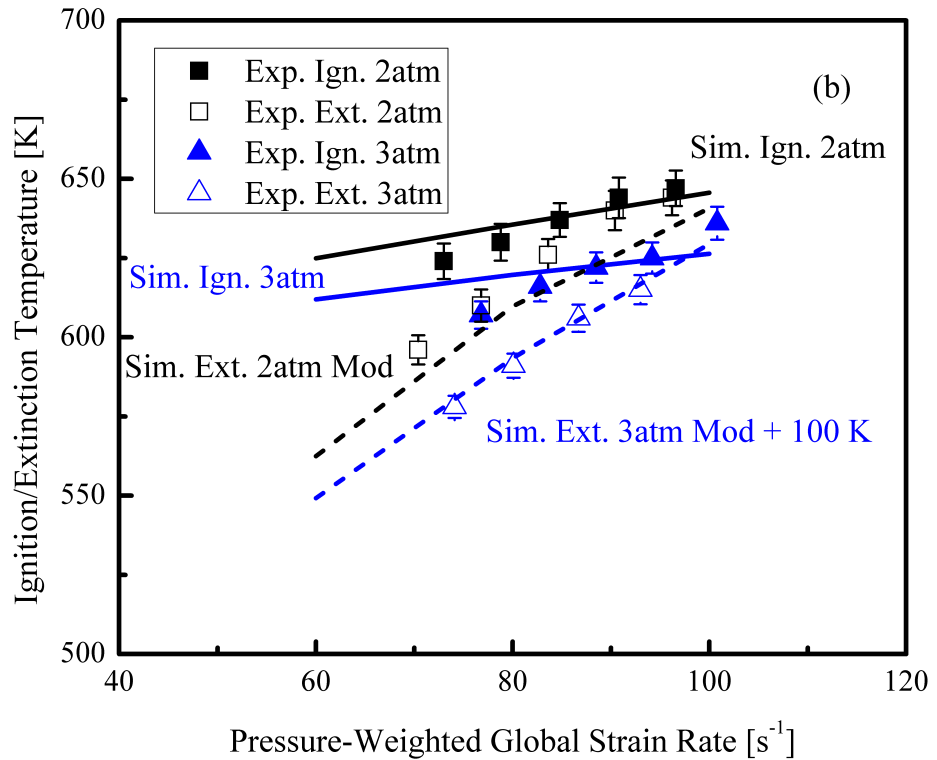


Figure 2.21: Ignition and extinction temperatures at various strain rates and pressures in experiments and computations with the modified chemical models. Some of the computed extinction temperatures are shifted up for better illustration. DME volume fraction in the fuel stream is 50%, and the oxidizer stream is air.

This is because, with increased oxygen concentration and hence decreased inert concentration, the heat release from the cool flame becomes more pronounced, which results in decreased extinction temperature. Dominant chemical pathways for these conditions are similar to those in Fig. 2.17.

The insensitivity of the cool flame ignition temperature is further confirmed with the experimental measurements, as shown in Fig. 2.23. However, the reduction effect of increased oxygen concentration on the cool flame extinction temperature is again overpredicted by the computation, while improved agreements are achieved with the two modified preexponential factors (Fig. 2.24).

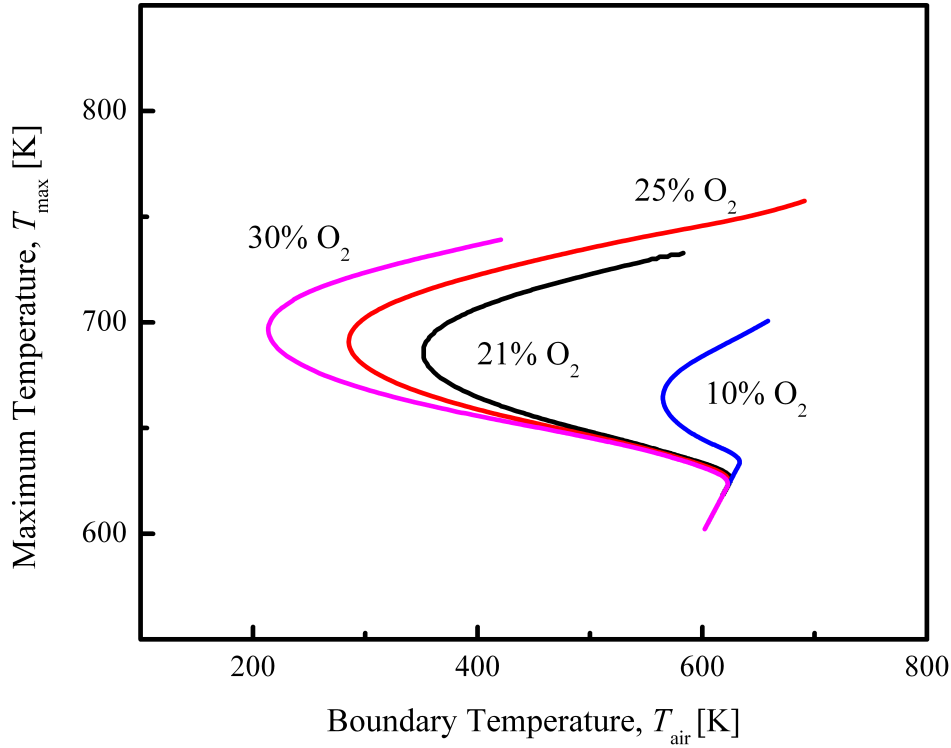


Figure 2.22: S-curve analysis for various oxygen concentrations and the pressure-weighted strain rate of 100 /s. DME volume fraction in the fuel stream is 50%, and the ambient pressure is 2 atm.

## 2.5 Summary

In this chapter, S-curve analysis was performed computationally to demonstrate the distinctive ignition and extinction states and structures of nonpremixed DME counterflow cool flames at various strain rates, ambient pressures, and fuel and oxidizer concentrations. The design of the experimental counterpart to substantiate the computational investigation is very challenging due to the limited heat release and species production in cool flames and lack of robustness of such flames. Qualitatively, the cool flame reactivity was substantiated with the “M” shaped signal captured by the PMT-oscilloscope system. The ignition of the cool flame at atmospheric pressure was quantified with sensitive infrared imaging.

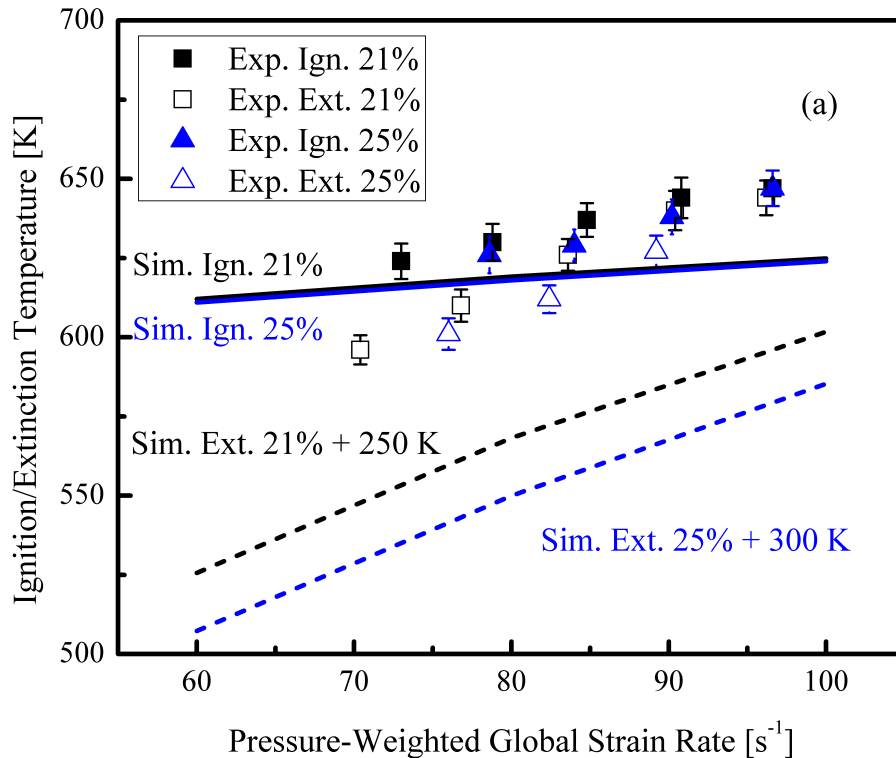


Figure 2.23: Ignition and extinction temperatures at various strain rates and oxygen concentrations in experiments and computations with the original chemical model. Some of the computed extinction temperatures are shifted up for better illustration. DME volume fraction in the fuel stream is 50%, and the ambient pressure is 2 atm.

Realizing that elevated pressure promotes cool flames and the limitation of the infrared experimental system, the detection method was improved with UV camera imaging. The hysteretic ignition and extinction behavior of the nonpremixed cool flame was then observed and quantified in experiments for the first time. It is noted, however, the extinction behavior of the cool flame was less well predicted by computation compared to ignition. Possible reasons for such discrepancies were discussed, including experimental uncertainties and the high sensitivity in some reaction rates. Although the objective of this chapter is not to propose an improved chemical model with modified kinetic parameters, it demonstrates the sensitive nature of the

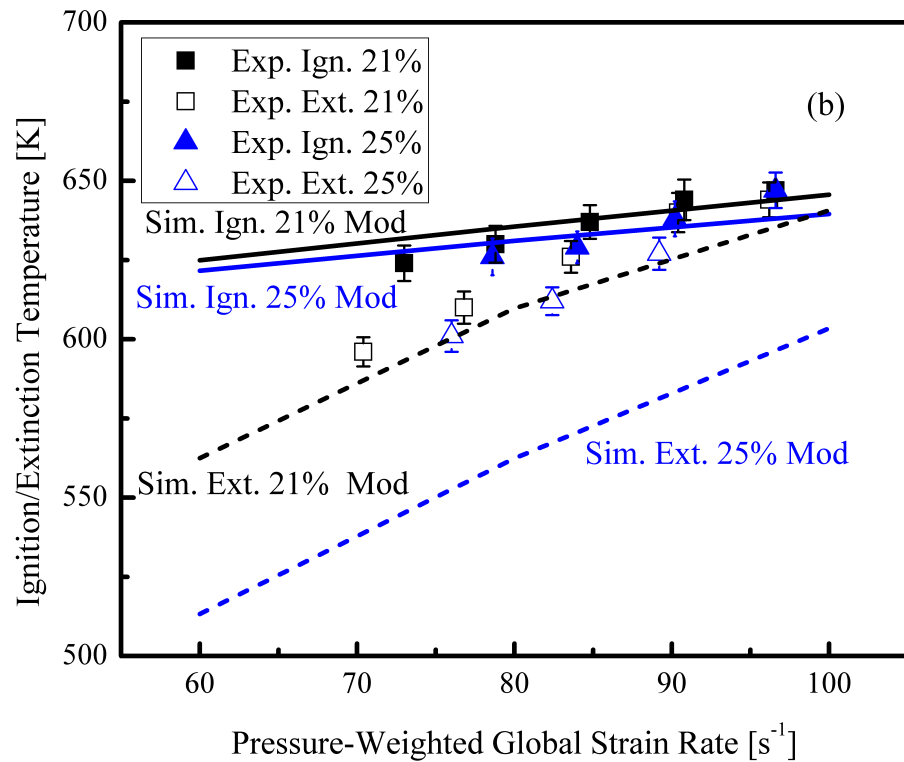


Figure 2.24: Ignition and extinction temperatures at various strain rates and oxygen concentrations in experiments and computations with the modified chemical models. Some of the computed extinction temperatures are shifted up for better illustration. DME volume fraction in the fuel stream is 50%, and the ambient pressure is 2 atm.

low-temperature chemistry, which stresses the need for further investigation on the low-temperature chemical kinetics.

# Chapter 3

## Flame Dynamics at Engine Conditions

In this chapter, laminar nonpremixed coflow flame dynamics are studied computationally at elevated temperatures and pressures to activate autoignition. Realizing practical engines work under turbulent and autoignitive conditions with unsteadiness in the inlet flows, the work presented in this dissertation starts with steady laminar flow and then goes to unsteady laminar flow, gradually adding flow complexities to bridge laminar and turbulent studies. Lifted flame stabilization at elevated temperatures and pressures is first presented to elucidate the role of autoignition in flame stabilization in addition to the traditional tribrachial flame stabilization. Responsible for the first stage autoignition and heat release, the role of low-temperature chemistry, presented in Chapter 2, is investigated. The thermal and chemical structures of the lifted flame are described with heat release and selected species profiles. The evolution of the controlling chemical pathways are subsequently identified with Chemical Explosive Mode Analysis (CEMA) and the stabilization mechanism determined with Lagrangian Flamelet Analysis (LFA). Different stabilization mechanisms are identified, and a regime diagram is proposed to demonstrate the shift of the stabilization

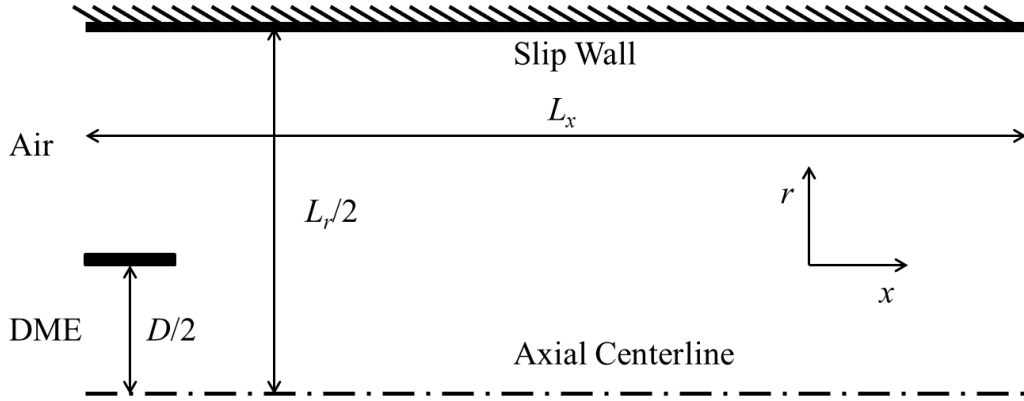


Figure 3.1: A schematic of the coflow configuration adopted in all of the steady and unsteady cases.

mechanism as flow condition varies. The complexity of unsteadiness is then added to the investigated problem by examining flame dynamics in an oscillating flow. Consequently, the chemistry-transport coupling effects on the shift of combustion modes in oscillating flows under autoignitive conditions are elucidated.

### 3.1 Computational Details

The flow configuration is an axisymmetric DME stream at 300 K in a heated coflow of air at 30 atmospheres. The fuel nozzle diameter  $D$  is 0.8 mm, and the fuel and air are initially separated with an adiabatic, no-slip wall with thickness  $D/20$ . The schematic of this coflow configuration is provided in Fig. 3.1. The coflow outer boundary is specified as an adiabatic slip wall, and its diameter is large enough such that increasing the width of the domain does not influence the computation. Uniform inlet velocities were specified for both fuel and air streams to establish lifted flames. For the unsteady establishment of the flame, a convective outflow is utilized at the outlet boundary, which simplifies to a Neumann condition for the steady problem.

The flow field was initialized on a coarse mesh within a large domain. At first, all the chemical source terms were set to zero until the nonreacting flow reached steady-state. Chemical source terms were then activated; the mixture autoignited; and the flow field reached steady-state. The domain was then truncated, and the mesh was refined to fully resolve the chemical structure. All the results presented in Secs. 3.2 and 3.3 were obtained from the steady-state solutions.

The Navier-Stokes equation with buoyancy in the streamwise direction and the conservation equations of mass, species, and temperature were solved. The species diffusivities were determined from a constant, nonunity Lewis number. The Lewis numbers for individual species were pre-calculated from a one-dimensional flamelet with the same boundary conditions and the mixture-averaged transport model and evaluated at the maximum temperature location. The conserved scalar mixture fraction  $Z$  was specified as unity and zero for the fuel jet and coflow at the inlet, respectively, and computed by solving its transport equation with unity Lewis number [123]. This definition of mixture fraction is consistent with the one used in the flamelet calculation in Sec. 3.2.2.

Dimethyl ether was chosen in this work, for it is a clean biofuel and one of the smallest hydrocarbons exhibiting NTC behavior. The same skeletal mechanism [5] is utilized as in Chapter 2.

The low-Mach number formulation of the governing equations is solved using NGA, which is based on the numerical methods of Desjardins *et al.* [29]. The momentum and scalar equations are discretized with a second-order centered scheme and a third-order WENO scheme [92], respectively, on a staggered mesh. The iterative second-order semi-implicit Crank-Nicolson scheme of Pierce and Moin [120] is adopted for temporal integration. At each time step, the chemical source terms for the species and energy equations are evaluated independently from the transport terms using the CVODE package [19].

Uniform grids in the axial direction were adopted for the computations, and the grid spacing was set as  $\Delta x = 2.2 \mu\text{m}$ . A nonuniform grid was used in the radial direction with a minimum spacing of  $2.5 \mu\text{m}$  to resolve the mixing layer corresponding to the separation wall and geometric progression stretch rates less than 3% towards both the centerline and the outer boundary. The dimensions of and number of grid points in the computational domain for each computation are introduced in the following sections.

A grid convergence study was performed for the air temperature 800 K case at 3.2 m/s, for it has the most complex structure, which is discussed in the following sections. As shown in Fig. 3.2, grid convergence was achieved for velocity, temperature, and species profiles. Grid convergence was also verified for the air temperature 1100 K case, which shows similar results and is therefore not shown here.

## 3.2 Flame Stabilization: Boundary Temperature Effects

In this section, the effect of boundary temperature on flame stabilization is investigated. Therefore, in all cases studied in this section, the boundary velocities of the DME jet as well as the coflow air are fixed at 3.2 m/s. Conversely, the temperatures of the heated air coflow are 700, 800, 900, and 1100 K. The dimensions of and number of grid points in the computational domain for each computation are summarized in Table 3.1.

### 3.2.1 Thermal and Chemical Structure

To visualize the flame structures, the heat release rate profiles for the four cases (700, 800, 900, and 1100 K) are shown in Fig. 3.3. Qualitatively, the most upstream point

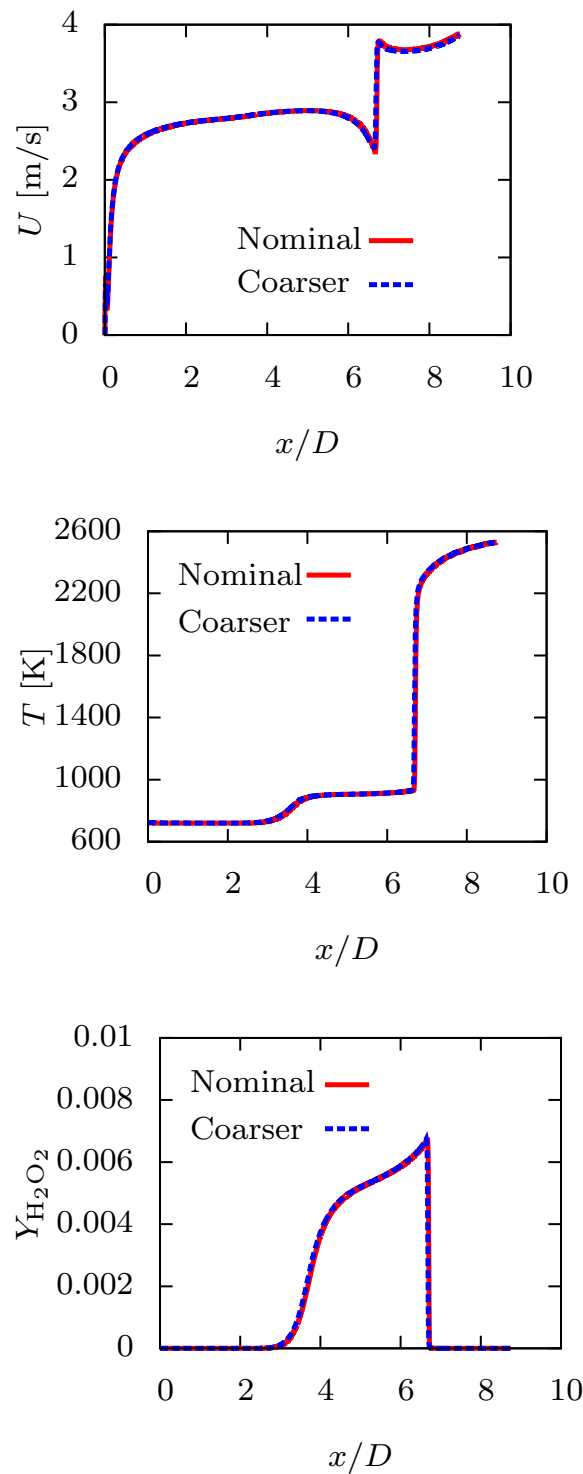


Figure 3.2: Velocity, temperature, and  $H_2O_2$  profiles along  $Z_{st}$  on the nominal and two times coarser (in each direction) meshes for an air temperature of 800 K.

Table 3.1: Computational domain and number of grid points for steady cases with the same flow velocities but different boundary temperatures.

Coflow Temperature [K]	700	800	900	1100
$L_x$ [mm]	28	7	3.5	3
$L_r$ [mm]	6	3.9	3.9	6
$N_x$	12290	3072	1536	1282
$N_r$	192	176	176	192

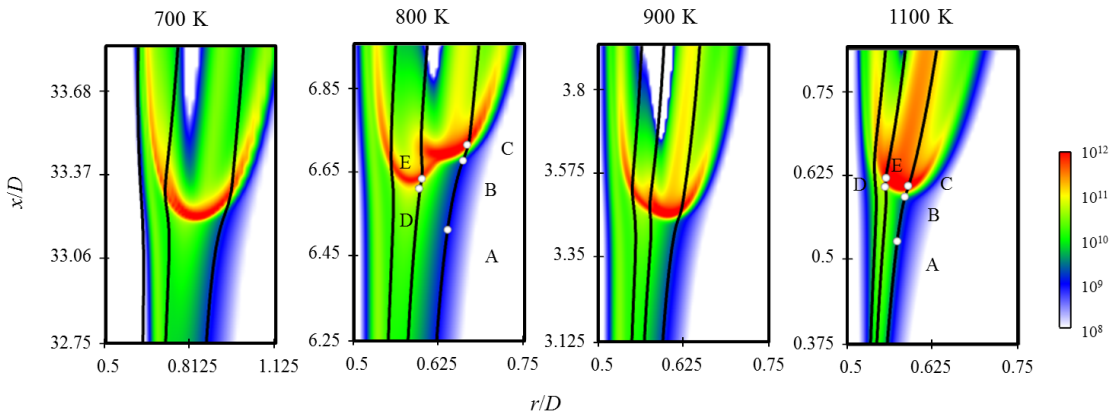


Figure 3.3: Heat release rate [ $\text{J}/\text{m}^3\cdot\text{s}$ ] profiles for the steady cases with the same flow velocities but different boundary temperatures. The iso-contours of  $Z_{\text{st}}$ ,  $Z = 0.2$ , and  $Z = 0.3$  are outlined from right to left in solid lines, respectively. The CEMA sampling points at 800 and 1100 K are indicated along the iso-contours.

on the largest heat release contour (the leading point), colored by red, will be referred to as the stabilization point.

At 700 K, a tribrachial thermal structure is observed, and the stabilization point is located around  $Z = 0.15$ , which is richer than the triple point, where the three branches intersect. Moreover, compared to the classical triple flame structure, the middle heat release rate branch, corresponding to the nonpremixed flame, is significantly weaker than the other two branches.

At 800 K, the stabilization point is not located on the tribrachial structure any more. Instead, it is located near  $Z = 0.23$  and connects two trailing heat release

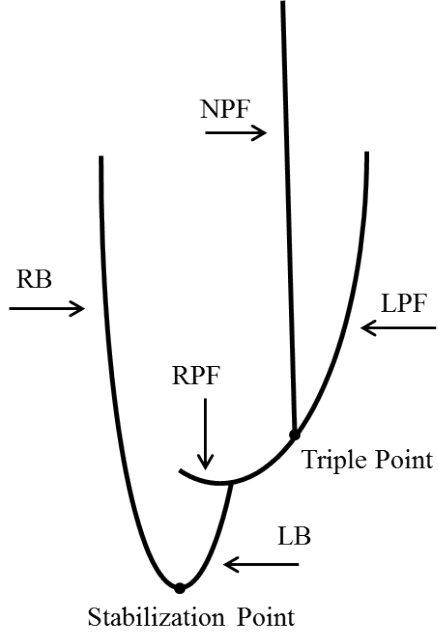


Figure 3.4: A schematic of the thermal structure of the 800 K case. LPF, RPF, and NPF denotes the lean premixed, rich premixed, and nonpremixed flame branches on the tribrachial structure, respectively. LB and RB denotes the leaner and richer branches of the reacting front, respectively.

branches, where a tribrachial flame structure is attached to the leaner branch (LB) of the bibrachial reacting front. A schematic of the structure is shown in Fig. 3.4.

As the air boundary temperature increases to 900 K, the stabilization point shifts back to  $Z = 0.14$ . Moreover, a long trailing branch at richer mixture fraction is attached to the main tribrachial structure, resulting in a tetrabrachial structure. Compared with the structure shown in the 800 K case, the main tribrachial structure stabilizes further upstream, for it depends less on the radical accumulation ahead of the flame. Therefore, it catches up with the reacting front at richer mixture fraction, and they merge into the apparent tetrabrachial structure.

A further increase in the boundary temperature results in a structure that is very similar to the classical triple flame, except for the fact that there is also heat release ahead of the stabilization point at  $Z = 0.13$ . Some of the multibrachial structures were also observed by Krisman *et al.* [80], using different definitions for branches, and

it was concluded that the autoignition chemistry could affect the flame structure and the stabilization mechanism.

To first qualitatively demonstrate the chemical structure of the flame, selected species profiles were examined, shown in Figs. 3.5 to 3.8. The methoxymethylperoxy radical ( $\text{CH}_3\text{OCH}_2\text{O}_2$ ) and hydroxyl radical (OH) were chosen as indicators of low and high-temperature chemistry, respectively. The hydroperoxyl radical ( $\text{HO}_2$ ) and hydrogen peroxide ( $\text{H}_2\text{O}_2$ ) were chosen, for they form in the preheat zone of a flame or before autoignition but quickly vanish in the post flame zone or after ignition [163].

For all four cases, similar profiles can be seen for some species. First, low-temperature chemistry, indicated by the  $\text{CH}_3\text{OCH}_2\text{O}_2$  radical, is found to be important at richer mixture fractions, where the temperature is also lower. Second, the OH radical peaks at and downstream of the maximum heat release locations and correlates well with the tribrachial structure shown in the heat release rate profiles, indicating the presence of high-temperature chemistry. Third, the  $\text{HO}_2$  mass fraction peaks in a thin region. Compared with the heat release rate contours, this thin region outlines the flame front and the reactive mixture at the rich mixture fractions and indicates the importance of the exothermic three-body recombination reaction  $\text{H} + \text{O}_2 + \text{M} \rightleftharpoons \text{HO}_2 + \text{M}$ .

However, there are also differences in the chemical structure among the different cases. For example, for the 800 and 900 K cases, another OH local maxima, which is two orders of magnitudes smaller than the peak value on the tribrachial structure, appears at richer mixture fractions, immediately downstream of where the  $\text{CH}_3\text{OCH}_2\text{O}_2$  radical and  $\text{H}_2\text{O}_2$  disappear, indicating autoignition. Moreover, more pronounced differences between the three lower boundary temperature cases and the 1100 K case are shown in the  $\text{H}_2\text{O}_2$  profiles: for the lower boundary temperature cases,  $\text{H}_2\text{O}_2$  accumulates along the mixture fraction iso-contours until it decomposes in the flame region, while, for the 1100 K case, the  $\text{H}_2\text{O}_2$  accumulation is an order of

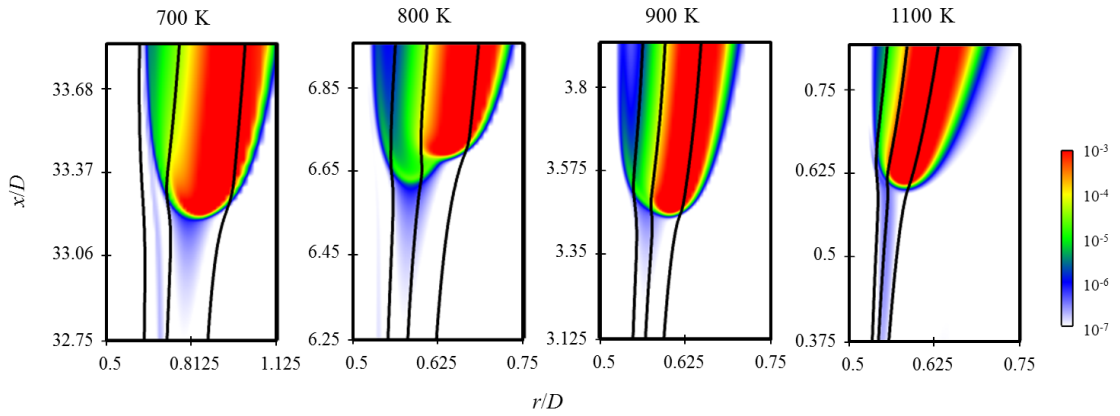


Figure 3.5: Hydroxyl (OH) radical mass fraction profiles for the steady cases with the same flow velocities but different boundary temperatures. The mixture fraction iso-contours are the same as in Fig. 3.3.

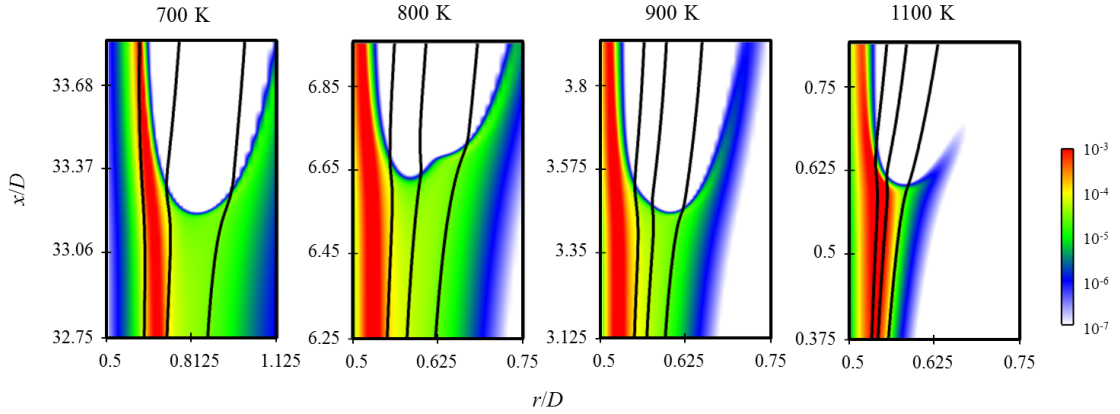


Figure 3.6: Methoxymethylperoxy ( $\text{CH}_3\text{OCH}_2\text{O}_2$ ) radical mass fraction profiles for the steady cases with the same flow velocities but different boundary temperatures. The mixture fraction iso-contours are the same as in Fig. 3.3.

magnitude lower, due to the reduced residence time from the nozzle exit to the flame base.

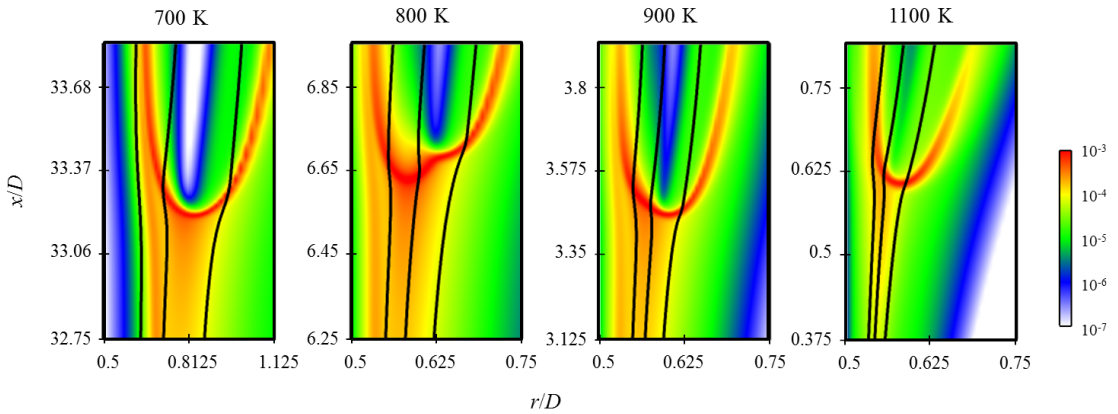


Figure 3.7: Hydroperoxyl ( $\text{HO}_2$ ) radical mass fraction profiles for the steady cases with the same flow velocities but different boundary temperatures. The mixture fraction iso-contours are the same as in Fig. 3.3.

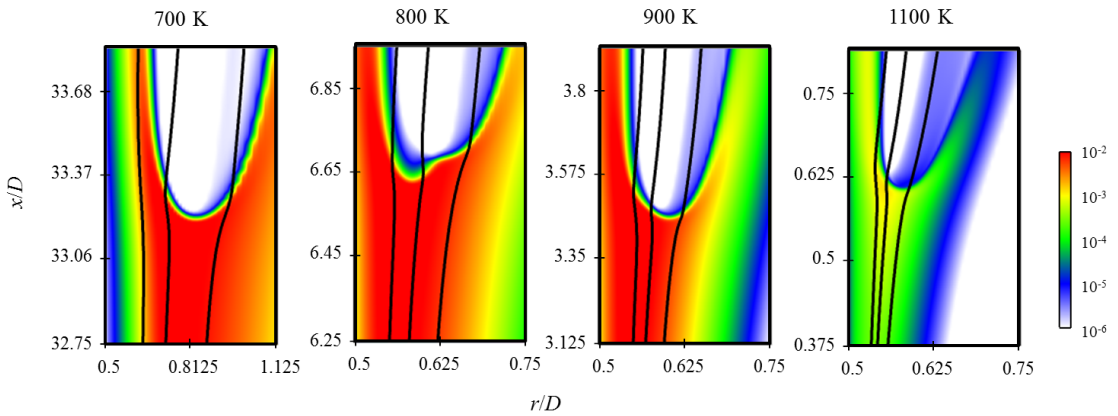


Figure 3.8: Hydrogen peroxide ( $\text{H}_2\text{O}_2$ ) mass fraction profiles for the steady cases with the same flow velocities but different boundary temperatures. The mixture fraction iso-contours are the same as in Fig. 3.3.

### 3.2.2 Computational Diagnostics and Analysis

The above heat release rate and species profiles demonstrate the thermal and chemical structure of the reacting fronts at different boundary temperatures. However, more detailed computational diagnostics and analysis are needed to further demonstrate the controlling chemistry and the stabilization mechanism.

## Chemical Explosive Mode Analysis

In addition to the analysis based on selected species profiles, Chemical Explosive Mode Analysis (CEMA) [94, 139] was conducted to identify the controlling chemistry in these complex reacting flows. Briefly, local species concentrations and temperature are sampled from the two-dimensional computation and input into CEMA to evaluate the eigenvalues of the Jacobian matrix ( $K + 1$  by  $K + 1$ , where  $K$  is the number of species) of the chemical source terms. The eigenmode associated with the eigenvalue  $\lambda_e$ , which has the largest real part among all the eigenvalues, is defined as a chemical explosive mode, if

$$\text{Re}(\lambda_e) > 0, \lambda_e = \mathbf{b}_e \mathbf{J}_\omega \mathbf{a}_e, \quad (3.1)$$

where  $\mathbf{b}_e$  and  $\mathbf{a}_e$  are the left and right eigenvectors, respectively, associated with  $\lambda_e$ , and  $\mathbf{J}_\omega$  is the chemical Jacobian matrix. The existence of the chemical explosive mode indicates the propensity of local mixture autoignition given an isolated, adiabatic, and constant volume environment. Furthermore, the detailed chemical reactions that contribute to the chemical explosive mode can be quantified by the explosion participation index:

$$\text{PI} = \frac{|(\mathbf{b}_e \cdot \mathbf{S}) \otimes \mathbf{R}|}{\text{sum}(|(\mathbf{b}_e \cdot \mathbf{S}) \otimes \mathbf{R}|)}, \quad (3.2)$$

where  $\mathbf{S}$  is the stoichiometric coefficient matrix,  $\mathbf{R}$  is the vector of the net rates for the reactions, and  $\otimes$  denotes elementwise multiplication of two vectors.

The dominant reactions at representative locations, such as those upstream and near the flame base, are identified, based on the explosive mode and participation index. For each case, the local species concentrations and temperature were sampled along the  $Z_{st}$ ,  $Z = 0.2$ , and  $Z = 0.3$  iso-contours, as indicated in Fig. 3.3, and processed by CEMA to demonstrate the evolution of the dominant reactions.

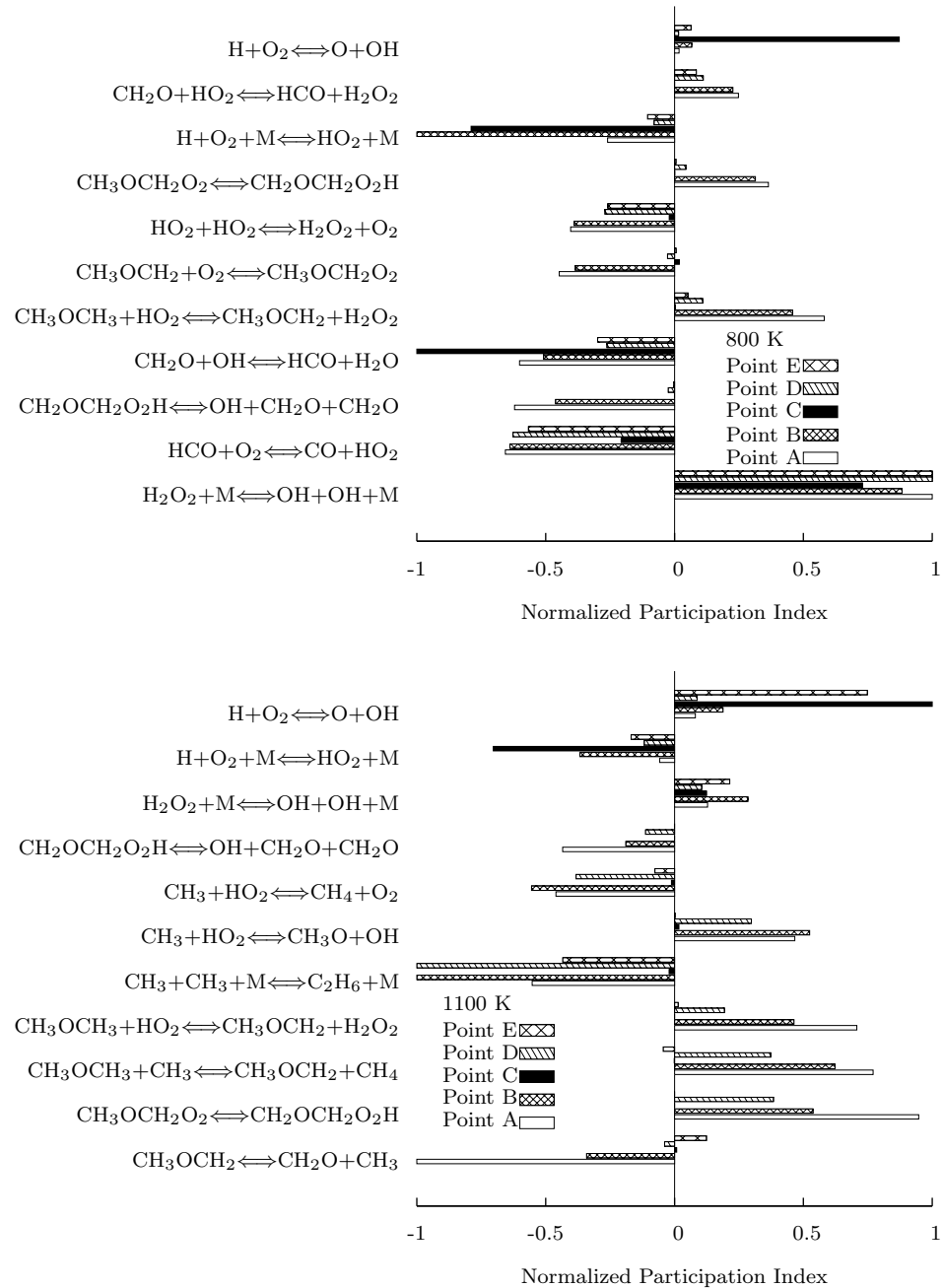


Figure 3.9: Normalized participation index at 800 K and 1100 K. Sampled locations are indicated in Fig. 3.3.

The results are summarized in Fig. 3.9, where three representative locations along the  $Z_{st}$  iso-contour approaching the flame front and two locations ahead of and at the reaction front at  $Z = 0.2$  were sampled. For the three lower coflow temperature cases, similar chemical patterns were found. Upstream of the flame front, the chemical explosive mode is positive, indicating that the mixtures have the potential to explode; downstream of the flame front, the chemical explosive mode becomes negative, meaning that the mixtures are composed of burned products. Following the  $Z_{st}$  iso-contour, the hydrogen peroxide chain branching reaction ( $\text{H}_2\text{O}_2 + \text{M} \rightleftharpoons \text{OH} + \text{OH} + \text{M}$ ) is the reaction that has the largest contribution to the explosive mode, showing the dominant role of autoignition chain branching [156]. The characteristic DME low-temperature chemistry is also important upstream of the flame, where methoxymethylperoxy radical formation ( $\text{CH}_3\text{OCH}_2 + \text{O}_2 \rightleftharpoons \text{CH}_3\text{OCH}_2\text{O}_2$ ) and isomerization ( $\text{CH}_3\text{OCH}_2\text{O}_2 \rightleftharpoons \text{CH}_2\text{OCH}_2\text{O}_2\text{H}$ ) promote the explosion, while the  $\beta$ -scission reaction ( $\text{CH}_2\text{OCH}_2\text{O}_2\text{H} \rightleftharpoons \text{OH} + \text{CH}_2\text{O} + \text{CH}_2\text{O}$ ) retards the explosion. Approaching the flame front, the H radical recombination reaction ( $\text{H} + \text{O}_2 + \text{M} \rightleftharpoons \text{HO}_2 + \text{M}$ ) becomes important for the 700 – 900 K cases, due to the fact that the H radicals generated at the reaction zone diffuse upstream and undergo three-body recombination reactions under the high pressure, low temperature condition. Further downstream where the heat release rate peaks, the hydrogen branching reaction ( $\text{H} + \text{O}_2 \rightleftharpoons \text{O} + \text{OH}$ ) becomes the most important chain branching reaction as it is activated at high temperatures [156].

CEMA conducted along the  $Z = 0.2$  iso-contour, which crosses the rich heat release front in the 800 and 900 K cases, shows different chemical mode evolution. The  $\text{H}_2\text{O}_2$  chain branching reaction is always the dominant reaction that promotes the explosive mode, while the H radical recombination reaction and the H branching reaction are less important ahead of the rich heat release front and at the front.

On the contrary, although low-temperature chemistry is still important for the 1100 K case upstream of the reaction zone and the hydrogen chain branching reaction promotes explosion in the reaction zone, the hydrogen peroxide chain branching reaction is not very important for all the sampled locations. Since the hydrogen peroxide reaction is the crucial chain branching reaction for the autoignition process, it is concluded that the 1100 K case is less affected by autoignition chemistry than the lower boundary temperature cases.

### Lagrangian Flamelet Analysis

The above species profile analysis and CEMA results have demonstrated that autoignition chemistry is crucial to the complex flame structure in the 700 to 900 K cases. However, the role that autoignition plays in the stabilization still needs further investigation. To elucidate the role of autoignition for the current flow configuration, a direct comparison with the homogeneous counterpart for a Lagrangian flow particle is insufficient, for no transport process is considered in homogeneous autoignition. In the current two-dimensional configuration, however, transport processes are present in two directions: parallel and normal to the mixture fraction gradient. These transport processes might be important: first, the temperature and species stratification parallel to the mixture fraction gradient can significantly modify the ignition characteristics, especially for fuels with NTC chemistry, as shown in Chapter 2. Second, flame propagation normal to the mixture fraction gradient can also influence the autoignition front through thermal and radical back diffusion.

To demonstrate the dominant transport direction as well as the stabilization mechanism, one-dimensional unsteady flamelet analysis was conducted to account for unsteadiness (convection), chemical reactions, and diffusion parallel to the mixture fraction gradient, while neglecting the transport process in the normal direction. As a consequence, the unsteady flamelet is able to capture inhomogeneous autoigni-

tion, with diffusion allowed only in one direction. Following the mixture fraction iso-contour, the spatial information from the two-dimensional computation could be interpreted as the time history of the corresponding mixture in the Lagrangian frame. If the one-dimensional unsteady flamelet predicts this time history, only the transport processes parallel to the mixture fraction gradient are important, and, therefore, the thermal structure is stabilized by inhomogeneous autoignition. Conversely, if the unsteady flamelet solutions do not agree with the two-dimensional computations, the transport processes along the mixture fraction iso-contour are not negligible compared to the gradient direction. Therefore, premixed flame propagation is the dominant stabilization mechanism, or, at least, stabilization is strongly affected by flame back diffusion.

The unsteady flamelet model developed by Pitsch *et al.* [122], referred to as Lagrangian Flamelet Analysis (LFA), was adopted. Due to the mixing processes, the scalar dissipation rate  $\chi$ , which can influence the flamelet solution significantly, decreases in the streamwise direction. Therefore, this dissipation rate variation must be considered when computing a flamelet as it evolves downstream.

The unsteady flamelet was computed with FlameMaster [121], and the dissipation rate was specified as a function of the flamelet time. The flamelet time was computed from the two-dimensional computational results, along the stoichiometric mixture fraction  $Z_{\text{st}}$  iso-contour:

$$t = \int_0^x \frac{1}{(u + u_Z)(x')|(Z = Z_{\text{st}})} dx'. \quad (3.3)$$

This formulation is otherwise the same as that of Pitsch *et al.* [122], except that, in addition to the axial component of fluid convection velocity  $u$ , the axial component of the mixture fraction iso-contour propagation speed relative to the fluid convection  $u_Z$  is also taken into account. The expression for the constant property scalar iso-surface

velocity relative to the local fluid motion was derived by Pope [126], and the current work adopts the formulation derived by Lignell *et al.* [86] for variable properties:

$$\mathbf{u}_Z = -\frac{\nabla \cdot (\rho D_Z \nabla Z)}{\rho |\nabla Z|} \mathbf{n}, \quad (3.4)$$

where  $D_Z$  is the mixture fraction diffusivity, which is defined in Sec. 3.1, and  $\rho$  the density. The normal vector  $\mathbf{n}$ , defined as

$$\mathbf{n} = \frac{\nabla Z}{|\nabla Z|}, \quad (3.5)$$

indicates the direction of this diffusion induced relative velocity. The dissipation rate along the  $Z_{st} = 0.1005$  iso-contour obtained from the two-dimensional computation was then correlated with this flamelet time and provided as the input for the LFA calculation. The dissipation rates at other mixture fractions were computed assuming the following form [119]:

$$\chi(Z) = \chi(Z_{st}) \frac{\exp(-2[\text{erfc}^{-1}(2Z)]^2)}{\exp(-2[\text{erfc}^{-1}(2Z_{st})]^2)} = \chi(Z_{st}) f(Z; Z_{st}). \quad (3.6)$$

To validate this formulation in the current configuration, the dissipation rates along different mixture fraction iso-contours were sampled from the two-dimensional computations, normalized using Eq. 3.6, and compared with the sampling along the  $Z_{st}$  iso-contour. As shown in Fig. 3.10, the normalized dissipation rates at different mixture fractions all collapse to the value at  $Z_{st}$ . Therefore, only the dissipation rate samplings along the  $Z_{st}$  iso-contour were needed to perform the unsteady flamelet calculation.

To account for the differential diffusion, species Lewis numbers for LFA were specified the same as in the two-dimensional computations. The governing equations for species and temperature follow Eq. 24 and 25 in Pitsch and Peters [123].

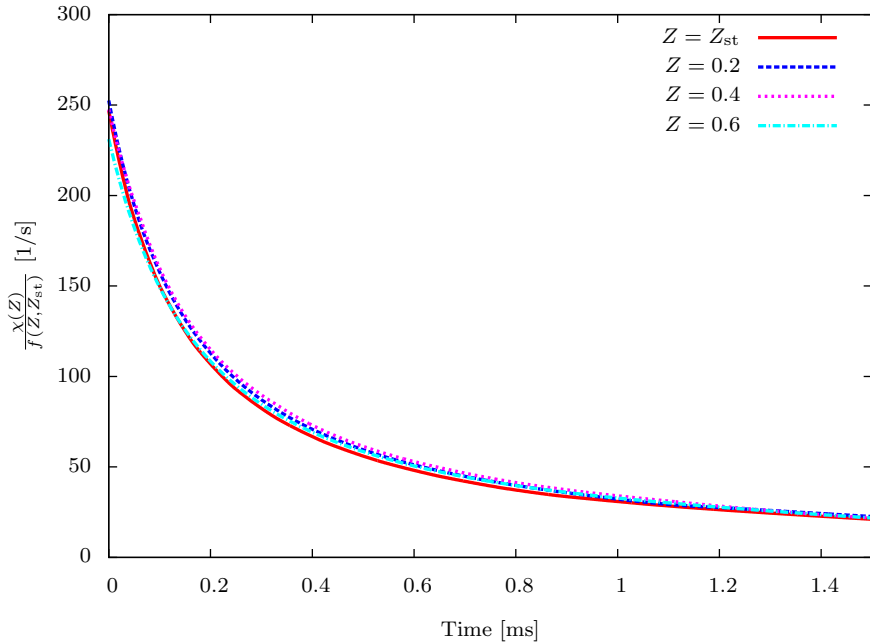


Figure 3.10:  $\frac{\chi(Z)}{f(Z; Z_{st})}$ , using Eq. 3.6, from the two-dimensional calculations at 800 K.

The time history of the dissipation rate  $\chi_{st}$  was specified in LFA according to the two-dimensional computation. To avoid the ill-defined Lagrangian time in the recirculation zone, time zero was defined at a downstream location ten times the thickness of the wall. Accordingly, the species and temperature profiles along the radial cut at this location were specified as the initial conditions for the flamelet. Based on these initial conditions and  $\chi_{st}$  time history profiles, the unsteady flamelets were calculated and compared with the two-dimensional computational results for  $Z_{st}$ ,  $Z = 0.2$ , and  $Z = 0.3$ .

As shown in Fig. 3.11, two ignition stages can be seen at  $Z_{st}$  and  $Z = 0.2$  for the 700 K case, while at  $Z = 0.3$  only one ignition dominated by low-temperature chemistry is observed, due to the reduced initial temperature. At all three mixture fractions examined, the flamelets agree with the two-dimensional computations very well. For the 800 K case, both the flamelet and two-dimensional computation experience almost identical time histories, where two-stage ignition occurs at all three mixture fractions.

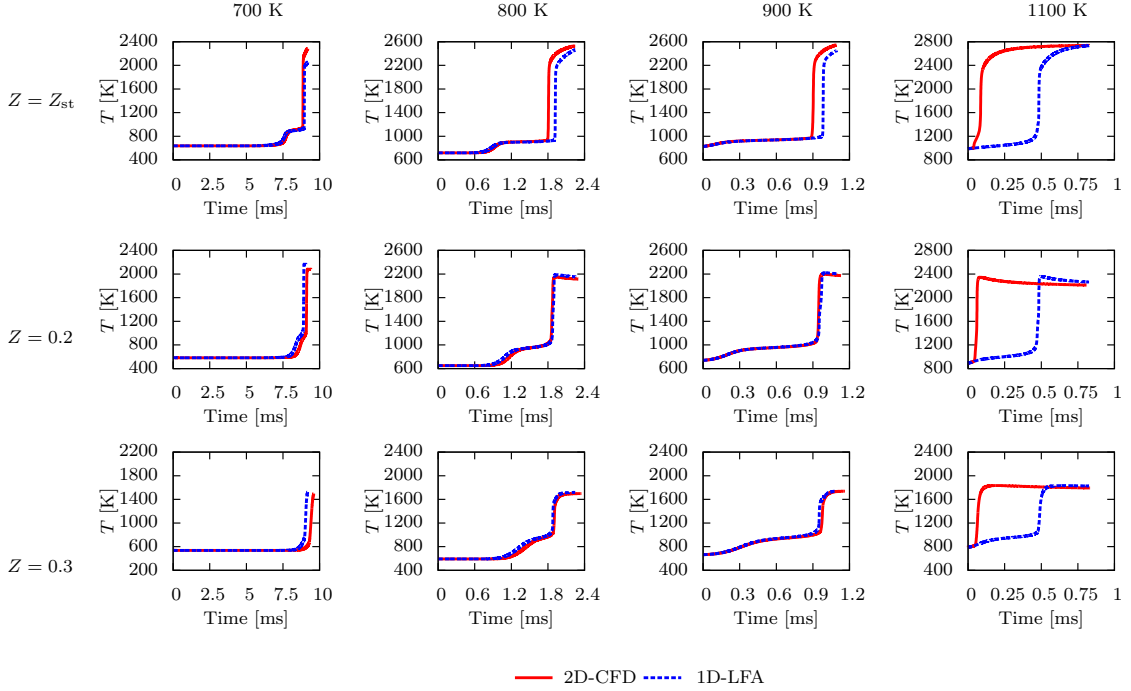


Figure 3.11: Comparison between 2D-CFD and 1D-LFA results for the steady cases with the same flow velocities but different boundary temperatures.

As the initial temperature further increases, corresponding to the increase in the boundary temperatures in the CFD computation, the two-stage ignition phenomenon is less pronounced. However, the 900 K case still shows good agreement between the flamelet profile with the time history of the two-dimensional computation at  $Z = 0.2$  and 0.3, while LFA slightly lags behind the CFD computation at  $Z_{st}$ , similar to the 800 K case.

On the contrary, for the 1100 K case, the ignition delay time computed with the one-dimensional flamelet assumption is significantly longer than the two-dimensional counterpart, indicating that transport processes along the mixture fraction iso-contours must be important and that autoignition is less important to the stabilization mechanism.

### 3.2.3 Stabilization Mechanism

With the above analysis based on species profiles, Chemical Explosive Mode Analysis, and Lagrangian Flamelet Analysis, the transition of the stabilization mechanism and the coupling between autoignition chemistry and flame propagation can be clearly identified. Two fundamental stabilization mechanisms are relevant: the *kinetic* stabilization mechanism, due to the balance between the autoignition delay time and flow residence time, and the *kinematic* stabilization mechanism, due to the balance between the local premixed flame propagation velocity and the local flow velocity.

In this stratified composition and temperature field, autoignition and flame propagation are coupled through thermal and radical interactions, for the accumulation of the upstream radicals and heat release from autoignition accelerate the flame propagation velocity. The flame also transfers heat and radicals through back diffusion processes to the upstream, which could also facilitate autoignition.

The stabilization mechanism was determined by comparing the two-dimensional computations with the one-dimensional inhomogeneous autoignition predicted by LFA. When these two time history profiles agree well, the case is characterized as *kinetically* stabilized. Specifically, at 700 K, the one-dimensional LFA agrees very well with the two-dimensional computation at all of the mixture fractions examined. Therefore, the 700 K case is characterized as *kinetically* stabilized. As the boundary temperature increases, the influences from premixed flame propagation become important, as predictions by LFA lag behind the CFD results for some mixture fractions. At 800 K, an autoignition front stabilizes the multibrachial structure at rich mixture fractions, due to the shorter ignition delay time resulting from the NTC chemistry, and a modified triple flame structure stabilizes slightly downstream of this front at leaner mixture fractions, as shown in Fig. 3.3. Further increasing the boundary temperature results in higher flame propagation velocities. Therefore, the flame front at leaner mixture fraction depends less on radical accumulation ahead

of the flame and propagates upstream, and the stabilization is influenced by both inhomogeneous autoignition and premixed flame propagation. The transition to a *kinematically* stabilized flame structure is achieved for the 1100 K case, where the local flame propagation velocity balances the incoming flow velocity. Therefore, the flame structure stabilizes close to the nozzle exit and depends least on radical accumulation from upstream. Consequently, the one-dimensional LFA predictions depart from the two-dimensional computation significantly.

Based on the understanding obtained from the current study, further extension of the stabilization regime can be made, as shown in Fig. 3.12. For fixed inlet flow velocity, when the boundary temperature is sufficiently low, the mixture cannot be autoignited, and it is essentially a frozen flow. Even when an external ignition source is applied, the flame cannot keep up with the excessive high flow velocity, such that the flame blows out. When the boundary temperature is high enough to activate autoignition, it occurs far downstream, but the flame propagation velocity still cannot keep up with the flow velocity. As a consequence, a pure *kinetically* stabilized autoignition front can be achieved, which is similar to the 700 K case. Conversely, when the boundary temperature is sufficiently high, the flame stabilizes close to the inlet, where the upstream can be treated as frozen, due to reduced residence time, which is similar to the 1100 K case. Therefore, a *kinematically* stabilized classical triple flame structure is achieved. Further increase in the boundary temperature results in an attached flame with the increased flame speed. Although not included, an attached flame was computed at 1500 K. In between the *kinetically* and *kinematically* stabilized regimes, there is a transitional regime governed by both mechanisms, which corresponds to the 800 and 900 K cases. Due to the NTC behavior of the autoignition chemistry, the stabilization point, in terms of mixture fraction space, varies, and the complex multibrachial flame structure appears.

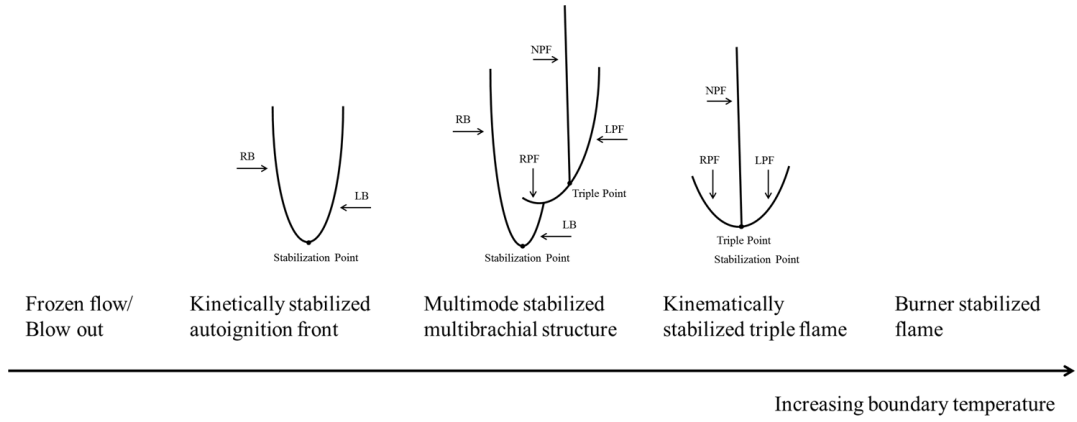


Figure 3.12: Extended regimes of the stabilization mechanism as the coflow boundary temperature increases.

Table 3.2: Computational domain and number of grid points for steady cases with the same boundary temperature but different flow velocities.

Inlet Velocity [m/s]	2.4	3.2	8.0
$L_x$ [mm]	3.5	3.5	15
$N_x$	1536	1536	3072
$N_r$	176	176	176

### 3.3 Flame Stabilization: Boundary Velocity Effects

In this section, the effect of boundary velocity and hence transport on flame stabilization is investigated. Therefore, in all cases studied in this section, the temperature of the heated air coflow is fixed at 900 K. Conversely, the boundary velocities of the DME jet as well as the coflow air are varied (2.4, 3.2, and 8.0 m/s). The dimensions of and number of grid points in the computational domain for each computation are summarized in Table 3.2. The 3.2 m/s case has been presented in Sec. 3.2.

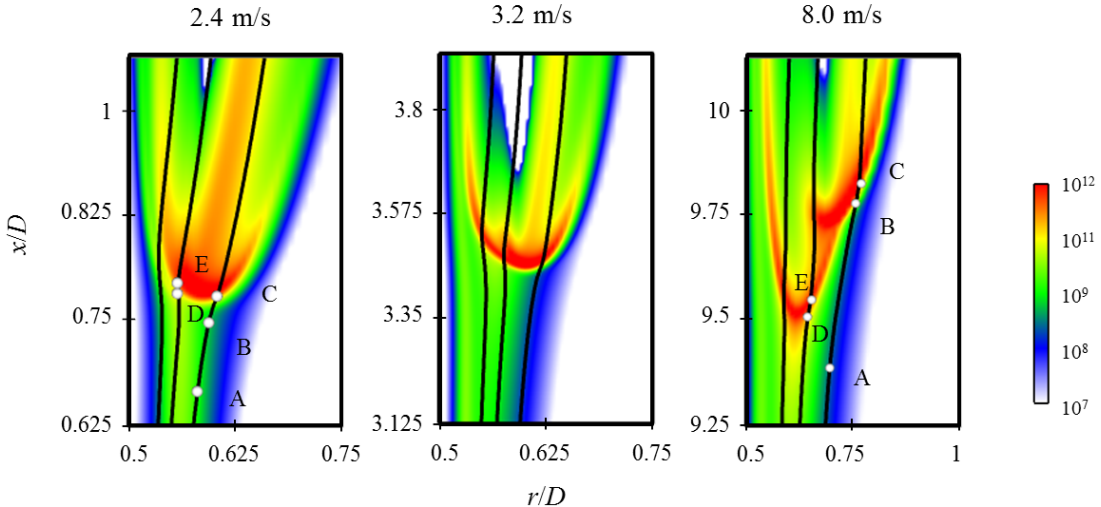


Figure 3.13: Heat release rate [ $\text{J}/\text{m}^3\text{-s}$ ] profiles for steady cases with the same boundary temperature but different flow velocities. The iso-contours of  $Z_{\text{st}}$ ,  $Z = 0.2$ , and  $Z = 0.3$  are outlined from right to left in solid lines, respectively. The CEMA sampling points for 2.4 and 8.0 m/s cases are marked along the iso-contours.

### 3.3.1 Thermal and Chemical Structure

The heat release rate profiles for the three cases are shown in Fig. 3.13. A qualitative determination of the stabilization point is the most upstream point on the largest heat release contour (the leading point), colored by red. The mixture fraction iso-contours of  $Z_{\text{st}} = 0.1005$ ,  $Z = 0.2$ , and  $Z = 0.3$  are delineated in solid black lines, from right to left.

When the inlet velocity is the lowest, 2.4 m/s, a tribrachial thermal structure is observed very similar to that of the classical triple flame. The triple point at  $Z = 0.15$ , where the three large heat release branches intersect, is also the stabilization point. Some heat release can be found upstream of the tribrachial thermal structure for the partially reacting mixture at elevated temperature but is much less than the heat release from the flame structure. As the inlet velocity increases to 3.2 m/s, another branch with large heat release is found attached to the tribrachial structure around  $Z = 0.2$ . The stabilization point is, again, the same as the triple point. This structure

has been analyzed in Sec. 3.2. However, as the inlet velocity further increases to 8.0 m/s, the stabilization point is no longer on the tribrachial structure. Instead, it is found to be near  $Z = 0.25$  and is the intersection point of two trailing heat release branches. Attached to the leaner branch, there is a tribrachial structure that appears similar to the triple flame structure. This multibrachial structure is similar to the one discussed in Sec. 3.2 at a lower oxidizer temperature (800 K) and lower velocity (3.2 m/s).

Similar to Sec. 3.2.2, the controlling chemistry of the three cases was studied with CEMA. Samplings were conducted along  $Z_{st}$ ,  $Z = 0.2$ , and  $Z = 0.3$  iso-contours, as shown in Fig. 3.13. Based on the explosive mode and participation index, the evolution of the dominant reactions is shown in Fig. 3.14.

At 2.4 m/s, the dominant reactions along  $Z_{st}$  and  $Z = 0.2$  iso-contours evolve in similar ways: upstream of the tribrachial structure (points A, B, and D), low-temperature chemistry, characterized by reactions involving  $\text{CH}_3\text{OCH}_2\text{O}_2$  radicals, is active. Due to the high diffusivity of H radicals and the elevated pressure, the H radical recombination reaction ( $\text{H} + \text{O}_2 + \text{M} \rightleftharpoons \text{HO}_2 + \text{M}$ ) is important. At the most reactive region (points C and E), the H radical branching reaction ( $\text{H} + \text{O}_2 \rightleftharpoons \text{O} + \text{OH}$ ) becomes the most important chain branching reaction, indicating the transition to high-temperature chemistry. On the contrary, for the 8.0 m/s case, while low-temperature chemistry is still active upstream of the multibrachial structure, the dominant chain branching reaction is the hydrogen peroxide branching reaction ( $\text{H}_2\text{O}_2 + \text{M} \rightleftharpoons \text{OH} + \text{OH} + \text{M}$ ). Moreover, the dominant reactions along the  $Z_{st}$  and  $Z = 0.2$  iso-contours evolve in different ways. Along the  $Z = 0.2$  iso-contour, from point D to E, the hydrogen peroxide branching reaction is always the dominant reaction, indicating the role of low-to-intermediate temperature autoignition chemistry [156]. Although this is the case at point A on the  $Z_{st}$  iso-contour, the H radical chain branching reaction becomes dominant at point C, the most reactive zone, indicating

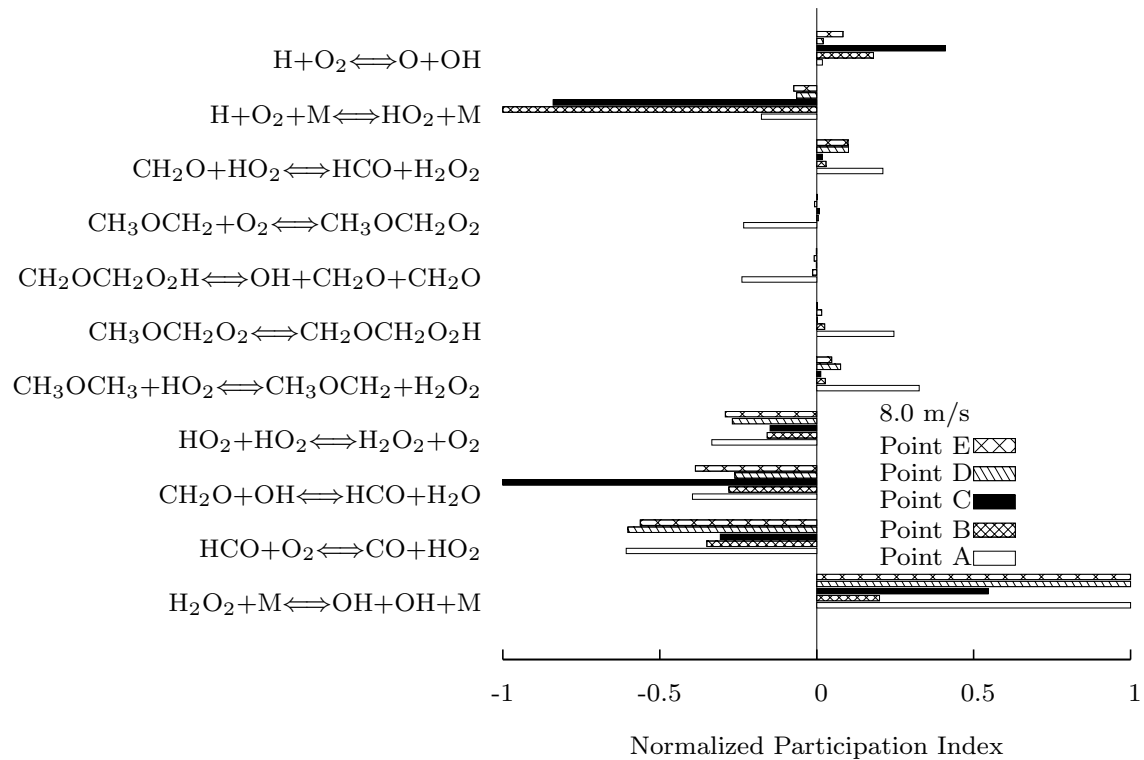
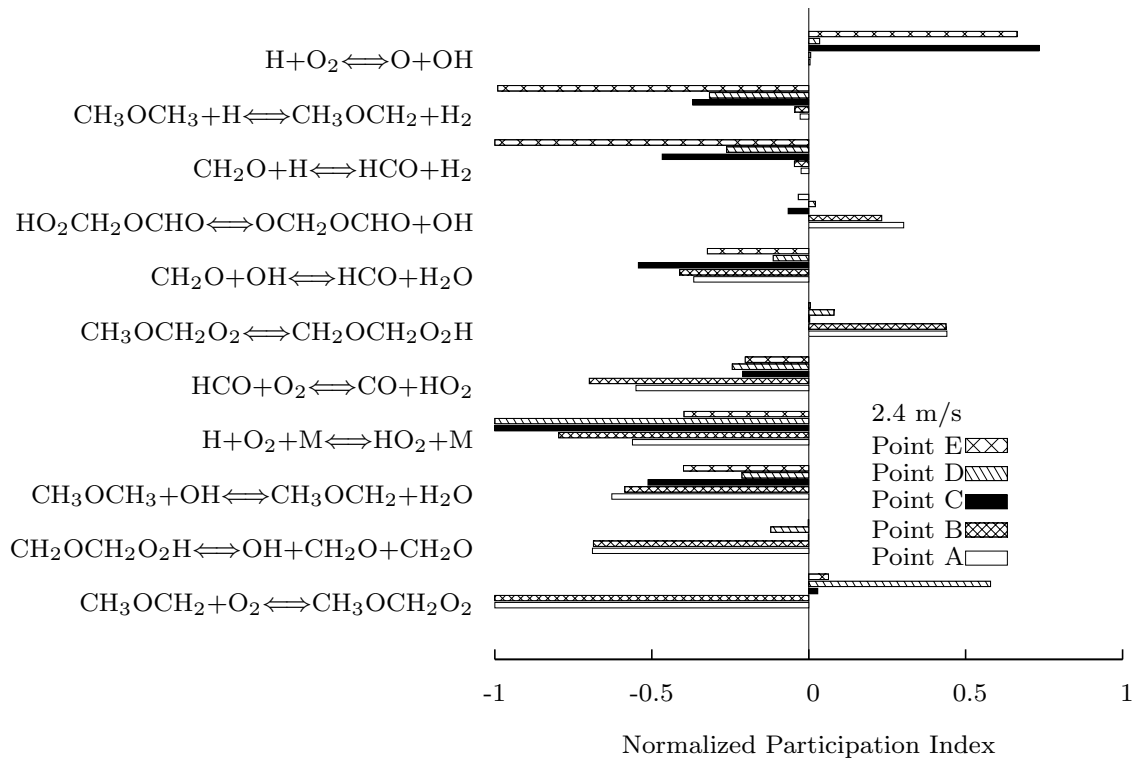


Figure 3.14: Normalized participation index at 2.4 and 8.0 m/s. Sampled locations are delineated in Fig. 3.13.

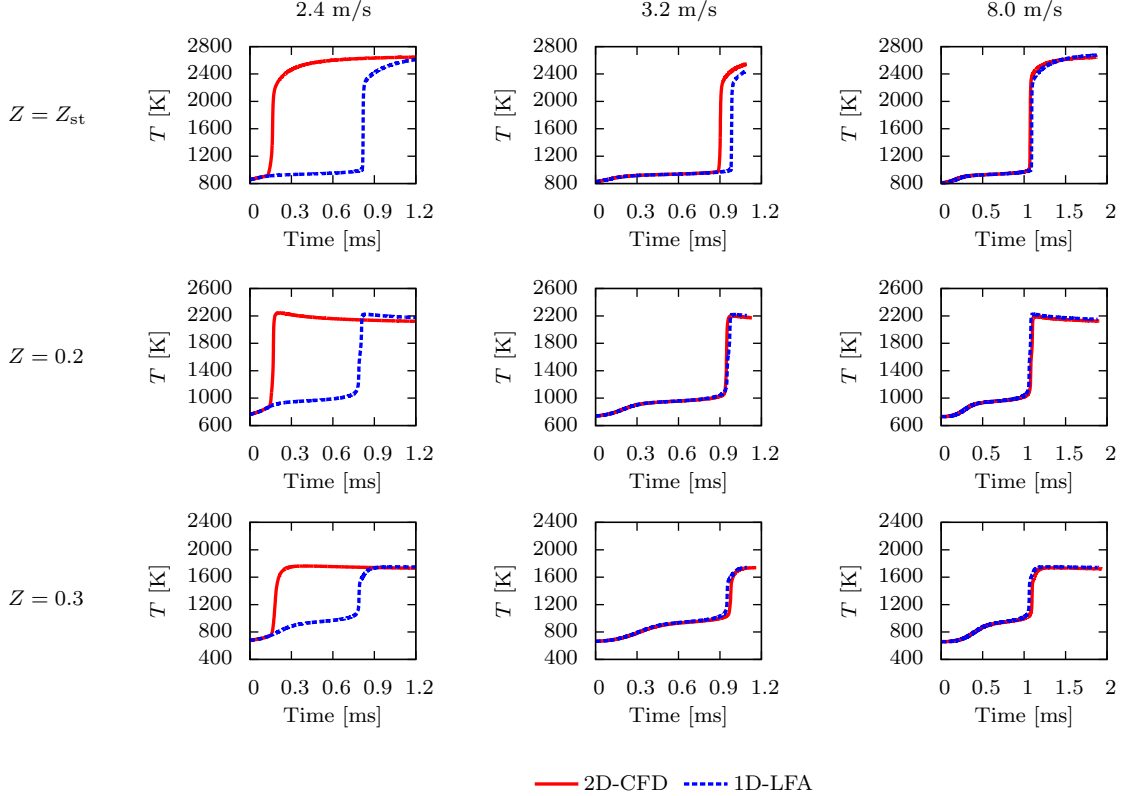


Figure 3.15: Comparison between 2D-CFD and 1D-LFA results for the steady cases with the same boundary temperature but different flow velocities.

that the dominant chemical pathway shifts to high-temperature chemistry. CEMA results for the 3.2 m/s case show similar transitions as those of the 8.0 m/s case, although their thermal structures appear different. Therefore, further computational diagnostics is needed to identify the dominant combustion mode.

### 3.3.2 Stabilization Mechanism

Similar to the Lagrangian analysis presented in Sec. 3.2.2, the Lagrangian time history profiles of the two-dimensional computation and one-dimensional LFA are shown in Fig. 3.15. For each inlet velocity case, the temperature profiles are compared along  $Z_{\text{st}}$ ,  $Z = 0.2$ , and  $Z = 0.3$ .

For the 2.4 m/s case, LFA fails to match the two-dimensional result at all three mixture fractions, indicating that transport processes normal to the mixture fraction

gradient are crucial, which further indicates that flame propagation is the dominant stabilization mechanism. At 3.2 m/s, LFA slightly lags behind the two-dimensional result at  $Z_{st}$  but matches well at  $Z = 0.2$  and  $Z = 0.3$ . Recalling the heat release profile in Fig. 3.13, these results indicate that the tetrabrachial structure consists of a tribrachial structure, at which flame propagation is not negligible, and the richer branch that intersects with the tribrachial flame is an autoignition front, whose response is well captured with the one-dimensional flamelet model. As a result, stabilization of the 3.2 m/s case is characterized as a mixed mode of inhomogeneous autoignition and premixed flame propagation, depending on the local mixture fraction. At 8.0 m/s, LFA agrees well with the two-dimensional result at all mixture fractions, indicating that the transport processes normal to the mixture fraction gradient are negligible. Therefore, the stabilization mechanism is characterized as inhomogeneous autoignition.

### 3.3.3 Autoignition and Flame Interaction

As shown by LFA, under some conditions, inhomogeneous autoignition and premixed flame propagation both contribute to flame stabilization, resulting in a multimode stabilized regime. Furthermore, the interaction between autoignition and flame propagation is tightly coupled. If the thermal structure is mainly *kinetically* stabilized, heat and radicals generated by autoignition will modify the downstream thermal and chemical environment and thus the local flame speed. On the contrary, if stabilization is mainly *kinematic* in nature then heat and radicals generated by the flame can back diffuse upstream, modifying the reactivity upstream.

To demonstrate these complex interactions and understand the transition between *kinetic* and *kinematic* stabilization mechanisms, the LFA results for the 2.4 m/s case were further analyzed. As shown in Fig. 3.15, if there was a *kinetically* stabilized inhomogeneous autoignition front, this front would stabilize further downstream than

the *kinematically* stabilized flame front. Although not shown, CEMA of these LFA solutions show the same evolution of the controlling chemistry as the 8.0 m/s case. In particular, the low-to-intermediate temperature hydrogen peroxide chain branching reaction dominates the transition to autoignition. Therefore, the nature and the qualitative structures of the inhomogeneous autoignition fronts, as predicted by LFA in Fig. 3.15 for the two lower inlet velocity cases, are essentially the same as the 8.0 m/s case.

A general description of the initiation of these multibrachial inhomogeneous autoignition fronts in all three cases is that, due to radical accumulation and heat release, the controlling chemistry shifts from low-temperature chemistry, represented by  $\text{CH}_3\text{OCH}_2\text{O}_2$  reactions, to hydrogen peroxide branching reactions. At some mixture fractions, higher temperatures and more oxidizer supply enable the dominant chemistry to transition further to high-temperature chemistry, as characterized by the H radical branching reaction. As shown in Fig. 3.16, there are double or triple heat release peaks, depending on the mixture fraction. However, for all mixture fractions, these peaks correlate very well with the inflection points on the temperature profiles and peaks on the OH radical profiles. Comparing them with the  $\text{CH}_3\text{OCH}_2\text{O}_2$  radical profile, it is clear that low-temperature chemistry results in the first peak of heat release profile and produces OH radicals. Hydrogen peroxide accumulates until it decomposes at the second heat release peak and produces OH radicals through  $\text{H}_2\text{O}_2 + \text{M} \rightleftharpoons \text{OH} + \text{OH} + \text{M}$ . At  $Z_{\text{st}}$  and  $Z = 0.2$ , there is a third heat release and OH radical peak, which is due to the  $\text{H} + \text{O}_2 \rightleftharpoons \text{O} + \text{OH}$  reaction. At  $Z_{\text{st}}$ , the second and third peaks appear to be much closer compared with those at  $Z = 0.2$ , probably due to higher temperature and more abundant oxidizer, such that the H radical chain branching reaction is activated earlier. Due to the lack of oxidizer, the third peak is not observed at  $Z = 0.3$ .

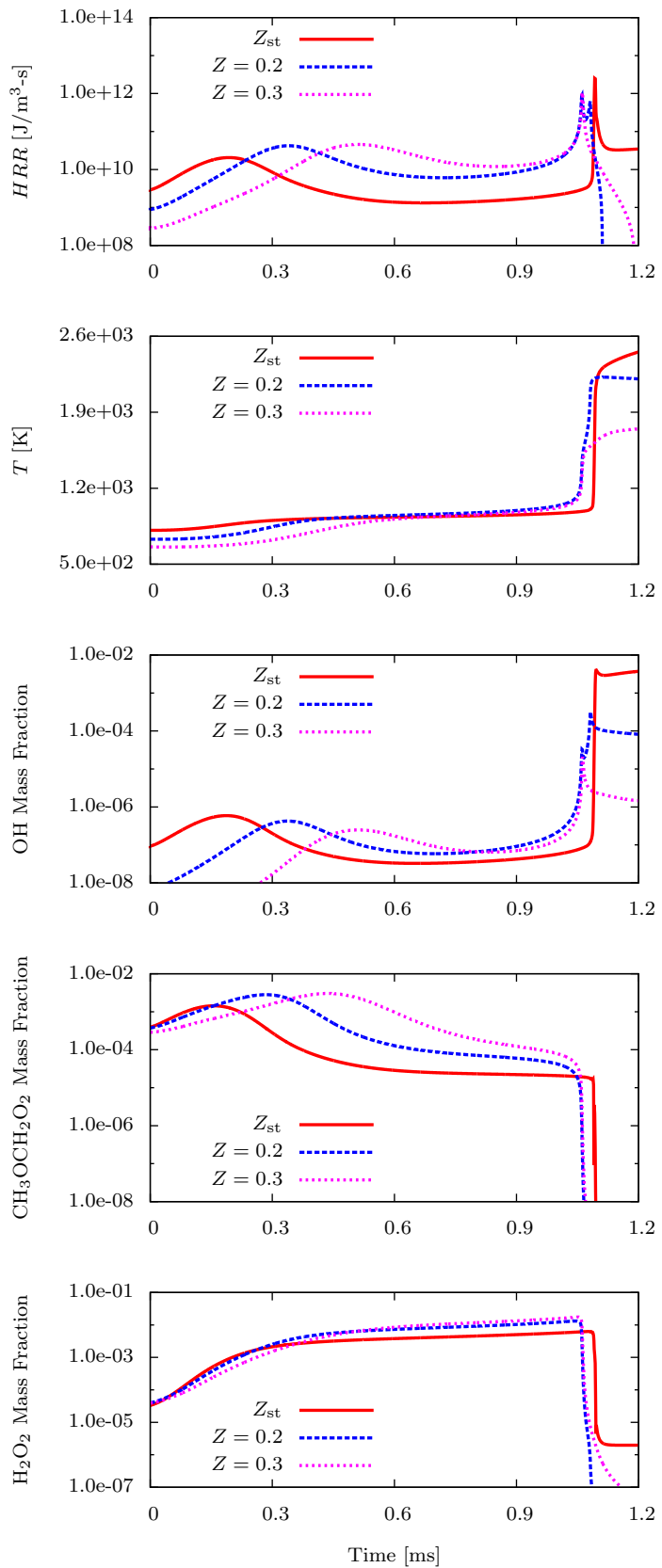


Figure 3.16: LFA profiles along  $Z_{st}$ ,  $Z = 0.2$ , and  $Z = 0.3$  of the 8.0 m/s case.

The multibrachial structure of the inhomogeneous autoignition front is due to the variation in ignition delay time at different mixture fractions. As shown in Fig. 3.13, the stabilization point is determined based on the threshold value of heat release rate. Therefore, the ignition delay time of inhomogeneous autoignition can be determined accordingly, which corresponds to the heat release rate peak that exceeds  $10^{12}$  J/m<sup>3</sup>-s. For the 8.0 m/s case shown in Fig. 3.17, the mixture is autoignited first at  $Z = 0.24$ , which corresponds to the stabilization point in Fig. 3.13. Although the first stage ignition delay time, defined by the first heat release peak through low-temperature chemistry, increases monotonically as mixture fraction increases (temperature decreases), the overall ignition delay time reaches the shortest at  $Z = 0.24$  due to the compensation of larger heat release after the first ignition stage [82], as shown in Fig. 3.16. As a consequence, although low-temperature chemistry is not the dominant chemical pathway at the stabilization point for the *kinetically* stabilized case, it still influences the location of the stabilization point through the mixture fraction dependent heat and radical accumulation upstream.

However, although the cases discussed are all initiated by inhomogeneous autoignition, the stabilization of the final structure depends on the dominant transport processes, which are influenced by the inlet velocities. At 8.0 m/s, heat and radical back diffusion from the autoignition front to upstream is not able to keep up with convection; therefore, the reacting front is *kinetically* stabilized. At 3.2 m/s, as flow convection is weaker, diffusion processes become inherently important and couple with chemical reactions to induce a flame front propagating upstream. However, the propagation speed of the flame varies with composition and temperature. As a consequence, around  $Z_{st}$ , where higher temperature and near-stoichiometric mixture composition enable higher local flame speed, the propagation of the reacting front balances the incoming flow velocity. However, such a balance fails at richer mixture fractions where *kinetic* stabilization dominates due to enhanced NTC-affected au-

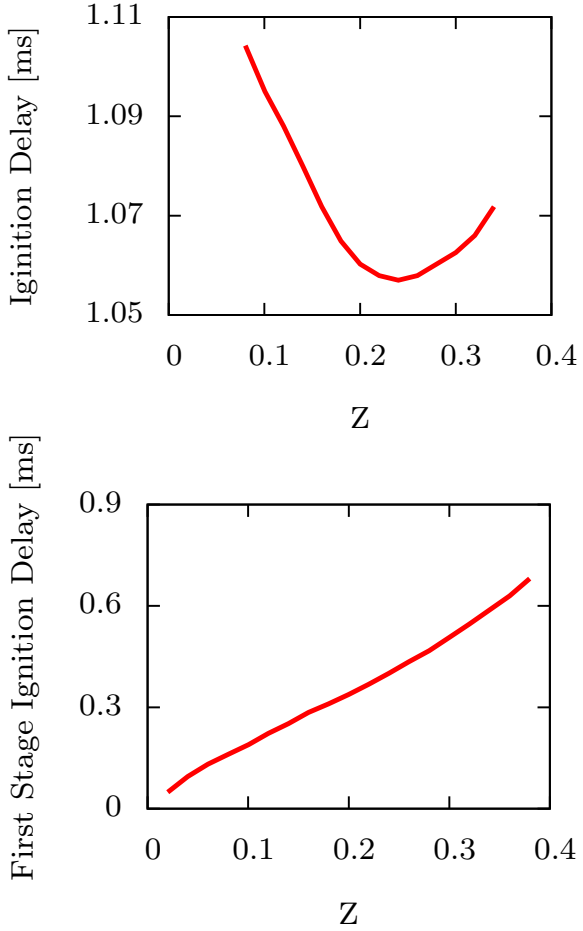


Figure 3.17: LFA results on the mixture fraction dependent total and first stage ignition delay times of the 8.0 m/s case.

to ignition at richer mixture fractions as demonstrated in Fig. 3.17. At 2.4 m/s, back diffusion is important at all mixture fractions such that the reacting front propagates upstream at the local flame speed, as determined by the local composition and temperature. Due to the increased temperature and species stratification and the reduced thermal and radical accumulation from autoignition, the propagation speed of this reacting front is less influenced by inhomogeneous autoignition, as demonstrated with CEMA and LFA. The structure of this *kinematically* stabilized reacting front, which is generally tribrachial, is therefore determined by the variation of the local flame speed.

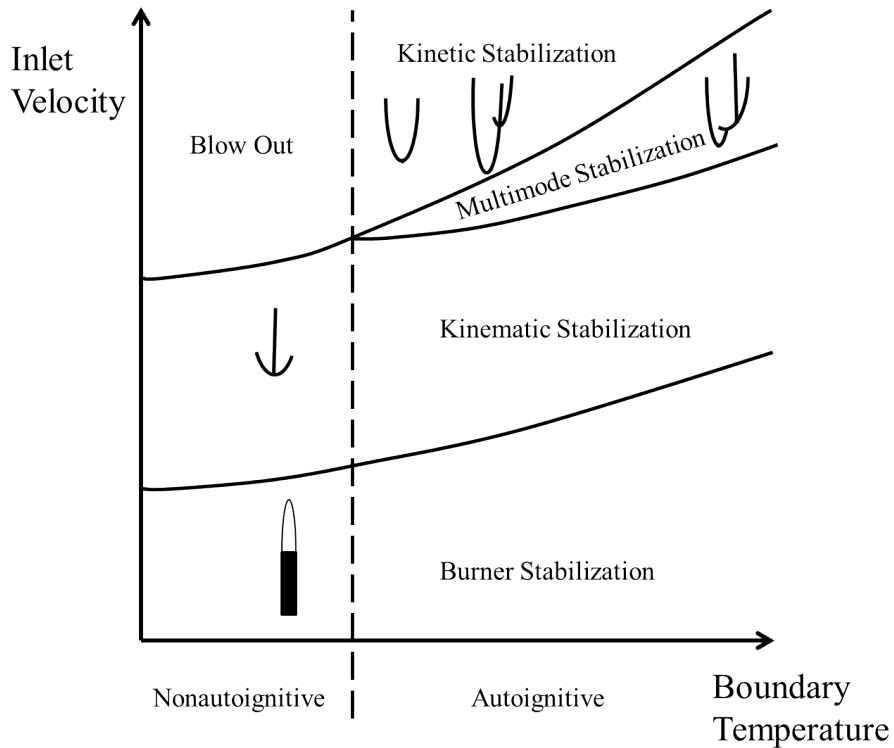


Figure 3.18: A qualitative regime diagram for the stabilization mechanisms as the boundary temperature and inlet velocity vary.

### 3.3.4 Stabilization Regime Diagram

The above sections have demonstrated the transport effects on the thermal and chemical structure of the lifted coflow flames as well as the stabilization mechanisms. Combining these results with the chemical effects demonstrated by changing the coflow boundary temperature in Sec. 3.2, a two-dimensional stabilization regime diagram is proposed, as shown in Fig. 3.18.

Qualitatively, when the boundary temperature is not high enough to activate autoignition, the lifted flame appears as the classical triple flame and is *kinematically* stabilized. When the inlet velocity is below or above certain threshold values, the triple flame becomes attached to the burner or is blown out, respectively.

As the boundary temperature is elevated enough to activate autoignition, increasing the inlet velocity while keeping constant boundary temperature, the flame

stabilization mechanism transits from burner stabilization to a *kinematic* balance between flame speed and incoming flow velocity, then to multimode stabilization influenced by both flame propagation and inhomogeneous autoignition, and finally to *kinetic* stabilization governed by inhomogeneous autoignition. It is expected that the crossover velocities between regimes increase with increasing boundary temperature because flame speed generally increases at higher temperature. However, it is difficult to quantify these boundaries as local composition and temperature vary in the streamwise direction, and, therefore, the reference flame speed cannot be calculated based on the upstream boundary conditions. Furthermore, local flame front curvature, cross-stream species stratification, and flow divergence approaching the flame front also modify the flame speed. As a consequence, only a qualitative trend is demonstrated in Fig. 3.18.

Similarly, if the boundary temperature increases at fixed inlet velocity, transition from blow out to burner stabilized regimes is achieved by moving horizontally across the regime diagram, which was discussed in Sec. 3.2.

### 3.4 Flame Dynamics in Oscillating Flows

In this section, unsteady nonpremixed DME/air coflow flames under autoignitive conditions are computationally studied to elucidate the coupling between unsteady fluid dynamics and chemical kinetics. Various oscillation frequencies were imposed on the inlet velocity, with the maximum and minimum velocities maintained the same as those in Sec. 3.3, which correspond to an autoignition front and a tribrachial flame, respectively. Low frequency oscillation ranging from 25 to 100 Hz, which covers buoyancy-driven instability frequencies [103, 37] and acoustic-driven oscillation frequencies in gas turbines [146] is considered. As the steady cases correspond to different combustion modes, it is expected that, at certain frequencies of veloc-

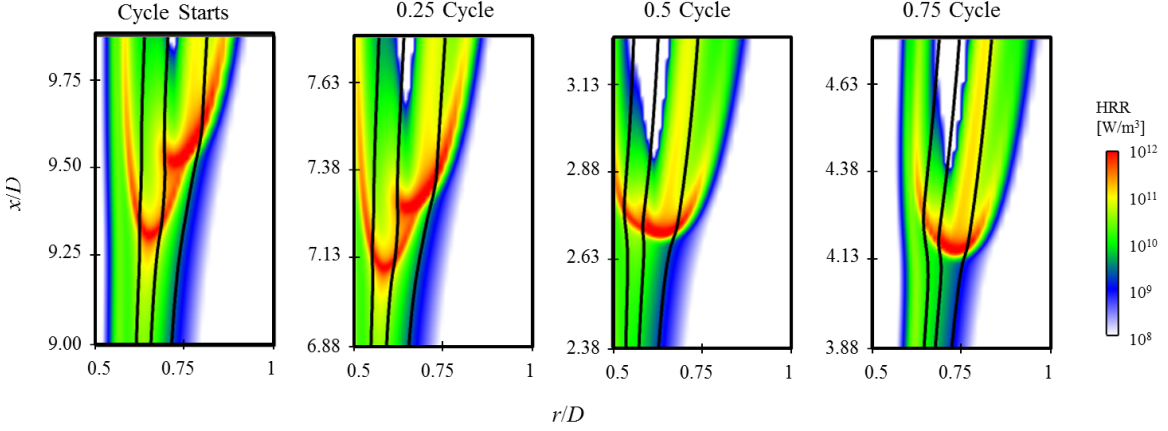


Figure 3.19: Heat release rate [ $\text{W}/\text{m}^3$ ] profile evolution during one oscillation cycle at 100 Hz. The iso-contours of  $Z_{\text{st}} = 0.1$ ,  $Z = 0.2$ , and  $Z = 0.3$  are outlined from right to left in solid lines, respectively.

ity oscillation, the dominant combustion process will shift between the nonpremixed tribrachial flame mode and the autoignition mode. Therefore, the transition in combustion mode is first presented. The thermal and chemical differences during such transition and the transition mechanism are then discussed. Finally, the effects of oscillation frequency on the coupling of fluid dynamics and chemical kinetics is elucidated. The understanding of the coupling effects of chemistry and transport obtained lays the foundation for future turbulent studies.

### 3.4.1 Thermal Structure

As the largest and smallest inlet velocity cases were designed to match the two extreme cases in Sec. 3.3, which are of different thermal structures, it is expected that similar thermal structures will be obtained. Furthermore, these thermal structures might transition back and forth in response to the oscillating flow field. Indeed, such transitions were observed for all three frequencies. For example, the evolution of the thermal structure of the 100 Hz case, in terms of the heat release rate profile, is demonstrated in Fig. 3.19. The oscillation cycle starts with the largest inlet velocity of 8.0 m/s, and the minimum inlet velocity (2.4 m/s) is achieved at half cycle.

At 8.0 m/s, the multibrachial thermal structure is located furthest downstream. The leading point, which is defined as the most upstream point that has the heat release rate value of  $10^{12}$  W/m<sup>3</sup>, is located at mixture fraction  $Z = 0.24$ . As the inlet velocity decreases, the multibrachial structure moves upstream, without obvious change of the leading point location, in terms of mixture fraction. When the inlet velocity reaches its minimum, the multibrachial structure transitions to a tribrachial structure, and the leading point switches to  $Z = 0.14$ . As the flow velocity increases, the tribrachial structure is pushed downstream, and both its tribrachial shape and its leading point mixture fraction remain unchanged. The thermal structure returns to that of multibrachial when the flow velocity further increases. Such transitions in structure repeat once a new oscillation cycle starts.

### 3.4.2 Differentiation of Combustion Mode

In Sec. 3.3 the morphology of the thermal structures are related to two different combustion modes: tribrachial flame and autoignition. Specifically, at steady state, the multibrachial structure in the 8.0 m/s case is an autoignition front, while the 2.4 m/s case is a tribrachial flame. In the previously presented steady cases, species mass fraction profiles at the inlet of the two-dimensional computation are treated as the initial conditions for one-dimensional Lagrangian Flamelet Analysis [122], which only considers diffusion processes parallel to the mixture fraction gradient and neglects those in the normal direction. When the LFA prediction agrees with the CFD result, transport in the normal direction of the mixture fraction gradient is negligible, and autoignition is the dominant combustion process. However, due to the unsteadiness in the oscillating cases, such comparison between LFA and CFD is no longer applicable, and a new criterion to differentiate the modes of tribrachial flame and autoignition needs to be identified and validated against the steady cases.

A density-weighted displacement speed,  $S_d$ , is often used to distinguish between deflagrations and spontaneous ignition fronts in HCCI combustion [162], which is defined from an iso-line of species  $k$  as [130, 65]:

$$S_d = \frac{1}{\rho_u |\nabla Y_k|} \left( \dot{\omega}_k - \frac{\partial \rho Y_k V_{j,k}}{\partial x_j} \right), \quad (3.7)$$

where  $Y_k$ ,  $V_{j,k}$ , and  $\dot{\omega}_k$  denote species mass fraction, diffusion velocity in the  $j$ -direction, and net production rate, respectively, and  $\rho_u$  is the density of the unburnt mixture. The choice of species  $k$  and its iso-line value can be ambiguous. Therefore, major products, such as CO<sub>2</sub>, H<sub>2</sub>O, H<sub>2</sub>, CO, and combinations of these products have been tested, and the sampling location is chosen as the leading point, as defined above, to enable further comparison with the steady cases.  $S_d$  at the leading point is insensitive to the choice of species, for less than 5% difference was observed across all the combinations. Consequently, H<sub>2</sub>O was chosen for simplicity. Both the laminar flame speed  $S_L$  and the unburnt mixture density  $\rho_u$  were obtained from laminar flame speed calculations using the FlameMaster code [121]. The composition and temperature boundary conditions for the laminar flame speed calculations were based on the sampled mixture fraction at the leading point and linearly interpolated, in the mixture fraction space, between the corresponding inlet values of the fuel and coflow streams.

Following the above procedure, displacement velocities were calculated for all three oscillation frequency cases, with 20 points per cycle, to demonstrate their evolution. Furthermore, as shown in Fig. 3.20,  $S_d/S_L$  for the two steady cases (2.4 and 8.0 m/s) were similarly calculated to validate this definition of normalized displacement velocity and differentiate between tribrachial flame and autoignition. For clarity, only the 100 Hz case is included in Fig. 3.20 to elucidate its evolution, and the effect of the oscillation frequency will be discussed in Sec.3.4.3.

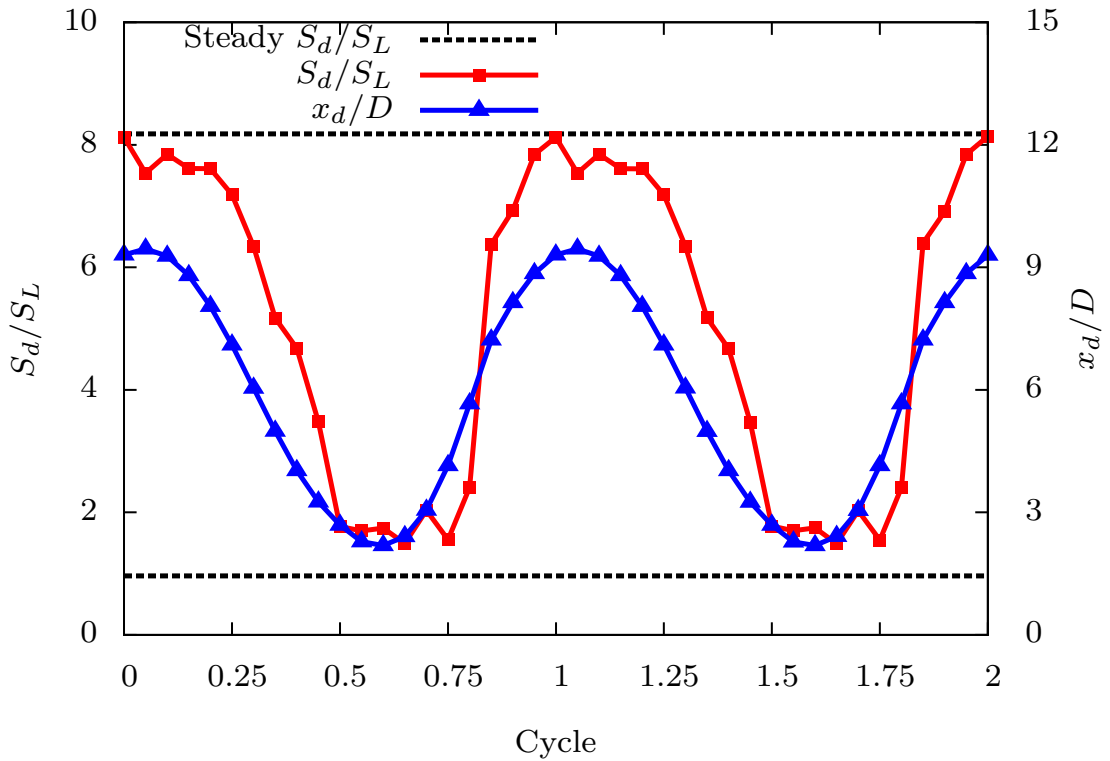


Figure 3.20: Normalized displacement velocity (red) and leading point location (blue) time history profiles at 100 Hz.

The normalized displacement velocities for the steady autoignition front and tribrachial flame are shown in Fig. 3.20 as the top and bottom horizontal lines, respectively. The  $S_d/S_L$  for the steady tribrachial flame is around unity, while this value is around eight for the autoignition front. These values are similar to those in HCCI combustion studies [162] and therefore can be used to benchmark the unsteady cases. The periodic time history profile of  $S_d/S_L$  is bounded by but does not fully reach the two steady values, indicating that, while the chemical structure responds to the flow dynamics, such response is not fast enough to reach steady-state.

When  $S_d/S_L$  approaches the tribrachial flame limit, its value is almost constant, while the change near the autoignition limit is more sinusoidal. Moreover,  $S_d/S_L$  changes more abruptly when the combustion mode switches from tribrachial flame to autoignition. Compared to the profile of the normalized leading point location

$(x_d/D)$ , which is almost sinusoidal, the profile of the normalized displacement velocity is asymmetric, indicating that the transition from tribrachial flame to autoignition as the inlet velocity increases is not an exact reverse process of the transition from autoignition to tribrachial flame. Indeed, as shown in Fig. 3.19, although the inlet velocities at 0.25 and 0.75 cycle are the same, the structures demonstrate different morphologies during the cycle of decreasing- and increasing-velocity: there is hysteresis during the transition.

Such hysteresis is demonstrated more clearly in Fig. 3.21, where  $S_d/S_L$  is plotted against the inlet velocity. Given the same inlet velocity, the reacting fronts have different displacement velocities during the cycle of decreasing- and increasing-velocity. Additional evidence of hysteresis, shown in Fig. 3.19, is the shift in the location of the leading point in the mixture fraction space:  $Z = 0.14$  when the tribrachial flame dominates and  $Z = 0.24$  when autoignition dominates. The shift in the leading point mixture fraction as well as the displacement velocity indicates different dominant chemical reactions, and analysis of the dominant chemical reactions will reveal the mechanism of the hysteresis.

From the steady case analysis in Sec. 3.3, the dominant chemical pathways are found to be different at the leading point of the tribrachial flame and autoignition front. Specifically, the hydrogen peroxide branching reaction ( $\text{H}_2\text{O}_2 + \text{M} \rightleftharpoons \text{OH} + \text{OH} + \text{M}$ ) is the dominant chain branching reaction at the leading point of the autoignition front, while the H radical branching reaction ( $\text{H} + \text{O}_2 \rightleftharpoons \text{O} + \text{OH}$ ) is the most important chain branching reaction at the tribrachial flame leading point. Due to the longer residence time, hydrogen peroxide accumulation is much higher upstream of the autoignition front compared to the tribrachial flame front.

As hydrogen peroxide plays different roles in the tribrachial flame and autoignition front, its spatial profiles along the  $Z = 0.14$  and  $Z = 0.24$  iso-contours are compared in Fig. 3.22, with the left and right subfigures corresponding to the decreasing-velocity

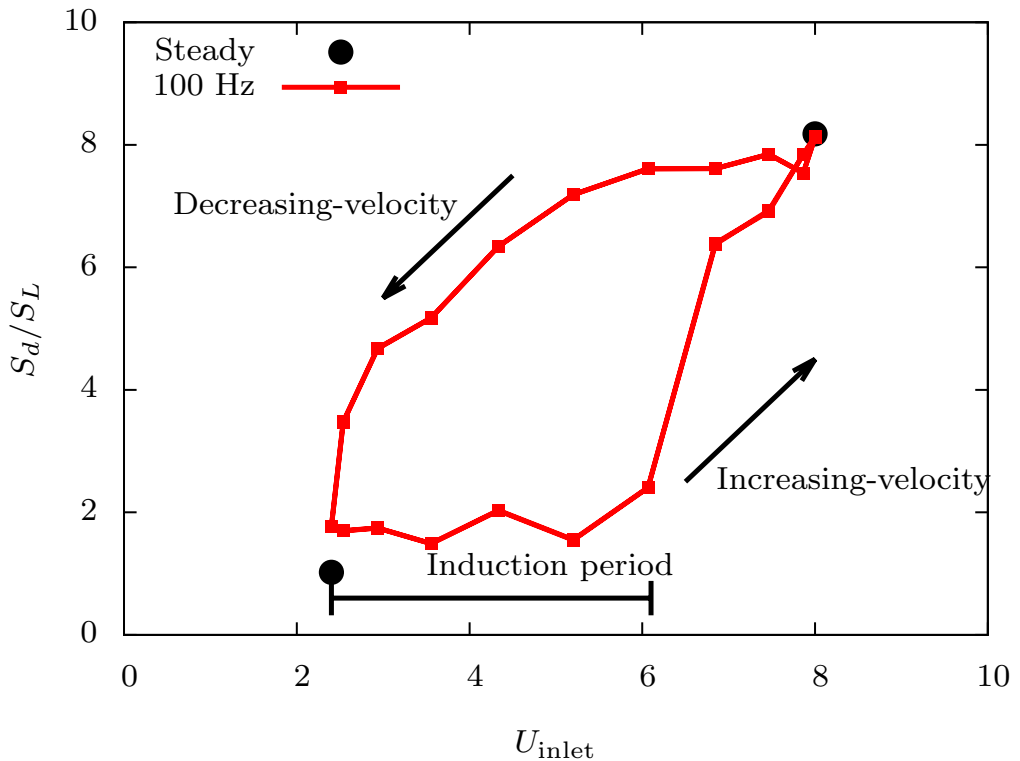


Figure 3.21: Normalized displacement velocities at various inlet velocities for two steady cases and the 100 Hz oscillating unsteady cases.

and increasing-velocity half cycles, respectively. Qualitatively, the evolution of the hydrogen peroxide profiles shows similar trends along both mixture fraction iso-contours. The left figures show that hydrogen peroxide accumulates until either autoignition occurs or it is consumed at the flame front, resulting in a sharp drop in its mass fraction. However, depending on the mixture fraction, the peak value of the hydrogen peroxide mass fraction differs by three to five times between a steady autoignition front (the steady 8.0 m/s case) and a tribrachial flame (the steady 2.4 m/s case), which implies its different significance in these two combustion modes and sets the benchmark for the unsteady evolution. As the inlet velocity decreases from 8.0 m/s, the peak  $Y_{\text{H}_2\text{O}_2}$  almost remains constant, indicating that the chemical structure is very close to the steady autoignition case. As a consequence, the dominant chemical pathway remains  $\text{H}_2\text{O}_2 + \text{M} \rightleftharpoons \text{OH} + \text{OH} + \text{M}$ , and autoignition is the dominant combus-

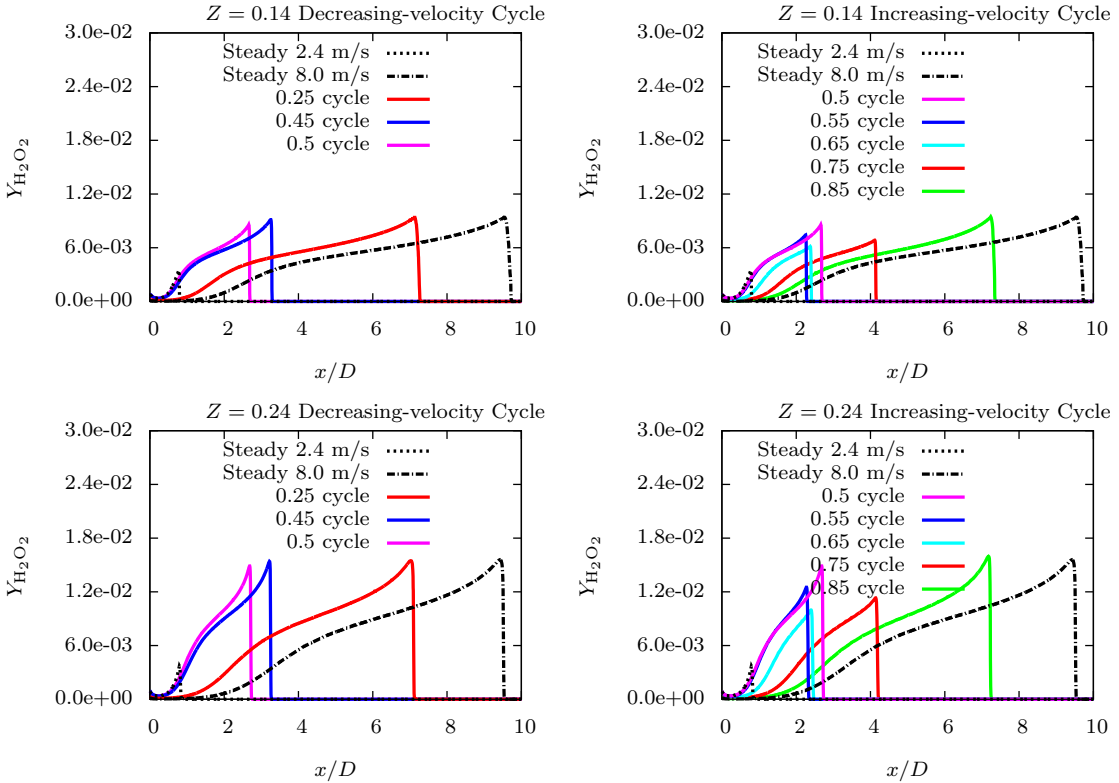


Figure 3.22: Comparison of hydrogen peroxide mass fraction profiles along the  $Z = 0.14$  and  $Z = 0.24$  iso-contours at steady state and at 100 Hz during the decreasing-velocity cycle (left) and increasing-velocity cycle (right).

tion process, resulting in larger  $S_d/S_L$ . However, as the flow velocity decreases, a larger gradient is achieved, resulting in steeper profiles and smaller  $S_d/S_L$ , according to Eq. (3.7). The large gradient results in enhanced back diffusion from the reacting front to the unburnt upstream mixture and ultimately drives the transition into a tribrachial flame.

Even when the inlet velocity reaches the minimum 2.4 m/s, which is the same as the steady case, the reacting front continues to move upstream. Inlet velocity changes slowest around the half cycle, allowing the chemical structure to respond to the hydrodynamic changes. As shown on the right of Fig. 3.22, the peak  $Y_{\text{H}_2\text{O}_2}$  decreases from 0.5 to 0.65 of the cycle. At this stage, autoignition is not fully activated, since the peak  $Y_{\text{H}_2\text{O}_2}$  is lower than the steady autoignition case. However, the peak  $Y_{\text{H}_2\text{O}_2}$  is

still larger than the steady tribrachial flame. Therefore, the  $S_d/S_L$  of the tribrachial structure is close to but slightly larger than a steady flame, for it is propagating into a partially reacted mixture.

As the inlet velocity further increases from 0.65 to 0.75 of the cycle, the propagation speed of the tribrachial flame cannot keep up with the flow incoming velocity, and the flame structure is therefore convected downstream. During this flame blow-off process,  $S_d/S_L$  remains essentially constant, which is demonstrated as the flattened bottom in Fig. 3.21. Meanwhile, the unburnt mixture upstream of the flame accumulates radicals and heat as it moves downstream and eventually triggers autoignition, indicated by a sudden jump of  $S_d/S_L$ . The time difference between the half cycle (where the inlet velocity is 2.4 m/s) and the last sample point before the sudden jump of  $S_d/S_L$  is defined as the induction period, as indicated in Fig. 3.21.

### 3.4.3 Effects of Oscillation Frequency

To better understand the coupling between hydrodynamics and chemistry and the hysteretic behavior in Fig. 3.21, the effects of oscillation frequency are analyzed. Compared to the 100 Hz case, the other two cases of lower oscillation frequency are similar qualitatively but with some quantitative differences. Figure 3.23 shows the evolution of the normalized leading point location ( $x_d/D$ ) for the three oscillating cases, compared with the steady benchmark cases. The peak-to-peak variation represents the oscillation amplitude during a cycle. Two distinct trends are evident. First, as the oscillation frequency increases, the oscillation amplitude decreases. Extrapolating, if the oscillation frequency were much faster than any chemical or transport times scale, the oscillation amplitude would be zero, since the thermal structure could not respond to the velocity changes.

Second and more interestingly, for all three frequencies, the most downstream points during the oscillation are almost identical to the steady case at 8.0 m/s. How-

ever, as the frequency increases, the most upstream point during the oscillation deviates more from the steady case at 2.4 m/s. The different effects of oscillation frequency on the most downstream and upstream points are attributed to the difference in the combustion mode at these two locations. As demonstrated in Fig. 3.21, the 100 Hz oscillating case has already established quasi-steady state when the boundary velocity is at 8.0 m/s when the combustion mode is kinetically controlled by autoignition. In a Lagrangian sense, the location of an autoignition front is directly related to the ignition delay time, determined by chemical kinetics. Therefore, the location of the autoignition front at this quasi-steady state is almost the same as the steady case with the same boundary velocity, which can be crudely estimated as the product of the ignition delay time and the boundary velocity. For even lower frequency cases, such a quasi-steady state is even easier to achieve. Consequently, for all three oscillation frequencies, the most downstream points remain very close to the steady autoignition governed case with the boundary velocity of 8.0 m/s. Conversely, the stabilization mechanism for the steady case at 2.4 m/s is kinematically controlled by the balance between the tribrachial flame propagation speed and the incoming flow speed. For the 100 Hz case, however, such kinematic balance never achieves quasi-steady state, as discussed in the previous section. The location of the tribrachial flame is then determined kinematically both by the velocity difference between the unsteady tribrachial flame propagation speed and the flow speed and the time allowed for such displacement to occur. At lower oscillation frequencies, longer time is allowed for the tribrachial flame to propagate upstream into the partially reacted mixture, while the displacement velocity decreases gradually due to reduced reactivity upstream. The most upstream point location will then asymptotically approaches the steady state case when the oscillation frequency is sufficiently low. This explains why the minimum  $x_d/D$  approaches the steady state case at 2.4 m/s more closely at lower oscillation frequency in Fig. 3.23.

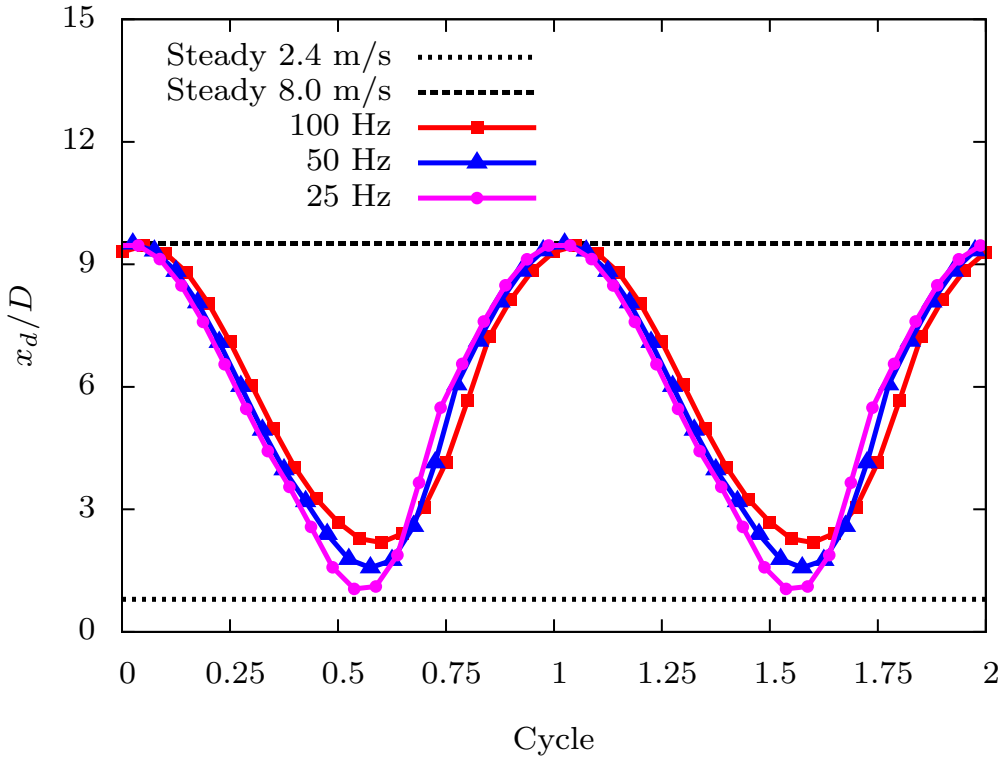


Figure 3.23: Normalized leading point location time history profiles at 25, 50, and 100 Hz.

Besides the oscillation amplitude, the hysteretic behavior is also affected by the oscillation frequency. As shown in Fig. 3.24, the hysteresis of decreasing and increasing velocity is diminished as the oscillation frequency decreases, denoted by the shrinking of the enclosed area. Hysteresis remains at slower inlet velocities since the decreasing-velocity branch is still autoignition dominated, but it takes finite induction time for the increasing-velocity unburnt mixture to achieve autoignition. At higher inlet velocities, both branches are autoignition dominant and therefore collapse to a single path at sufficiently low frequency, approaching the quasi-steady limit. Ideally, the quasi-steady limit could be achieved by investigating even lower frequencies, such as 0.1 Hz; however, such calculation would be extraordinarily intensive, requiring more than 20 million core-hours. Instead, three steady state cases reported previously in Sec. 3.3 and a new steady case at the boundary velocity of 6.4 m/s are also included

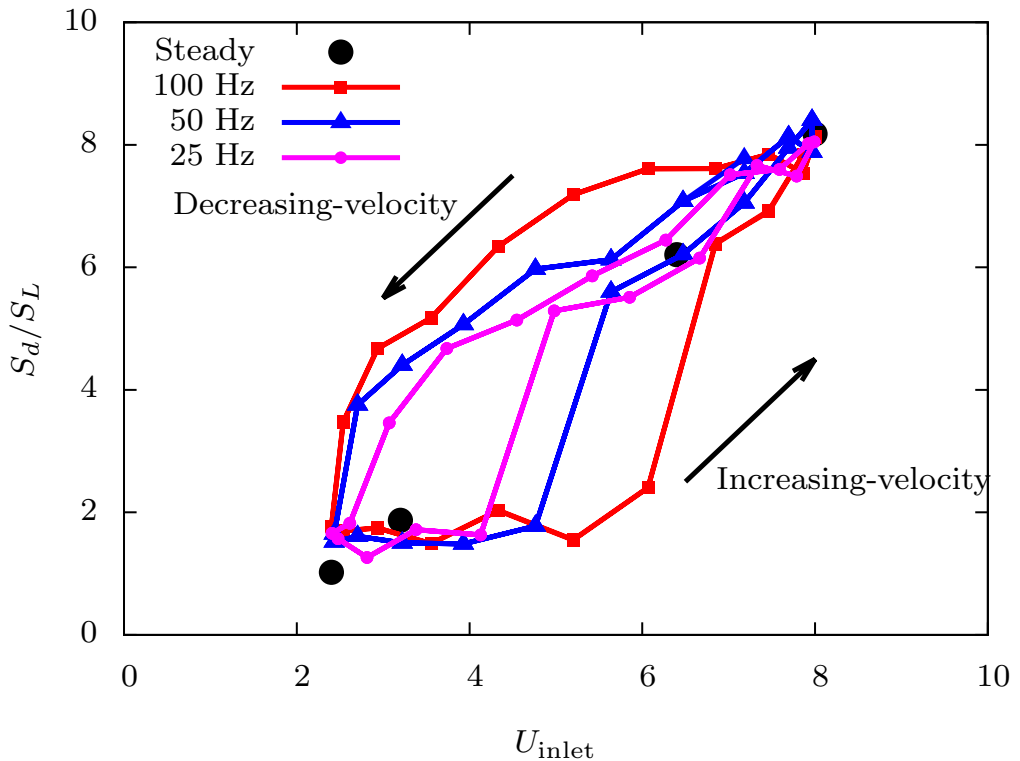


Figure 3.24: Normalized displacement velocities at various inlet velocities for four steady cases and three oscillating unsteady cases at different frequencies. Induction periods for the unsteady cases can also been defined similar to Fig. 3.21 but are not shown here for clarity.

in Fig. 3.24 to illustrate the steady state limit. The 3.2 m/s case is kinematically stabilized, similar to the 2.4 m/s case, and therefore is closer to the increasing-velocity branches of the oscillating cases but is different from the decreasing-velocity branches for the same reason at the lower velocity condition, as discussed in the previous section. Conversely, the 6.4 m/s case is kinetically stabilized by autoignition, which can be approached by both the decreasing-velocity and increasing-velocity branches at lower oscillation frequency.

In terms of the relative portion of the oscillation cycle, the 100 Hz case demonstrates a more pronounced hysteresis and longer induction period. However, in term of the absolute time, shown in Table 3.3, the 25 Hz case takes a longer time to achieve the transition from small  $S_d/S_L$  to larger values during the increasing-velocity portion

Table 3.3: Induction time at different harmonic oscillation frequencies. The definition of the induction time is illustrated in Fig. 3.21

Frequency [Hz]	25	50	100
Induction Time [ms]	6	4	2.5

of the cycle , noting that the time intervals between sampling points in Fig. 3.24 are not the same for the three frequencies, being 0.5, 1.0, and 2.0 ms for 100, 50, and 25 Hz, respectively.

This counter-intuitive finding is explained with Fig. 3.25. Here, the temperature, hydrogen peroxide, and methoxymethylperoxy radical ( $\text{CH}_3\text{OCH}_2\text{O}_2$ ) profiles are compared for the three frequency cases for both decreasing- and increasing-velocity branches at the same inlet velocity of 3.2 m/s and benchmarked with the corresponding steady computation. As in Secs. 3.2 and 3.3, this steady case is autoignition dominated and stabilized at  $Z = 0.24$ .

According to the temperature profiles, the steady and unsteady cases all demonstrate two heat release stages, with the first and second stage correlated well with the depletion of the  $\text{CH}_3\text{OCH}_2\text{O}_2$  radical and hydrogen peroxide, respectively. The  $\text{CH}_3\text{OCH}_2\text{O}_2$  radical is often chosen to represent the NTC chemistry [80]. As demonstrated in the steady cases, NTC chemistry is important in the upstream of both tribrachial flame and autoignition front, and NTC chemistry is still important for the unsteady cases. It is seen from Fig. 3.25 that, irrespective of the oscillation frequency and traveling direction, at the same inlet velocity,  $Y_{\text{CH}_3\text{OCH}_2\text{O}_2}$  matches with its steady state profile, indicating that NTC chemistry responds to the flow oscillation relatively fast, and therefore is decoupled from flow dynamics.

Conversely, the coupling between fluid dynamics and second-stage autoignition/flame chemistry is important, for the hydrogen peroxide profiles of the unsteady cases fail to collapse onto that of the steady case. Although three unsteady profiles on the decreasing-velocity branch show similar peak values, the lower the frequency,

the closer the profile matches the steady case, which is expected from Fig. 3.24. However, the unsteady profiles on the increasing-velocity branch show lower peak values than the steady structure, with the 100 Hz case profile being closer to the steady counterpart. Noting from Fig. 3.24 that the minimum  $S_d/S_L$  in all three cases are larger than the steady 2.4 m/s case and at lower frequency the unburnt mixture has longer time to relax to steady state, the 25 Hz case should match the 2.4 m/s steady case closer, that is, a tribrachial flame with low H<sub>2</sub>O<sub>2</sub> accumulation. Therefore, a longer time is required to accumulate this lost H<sub>2</sub>O<sub>2</sub> and activate autoignition. Conversely, the 100 Hz case allows less time to relax to a steady flame structure and therefore has larger Y<sub>H<sub>2</sub>O<sub>2</sub></sub> to start with during the increasing-velocity cycle, resulting in a shorter induction time for autoignition.

The different effects of oscillation frequency on the first-stage NTC chemistry and second-stage autoignition/flame chemistry can be understood by comparing the characteristic time scales of these processes. The ignition delay time for the first-stage ignition facilitated by NTC chemistry is relatively short ( $\sim$ 0.3 ms, according to Sec. 3.3) compared to the major autoignition process induced by the hydrogen peroxide branching reaction ( $\sim$ 1 ms, according to Sec. 3.3) and the characteristic hydrodynamic oscillation time (10-40 ms in the unsteady cases). Therefore, for the low frequency oscillations investigated in this section, the fluid dynamics and second-stage autoignition/flame chemistry coupling is mainly responsible for the hysteretic behavior and deviation from the steady state.

At even higher oscillation frequencies, the NTC chemistry could interact with the hydrodynamics. Such conditions were attempted computationally, but the elevated frequency resulted in vortex shedding and local flame extinction, which add further complexity.

## 3.5 Summary

In this chapter, the two-dimensional nonpremixed DME flames in heated air coflows were investigated computationally due to the difficulty in well-controlled experiments otherwise. The understanding of the low-temperature chemistry obtained in the one-dimensional counterflow configuration presented in Chapter 2 is beneficial to elucidate the importance of low-temperature chemistry in flame dynamics at elevated temperatures and pressures. In the steady cases, besides the kinematic stabilization mechanism that balances the traditional tribrachial flame propagation in coflows at nonautoignitive conditions, the kinetic stabilization mechanism induced by autoignition can also be important under certain conditions. Since low-temperature chemistry dictates the first-stage autoignition delay time and the subsequent heat release, it affects the morphology of the multibrachial structure of the autoignition front. With advanced computational diagnostics, the thermal and chemical structures as well as the dominant stabilization mechanisms were elucidated for steady cases at various boundary conditions. A regime diagram was proposed to generalize the stabilization mechanism.

Furthermore, realizing that one of the major characteristics of practical engine conditions is unsteadiness, flame dynamics in the same configuration were investigated by forcing harmonic oscillations between two steady cases at different oscillation frequencies. The transition in the combustion mode during the oscillation was observed and quantified. Finally, the coupling effects of low-temperature chemistry, high-temperature chemistry, and transport were elucidated. Such understanding could be beneficial to future turbulent studies.

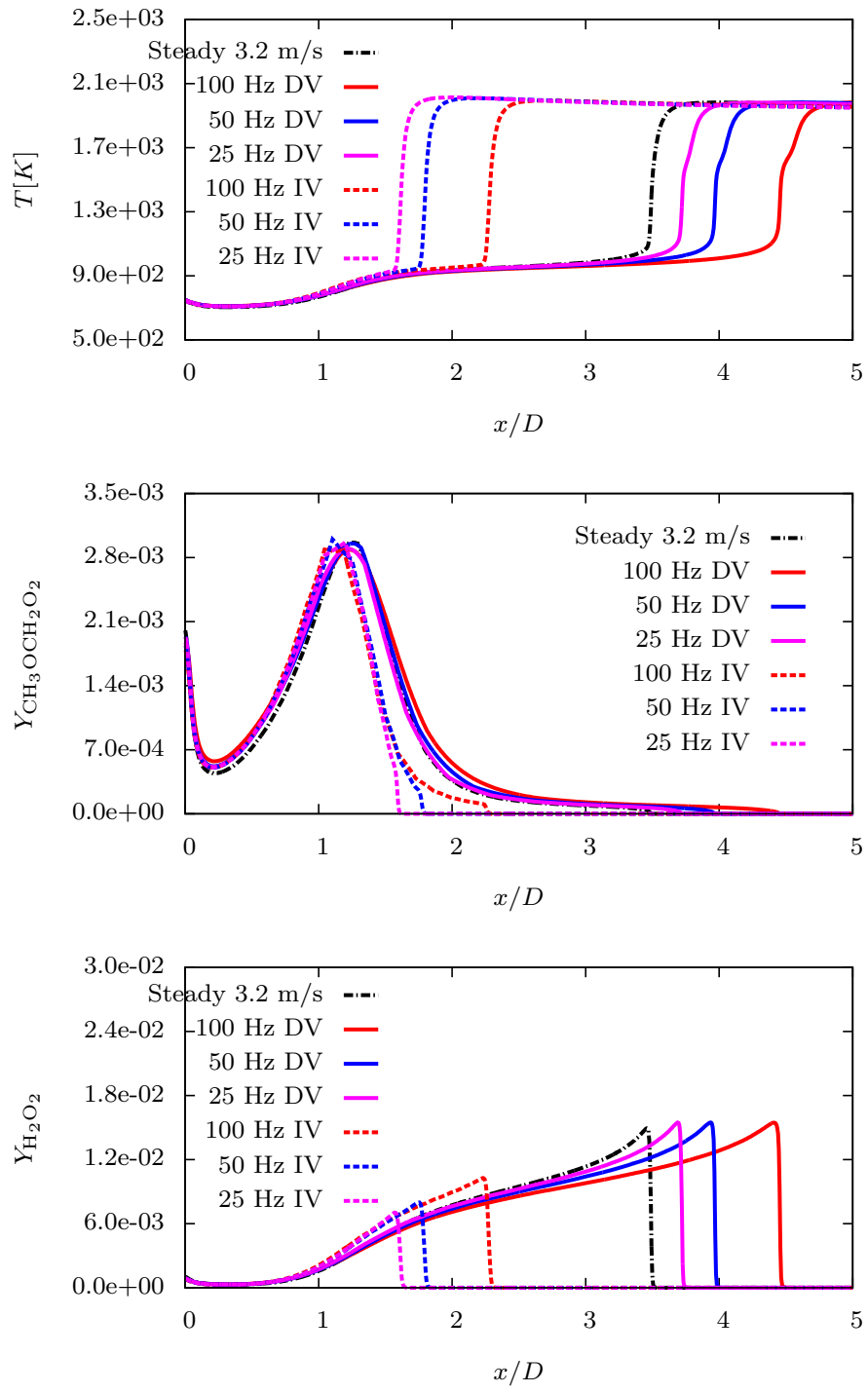


Figure 3.25: Temperature, methyoxy methylperoxy radical, and hydrogen peroxide mass fraction profiles along the  $Z = 0.24$  iso-contour at  $3.2 \text{ m/s}$ . DV: decreasing-velocity, and IV: increasing-velocity.

# Chapter 4

## Sooting Limits of Laminar Stagnation-Flow Flames

Soot emission control is an important research area in combustion. As reviewed in Chapter 1.2.2, the fundamental understanding of the chemical kinetics in sooting flames is still under development. Although oxygenated additives have been found to reduce particular matter emissions [53], the precise role of oxygenated additives on soot emission reduction has not yet come to a scientific consensus. Moreover, since soot formation is a kinetically controlled process [149], the finite residence time effect also needs to be considered. Therefore, the experimental and computational investigation of sooting limits of three neat liquid diesel/biofuel components, specifically, *n*-heptane, *n*-butanol, and methyl butanoate, in a nonpremixed stagnation-flow is presented in this chapter. A combined chemical kinetic model with detailed polycyclic aromatic hydrocarbon (PAH) chemistry is constructed to investigate the important pathways of soot formation with these three fuels.

This choice of the target fuels is motivated by both practical and scientific concerns. First, butanol has more diverse non-food sources of supply than ethanol, which has been derived primarily from corn. Second, methyl butanoate is chosen not only

because it is a typical biodiesel surrogate but also due to the availability of detailed chemical kinetic models. Third and most important, the boiling points of *n*-butanol and methyl butanoate are 391 K and 375 K, respectively, which are very close to that of *n*-heptane (372 K). This similarity in the vaporization characteristics enables similar fuel vapor concentrations and assures similar rates of supply of the vaporized fuel to the flame region.

## 4.1 Experimental Methodology

The sooting limits of nonpremixed model diesel/biofuel components, in terms of the critical strain rate (CSR) at which soot inception starts to happen when the residence time, which is the inverse of the strain rate, is further increased, were measured at atmospheric pressure in a liquid pool stagnation-flow configuration. An unheated oxidizer stream impinged against the liquid fuel pool, and flames were established by spark ignition. Coflowing nitrogen was utilized as the shielding gas to minimize the disturbance from the surroundings. With the 20 mm nozzle and pool diameter, the separation distance between the oxidizer nozzle and liquid pool was maintained at 13 mm to assure a well-characterized stagnation flow and also to enable better measurement of the velocity field by Laser Doppler Velocimetry (LDV). The schematic of the liquid pool stagnation-flow apparatus is shown in Fig. 4.1, and details about the auxiliary system can be found elsewhere [91].

Due to the oxygen content in *n*-butanol and methyl butanoate, their flame temperatures are lower than *n*-heptane. Since soot formation is highly sensitive to temperature [153], this thermal effect has to be eliminated to elucidate the chemical effects. In the present study, *n*-butanol and methyl butanoate flame temperatures were increased to be the same as *n*-heptane by replacing a portion of the nitrogen in the oxidizer stream with argon, which is the same approach taken by Axelbaum, Law,

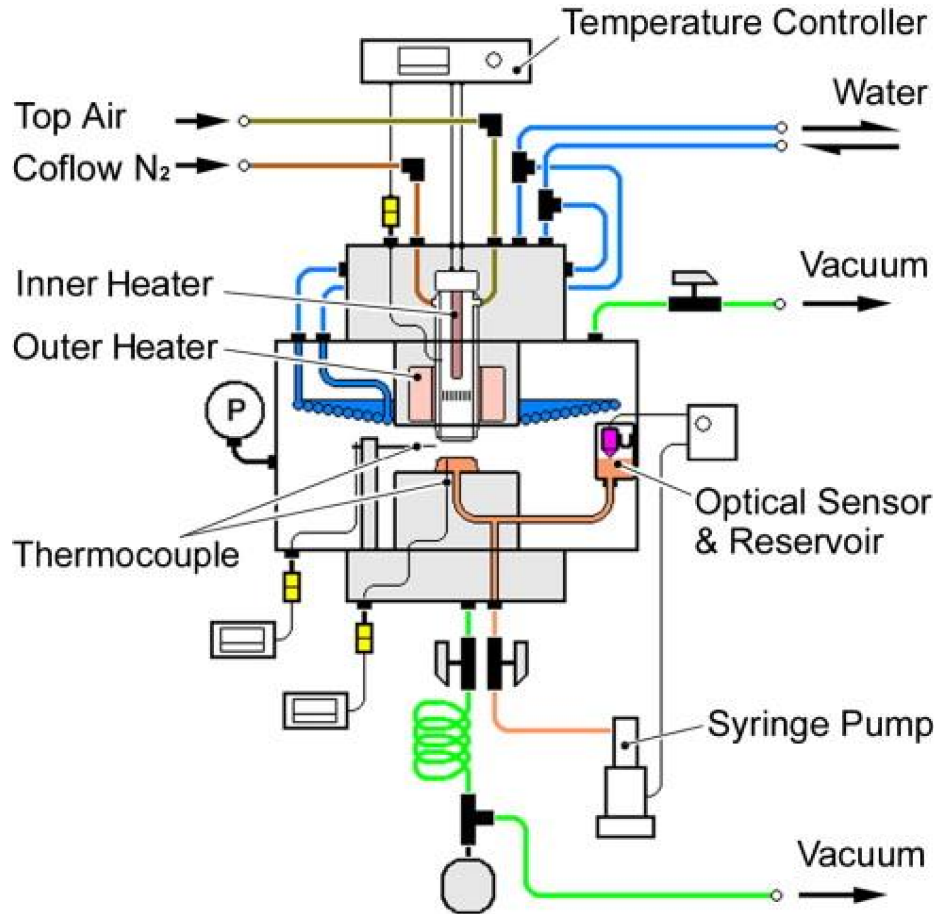


Figure 4.1: Schematic of the liquid pool stagnation-flow apparatus [91]. The heating system was not activated in the current study.

and co-workers [34, 35, 3]. The amount of nitrogen replacement was calculated with CHEMKIN's equilibrium solver EQUIL [74] for stoichiometric fuel/oxidizer mixtures, and the diluent concentrations are summarized in Table. 4.1. Although the replacement was calculated based on premixed stoichiometric mixtures, the thermal environment of all three fuels cases under the same strain rate and oxygen mole fraction in the stagnation-flow configuration is nearly the same, according to the simulations, which will be discussed in detail in Sec. 4.3. Liquid *n*-heptane, *n*-butanol, and methyl butanoate were fed to the liquid pool by a syringe pump at room temperature.

Soot detection was based on luminosity observations with a Nikon D700 camera, for Du *et al.* [34] found that such measurements agreed well with light scattering

Table 4.1: Oxidizer stream composition in mole fractions to maintain the same adiabatic flame temperature of the three fuels with the same oxygen concentration in the oxidizer stream.

		$O_2$							
		0.2000	0.2025	0.2050	0.2075	0.2100	0.2150	0.2200	0.2250
$n - C_4H_9OH$	$N_2$	0.7640	0.7600	0.7560	0.7521				
	$Ar$	0.0360	0.0375	0.0390	0.0404				
$C_5H_{10}O_2$	$N_2$			0.7119		0.7017	0.6915	0.6811	0.6707
	$Ar$			0.0831		0.0883	0.0935	0.0989	0.1043

detection and were a convenient indicator of the presence of soot particles. The experimental procedure to identify the sooting limit is briefly summarized here. First, the oxidizer component flow rates were set, and a non-sooting blue flame was established. Then, the bypass valve placed upstream of the oxidizer nozzle was slowly adjusted to divert oxidizer out of the system, effectively reducing the velocity of the stream and, consequently, the strain rate. The residence time was further increased until yellow luminosity began to appear on the fuel rich side of the flame. A standard single-component LDV measurement was performed along the axial centerline under this threshold flow condition, and the local strain rate was determined as the axial velocity gradient upstream of the flame [34]. Following this procedure, the sooting limits for the three fuels with different oxygen concentrations in the oxidizer streams were identified. Although this luminosity measurement was not quantified, the CSR measurements were found to be repeatable.

## 4.2 Computational Methodology

The liquid pool stagnation-flow flames were simulated with the FlameMaster code [121], including detailed PAH chemistry and a detailed soot model. The boundary conditions on the fuel side were specified following Bui-Pham *et al.* [11]. In brief, the Antoine equation [125] was used to close the boundary value problem by relating the liquid pool surface temperature and vapor pressure, yielding a relationship for

the fuel mole fraction at the surface. As in the experiment, the local strain rate was determined as the gradient of the velocity profile on the oxidizer side, ahead of the flame.

Furthermore, since the luminosity observations cannot be simulated directly, the computational CSRs were determined based on an alternative metric, and a critical value of this metric was chosen to match the experimental results of *n*-heptane at larger  $X_{O_2}$  cases and was kept fixed for all other cases. The global domain-integrated soot volume fraction ( $f_V$ ), the temperature-weighted global domain-integrated soot volume fraction ( $f_V*T^4$ ), and the maxima of the corresponding single-point values were considered as potential metrics. However, the qualitative trends presented in the next section were found to be insensitive to the choice of the threshold value or determination metrics that were explored. Therefore, the global domain-integrated  $f_V$  ( $m^3/m^2$ ) were chosen as the metric for computational determination of CSRs in the following sections.

#### 4.2.1 Chemical Model

A detailed chemical model including PAH chemistry was constructed from three well validated models corresponding to the fuels of interest. A mechanism with PAH chemistry of engine relevant fuels was developed by Blanquart, Pitsch, and co-workers [8, 110]. This mechanism has been validated extensively against experimental measurements of ignition delay times, laminar burning velocities, and species profiles in both premixed and nonpremixed flames over a large range of equivalence ratios and pressures for small hydrocarbons, C<sub>3</sub> and C<sub>4</sub> species, (substituted) aromatics, *n*-heptane, and iso-octane. Of particular interest to this work, the mechanism was validated in *n*-heptane nonpremixed flames against the measurements of Berta *et al.* [4]. This mechanism was adopted as the base mechanism with PAH chemistry. Reduced oxidation/pyrolysis chemistry of *n*-butanol and methyl butanoate kinetic

models was adopted from Liu *et al.* [88] and combined with the base mechanism. These models were reduced from the detailed mechanisms of Sarathy *et al.* [132] and Gail *et al.* [48], respectively. Details about the mechanism reduction, validation, and reduced mechanisms can be found in Liu *et al.* [88]. All the common reactions among the base mechanism and the additional mechanisms were retained from the base mechanism to maintain compatibility with the PAH mechanism. The thermal and transport data of the species that appeared only in the *n*-butanol and methyl butanoate mechanism were taken from these latter works, and species in common were taken from the base mechanism. The combined mechanism consists of 220 species and 2259 forward and backward reactions; none of the reaction rate parameters were adjusted in the combined mechanism.

The combined mechanism was validated against laminar flame speed measurements [88] and compared with the predictions by the original mechanisms; results of this validation are shown in Figs. 4.2 and 4.3. As no difference was found between the validation results calculated by the combined and the original *n*-heptane mechanism, *n*-heptane laminar speed validation is not included and can be found in the referenced works [8, 110]. The differences between the combined mechanism and the original mechanism for *n*-butanol and methyl butanoate are attributed to the differences in the base chemistry, with the combined mechanism generally giving improved agreement with the experimental measurements.

In addition, the combined mechanism was further validated against extinction strain rate (ESR) measurements in the nonpremixed liquid pool stagnation-flow system, as shown in Figs. 4.4 to 4.6. The computational ESRs for *n*-heptane and methyl butanoate were compared with the experimental studies of Seshadri and co-workers [137, 114], and details about the experimental procedure and conditions can be found therein. These measurements were augmented with our own measurements of ESR for *n*-butanol with the same apparatus presented in the previous section. The

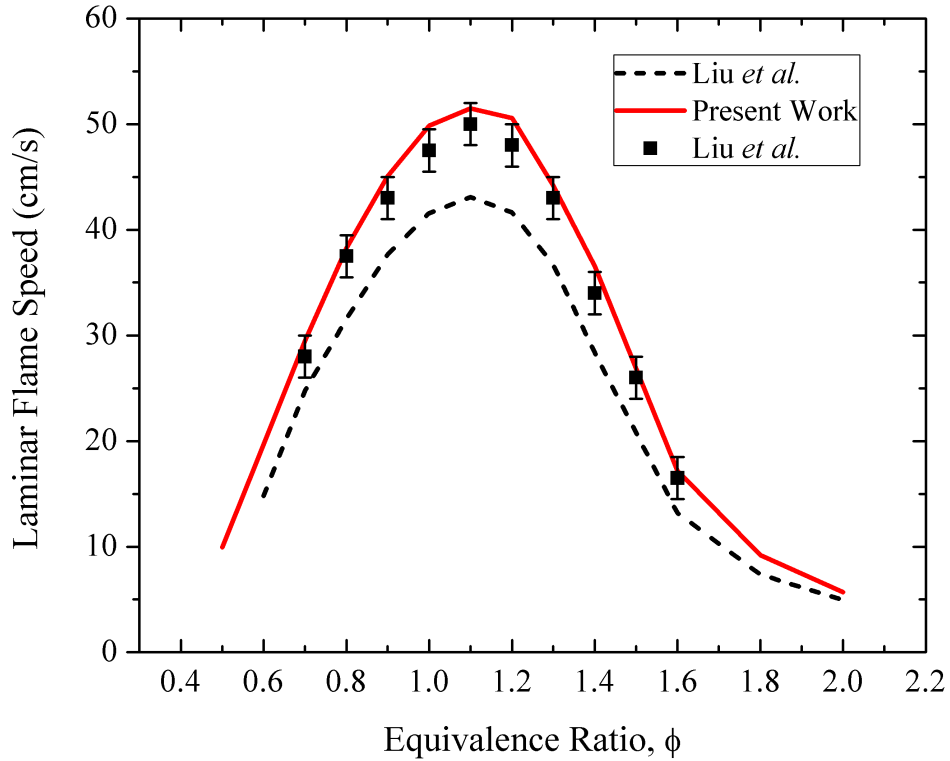


Figure 4.2: Mechanism validation of *n*-butanol laminar flame speeds, against the experimental (symbols) and computational (dotted lines) results from Liu *et al.* [88].  $P = 1$  atm and  $T = 353$  K.

same experimental procedure as Seshadri and co-workers was adopted, except that the ESR was defined by the local strain rate rather than the global one, the former being the fundamentally more relevant quantity. In all cases, the experimental measurements and simulation results were compared based on the same definition of the strain rate. However, as demonstrated in Liu *et al.* [89], determinations based on a given definition are consistent. As shown in Figs. 4.4 to 4.6, computational ESRs for *n*-heptane and methyl butanoate agree well with the experimental measurements and are slightly overpredicted for *n*-butanol.

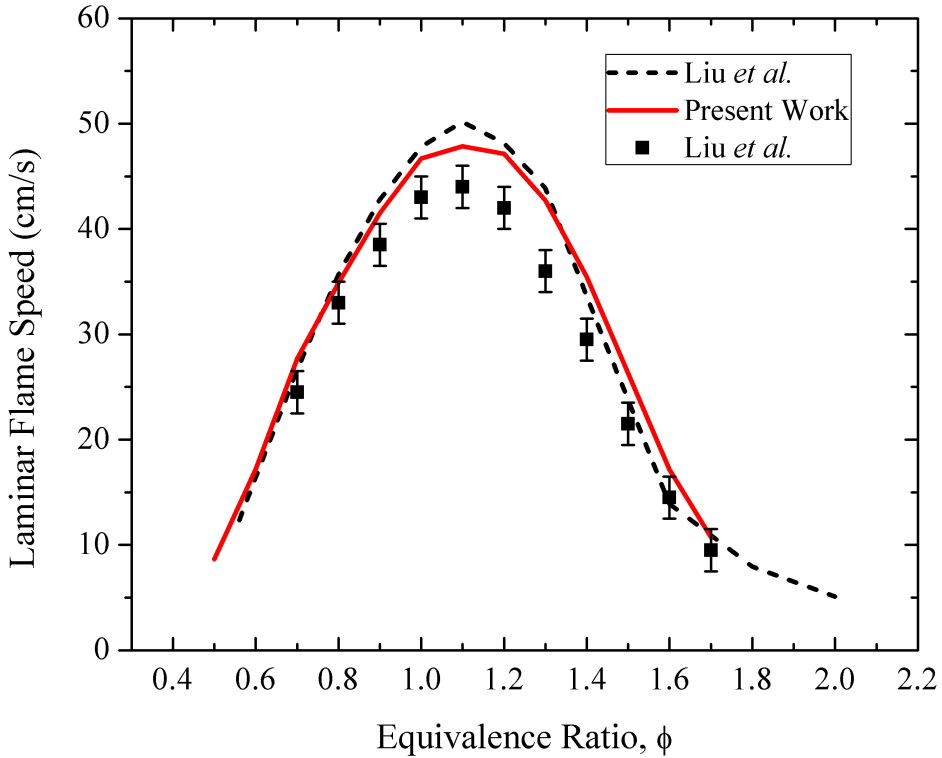


Figure 4.3: Mechanism validation of methyl butanoate laminar flame speeds, against the experimental (symbols) and computational (dotted lines) results from Liu *et al.* [88].  $P = 1$  atm and  $T = 353$  K.

#### 4.2.2 Soot Model

Far too many soot particles are present to track individually, so the population is described statistically with Number Density Function (NDF),  $N_i$ . The NDF describes the size distribution of soot particles and is typically bimodal [165]. Due to persistent nucleation of soot particles from PAH, one mode of the NDF contains the smaller incipient spherical soot particles. The other mode contains larger and more mature fractal aggregates formed from coagulation of smaller spherical primary particles. A two-dimensional internal coordinate is used to define the NDF: the volume  $V$  and the surface area  $S$ . The transport equation governing the evolution of NDF is very high-dimensional (three spatial dimensions and two internal dimensions). Therefore,

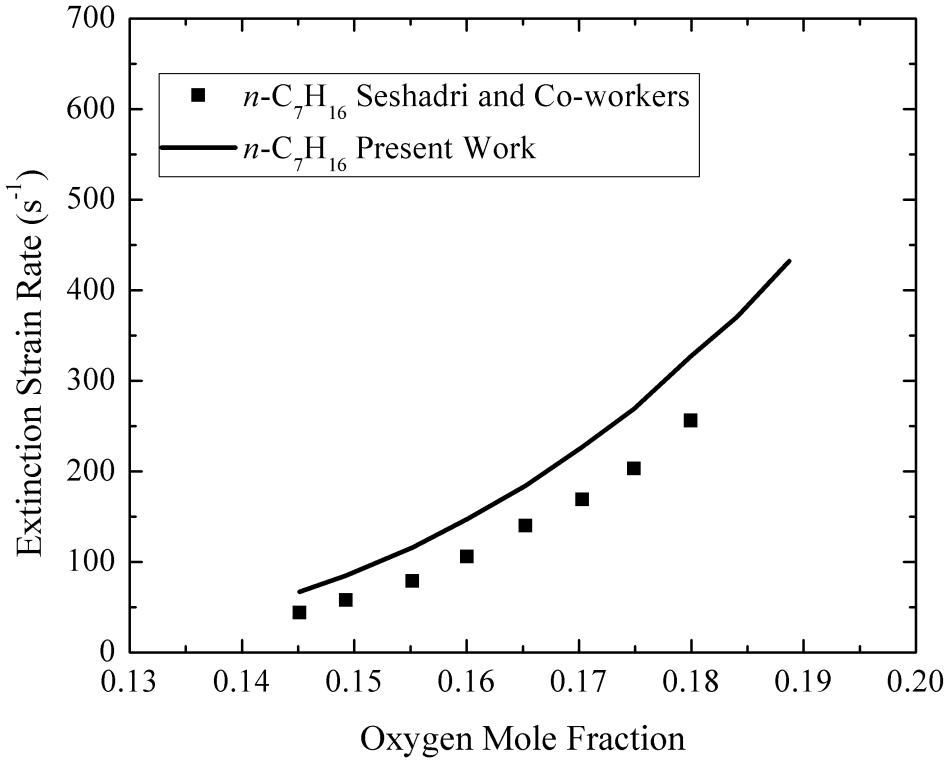


Figure 4.4: Mechanism validation for *n*-heptane against the extinction strain rates measurements in nonpremixed stagnation-flow systems.

the only tractable model is the Method of Moments, in which moments of the NDF are solved for rather than the NDF itself. The moments of the NDF  $M_{x,y}$  are given by

$$M_{x,y} = \sum_i V_i^x S_i^y N_i, \quad (4.1)$$

where summation over all particle sizes is performed. Although the distribution of soot particle sizes is not provided directly with the Method of Moments, quantities that are of interest in engineering applications, such as the soot volume fraction, total number density, average primary particle diameter, etc., are well captured.

The evolution of the NDF is described by the Population Balance Equation (PBE) [46]. Similarly, the transport equation for the evolution of the moments of

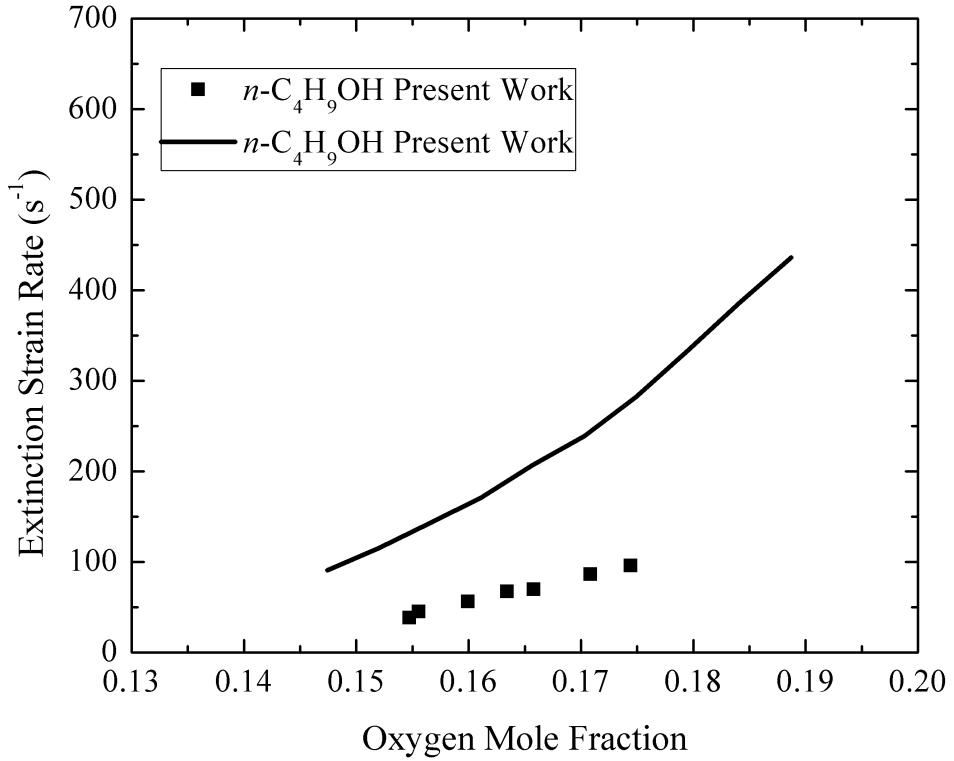


Figure 4.5: Mechanism validation for *n*-butanol against the extinction strain rates measurements in nonpremixed stagnation-flow systems.

NDF can be obtained by taking the moments of the PBE, that is,

$$\frac{\partial M_{x,y}}{\partial t} + \frac{\partial u_i M_{x,y}}{\partial x_i} = \frac{\partial}{\partial x_i} \left( 0.55 \frac{\nu}{T} \frac{\partial T}{\partial x_i} M_{x,y} \right) + \dot{M}_{x,y} , \quad (4.2)$$

where the first term on the right hand side is the thermophoresis of soot particles[152] and molecular diffusion is neglected [6]. Subsequently, this term is combined with the convective term, and the total velocity is denoted by

$$u_i^* = u_i - 0.55 \frac{\nu}{T} \frac{\partial T}{\partial x_i} . \quad (4.3)$$

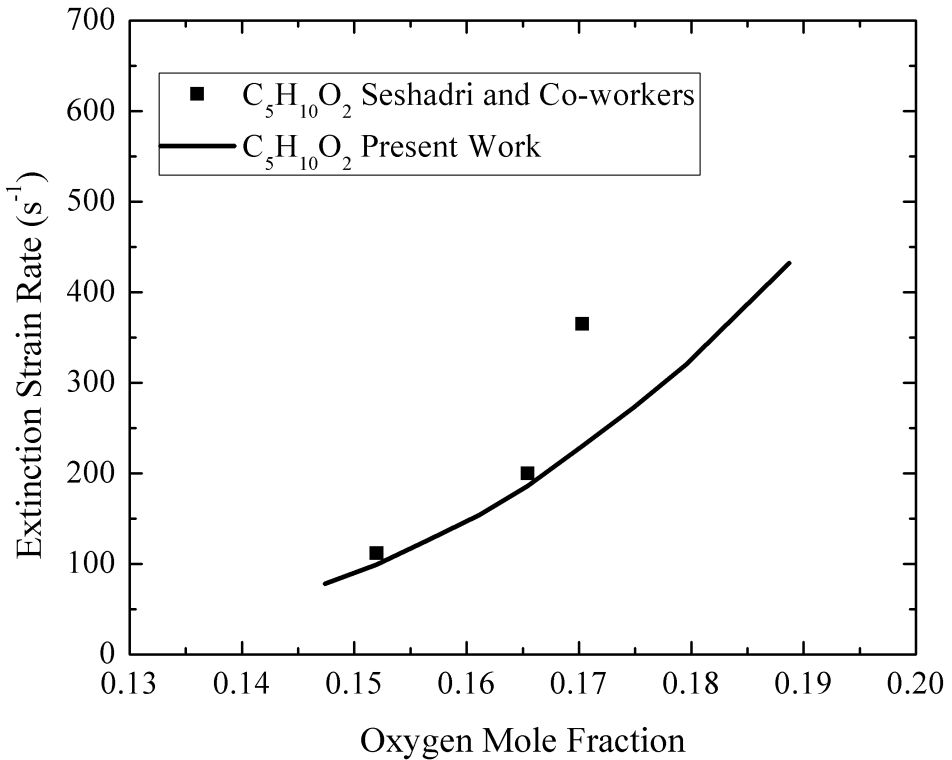


Figure 4.6: Mechanism validation for methyl butanoate against the extinction strain rates measurements in nonpremixed stagnation-flow systems.

The source term in Eq. 4.2 contains incipient soot particle nucleation from PAH dimers [133, 159, 9], PAH condensation [117, 100, 101], particle coagulation [104], surface growth by the HACA mechanism [45], oxidation [71, 113], and oxidation-induced fragmentation [106].

The major challenge with the Method of Moments is the closure problem, which is the fact that the source terms for the moment equations depend on moments which are not solved for. In this dissertation, closure is achieved with the Hybrid Method of Moments (HMOM) developed by Mueller *et al.* [105, 104, 106], and the details of the above models can be found in those works. Briefly, in HMOM, the contribution from the smaller incipient particles to the moments is described with a delta function as in the Direct Quadrature Method of Moments (DQMOM) [96]. Moreover, the

contribution to the moments from the larger particles is described with polynomial interpolation as in the Method of Moments with Interpolative Closure (MOMIC) [44]. Therefore, an arbitrary moment is given by

$$M_{x,y} = V_0^x S_0^y N_0 + \exp \sum_{r=0}^R \sum_{k=0}^r a_{r,k} x^k y^{r-k}, \quad (4.4)$$

where the location of the delta function  $(V_0, S_0)$  is fixed and  $R$  is the order of the polynomial interpolation. A transport equation is solved for the weight of the delta function  $N_0$ . The transport equation for this quantity is the same as Eq. 4.2 with the source term given by

$$\dot{N}_0 = \lim_{\alpha, \beta \rightarrow \infty} \frac{\dot{M}_{-\alpha, -\beta}}{V_0^{-\alpha} S_0^{-\beta}}. \quad (4.5)$$

Given the weight of the delta function  $N_0$ , the polynomial interpolation coefficients are obtained from a set of moments which are solved for. In this work,  $R = 1$ , so three moment equations are solved other than  $N_0$ : the total number density  $M_{0,0}$ , the total soot volume  $M_{1,0}$ , and the total soot surface area  $M_{0,1}$ . Further details about HMOM and the soot model can be found in Mueller *et al.* [105, 104, 106] and the references therein.

### 4.3 Results: Sooting Limits

As mentioned in Sec. 4.1, argon dilution was used to keep the thermal environment of the three fuel cases nearly the same. This is justified with the simulation results of the temperature profiles for three fuel cases under the same strain rate and oxygen mole fraction, as shown in Fig. 4.7. The difference among the peak temperatures is less than 20 K, and the peak locations differ by less than 0.1 mm. Furthermore, on the fuel-rich side, in the vicinity where soot is formed, the maximum temperature difference among the fuels is less than  $\pm 20$  K. Also, simulation results show that the liquid surface

temperatures for all three fuels stay about 20 K below their respective boiling points, and the liquid surface temperatures are nearly constant (within 0.3%), regardless of the change in oxygen mole fractions. Consequently, the thermal environment is maintained nearly the same for all three fuels, and chemical effects have therefore been isolated from thermal effects.

The critical strain rates (CSRs) corresponding to the sooting limits from the experiments and computations are shown in Fig. 4.8. For each set of data, the region above/left of the data corresponds to non-sooting flames, and the region below/right of the data corresponds to sooting flames. For all three fuels, the CSR increases with increasing oxygen concentration in the oxidizer stream, which has been previously characterized as a thermal effect [35]. In addition, both experiment and computation show that methyl butanoate has substantially lower CSRs compared to *n*-heptane and *n*-butanol.

This distinct trend warrants further investigation. Noting that, the CSRs are defined (experimentally and computationally) based on an absolute amount of soot, the fact that the CSRs are substantially lower for methyl butanoate compared to the other two fuels could then be due to either or both of the following hypotheses. First, less soot is formed from methyl butanoate overall, regardless of strain rate. Second, the chemical pathways leading to PAH and soot formation for methyl butanoate are slower and are more strongly suppressed with decreasing residence time (increasing strain rate). The relative roles of these two hypotheses require further analysis.

## 4.4 Mechanistic Analysis

To elucidate the role of the above two hypotheses, mechanistic analysis was conducted for all three fuels to investigate the response of soot volume fraction to strain rate,

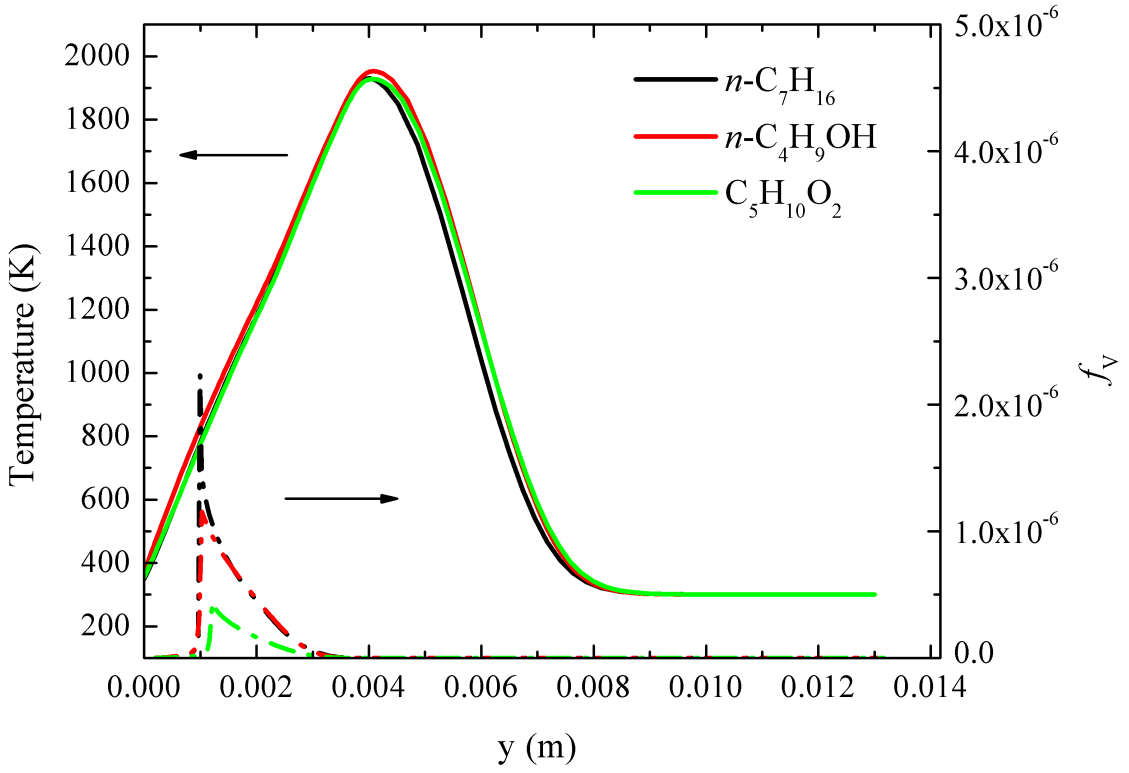


Figure 4.7: Temperature (solid line) and  $f_V$  (dash-dotted line) profiles at the strain rate of  $16 \text{ s}^{-1}$  and  $X_{O_2} = 0.2$ .

chemical pathways for PAH formation, and the rate-limiting steps for PAH formation for each of the three fuels.

#### 4.4.1 Volume Fraction Response to Strain Rate

The integrated  $f_V$  under various strain rates are shown in Fig. 4.9. For all three fuels, as the strain rate increases, less soot is formed due to reduced residence time. At all strain rates,  $n$ -butanol is overall as sooty as  $n$ -heptane, while methyl butanoate is the least sooty. If a critical  $f_V$  is chosen and a horizontal line drawn based on this choice, the intersections of the horizontal line and the three  $f_V$  profiles give the corresponding CSRs for the three fuels. This is indeed how the computational CSRs were determined in the current study. Therefore, the CSRs correlate with the

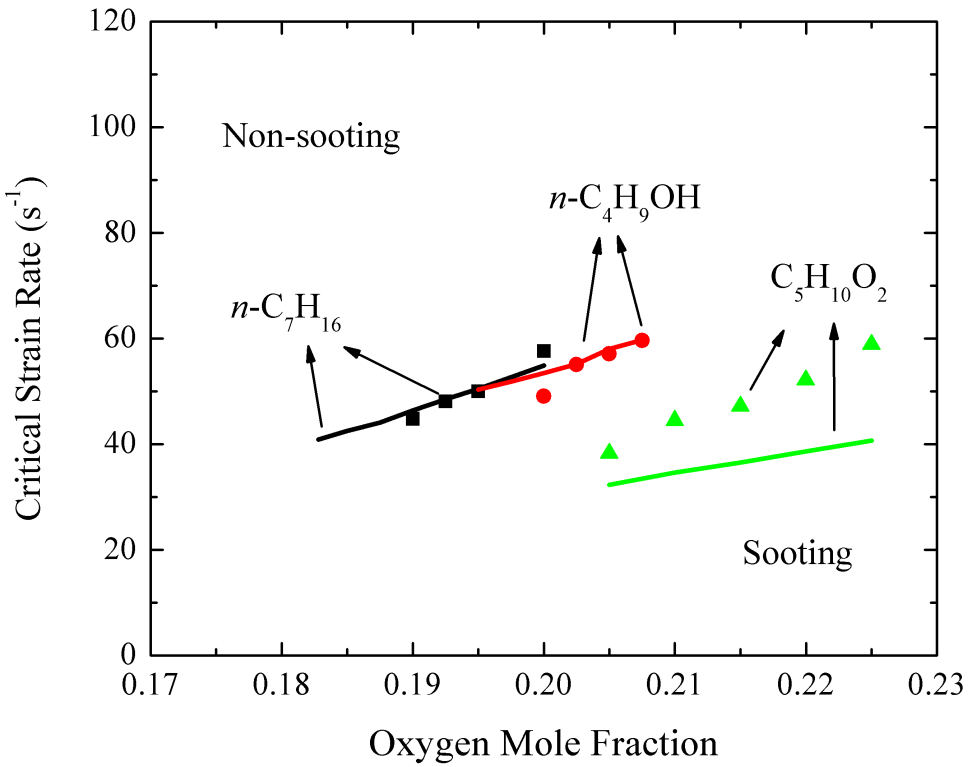


Figure 4.8: Experimental (symbols) and computational (lines) CSRs.

total amount of soot formed, explaining at least in part the CSR trends. However, detailed chemical pathway analysis is still needed to elucidate the differences in the global sooting behavior as well as to see if there are any significant differences in PAH pathways with different timescales for the three fuels that could further explain the observed trends in CSRs.

#### 4.4.2 Sensitivity and Reaction Pathway Analysis

To understand the distinct differences in PAH evolution between the three fuels, sensitivity and reaction path analysis were performed for a representative PAH species, naphthalene ( $\text{C}_{10}\text{H}_8$ ). As shown in Fig. 4.10 and Fig. 4.11, naphthalene shows roughly

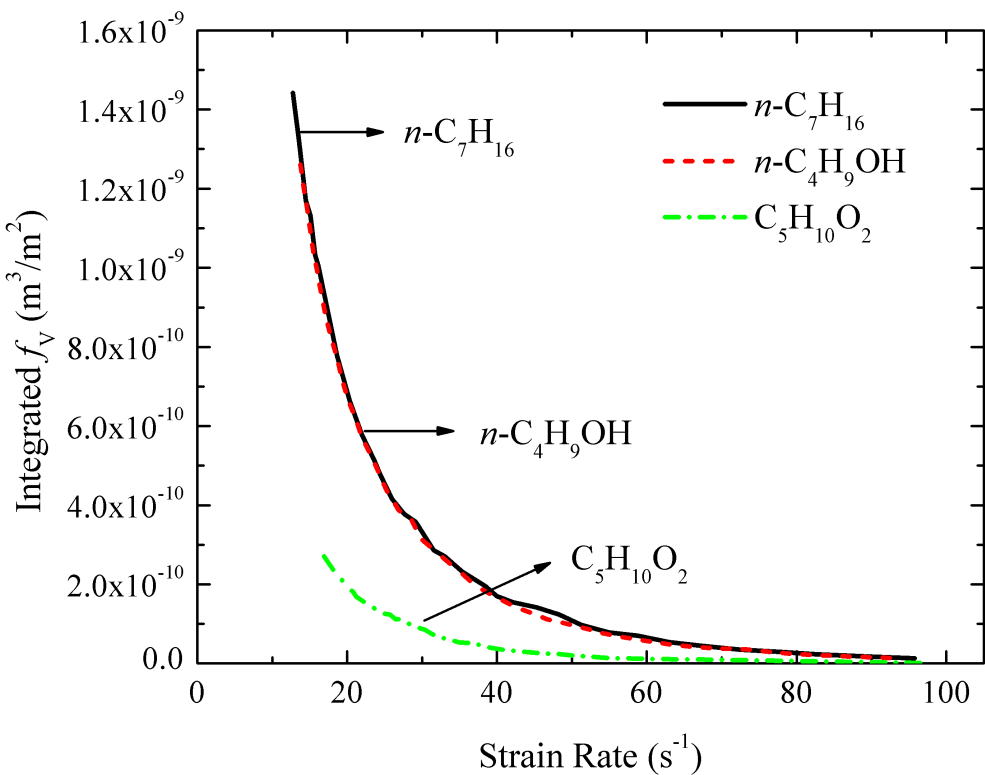
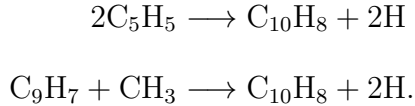


Figure 4.9: The responses of the integrated  $f_V$  to strain rate at  $X_{O_2} = 0.2$ .

the same sensitivities to the same reactions for each of the fuels, and the chemical pathways of naphthalene are essentially the same after the fuel cracking. Initially, fuel cracks to unsaturated C<sub>3</sub> to C<sub>5</sub> chains through H abstraction followed by  $\beta$ -scission reactions. These smaller molecules further decompose into allyl radicals ( $\text{CH}_2=\text{CH}-\text{CH}_2^*$  or A-C<sub>3</sub>H<sub>5</sub>) and propene (C<sub>3</sub>H<sub>6</sub>), which contribute to C<sub>5</sub> and C<sub>6</sub> ring formation by either combining with acetylene (C<sub>2</sub>H<sub>2</sub>) or forming propargyl (C<sub>3</sub>H<sub>3</sub>), the latter further combining with itself to form aromatic rings. Larger species (predominantly toluene and indene) are formed by the combination of benzene and cyclopentadiene with smaller species, such as CH<sub>3</sub>, C<sub>2</sub>H<sub>2</sub>, and C<sub>3</sub>H<sub>3</sub>. Two pathways directly contribute to naphthalene formation, namely, cyclopentadienyl (C<sub>5</sub>H<sub>5</sub>) radical recombination and

methyl addition to indenyl ( $C_9H_7$ )



Although the PAH pathways for the three fuels are similar, the formation of these soot precursors from the fuel cracking processes and the relative importance of the subsequent chemical pathways of PAH growth are fuel specific. Noting the similarity in the chemical pathways beyond  $A-C_3H_5$  and  $C_3H_6$ , the fuel specific breakdown pathways that lead to the generation of these precursors are depicted in Fig. 4.12. For both *n*-heptane and *n*-butanol, 1-butene ( $P-C_4H_8$ ) is a product of the fuel decomposition, and this species contributes to 25% of  $A-C_3H_5$  production and strongly promotes naphthalene formation, as indicated by the sensitivity analysis in Fig. 4.10. Moreover, the fuel bound oxygen in *n*-butanol is converted into water during an intramolecular water elimination reaction and does not contribute to carbon reduction [97, 98]. As a consequence,  $P-C_4H_8$  is also formed from the water elimination reaction, which explains the similar sooting behavior as *n*-heptane.

Conversely,  $C_3$  species are the largest species formed from methyl butanoate cracking due to the fuel bound oxygen. As pointed out by Westbrook *et al.* [157], the double  $C=O$  bond is very difficult to break, so the carbon chain length is reduced when the  $C-C$  bond is broken due to  $\beta$ -scission. The oxygenated parts are then oxidized to CO and  $CO_2$ , preventing the carbon from entering the pool for soot formation [40, 155]. As shown in Fig. 4.13, fewer allyl radicals are formed from methyl butanoate, such that the concentration of  $C_5H_5$  is also reduced. Since one of the pathways for naphthalene depends quadratically on  $C_5H_5$ , even moderate reductions in the radical concentration will significantly reduce naphthalene. As a result, in methyl butanoate flames, the  $C_5H_5$  recombination pathway is negligible compared to

the C<sub>9</sub>H<sub>7</sub> pathway. This reduction in soot precursors from fuel cracking processes distinguishes methyl butanoate from *n*-heptane and *n*-butanol, in terms of the sooting propensity and CSR.

At this point, the pathways and species that are responsible for soot formation have been identified. The next question that naturally arises is how sensitive these pathways are to the increasing strain rate that leads to reduced soot formation. Although not shown here, sensitivity and reaction path analysis was conducted at critical strain rates, and no substantial differences were found compared with low strain rate cases. In addition, if the CSR is defined based on a relative metric, in other words, to be the strain rate at which the global domain-integrated  $f_V$  is 10% of the value at a fixed low strain rate (16 s<sup>-1</sup>), the three fuels have essentially the same CSR, indicating the potential similarity in the rate-limiting steps of soot formation. These observations indicate that it is mostly the total amount of soot formed with the three fuels that give the differences in CSR.

#### 4.4.3 Rate-Limiting Steps for PAH Formation

To elucidate the rate-limiting step, profiles of soot precursors at low and critical strain rates are shown in Fig. 4.13. All profiles shift in the direction of the liquid pool at higher flow rates as increased strain rates push the stagnation plane towards the pool. Species with ring structures, specifically C<sub>5</sub>H<sub>6</sub> and C<sub>6</sub>H<sub>6</sub> have lower concentrations at CSR, responding to strain similar to  $f_V$ . However, the upstream C<sub>3</sub> precursors, A-C<sub>3</sub>H<sub>5</sub> and C<sub>3</sub>H<sub>3</sub>, have higher concentrations at CSR. Other upstream species such as C<sub>2</sub>H<sub>2</sub> and C<sub>2</sub>H<sub>4</sub> do not show significant difference. This indicates that A-C<sub>3</sub>H<sub>5</sub> and C<sub>3</sub>H<sub>3</sub> species have insufficient residence times to form rings, resulting in the observed

decrease in soot. Therefore, the ring formation reactions



are the rate-limiting steps and are the same for all three fuels.

## 4.5 Summary

In this chapter, the sooting limits of *n*-heptane, *n*-butanol, and methyl butanoate were investigated both experimentally and computationally in the stagnation-flow configuration. Two hypotheses that might explain the lower CSRs of methyl butanoate compared to the other two fuels were proposed: if less soot is produced from methyl butanoate regardless of the strain rate and/or if soot formation reactions of methyl butanoate are more prone to extinction at reduced residence times. The response of soot volume fraction to strain rate, chemical pathways for PAH formation, and the rate-limiting steps were examined to elucidate the relative roles of these two hypotheses. Methyl butanoate is found to be significantly less sooting than *n*-heptane and *n*-butanol at all strain rates. As the three fuels share similar PAH pathways, the fuel specific breakdown processes account for the different  $f_V$  at the same strain rate. Furthermore, the rate-limiting steps for all three fuels were identified and found the same. Therefore, the difference in CSRs for three fuels are due to the total amount of soot formed with the three fuels, due to the difference in fuel breakdown processes that generate soot precursors.

With relatively simple flow configuration, the fuel effects on the PAH chemistry in strained flows were elucidated. The PAH and soot models were further validated with experiments, which was also utilized in the computations of turbulent sooting flames in more complex configurations, presented in the following chapter.

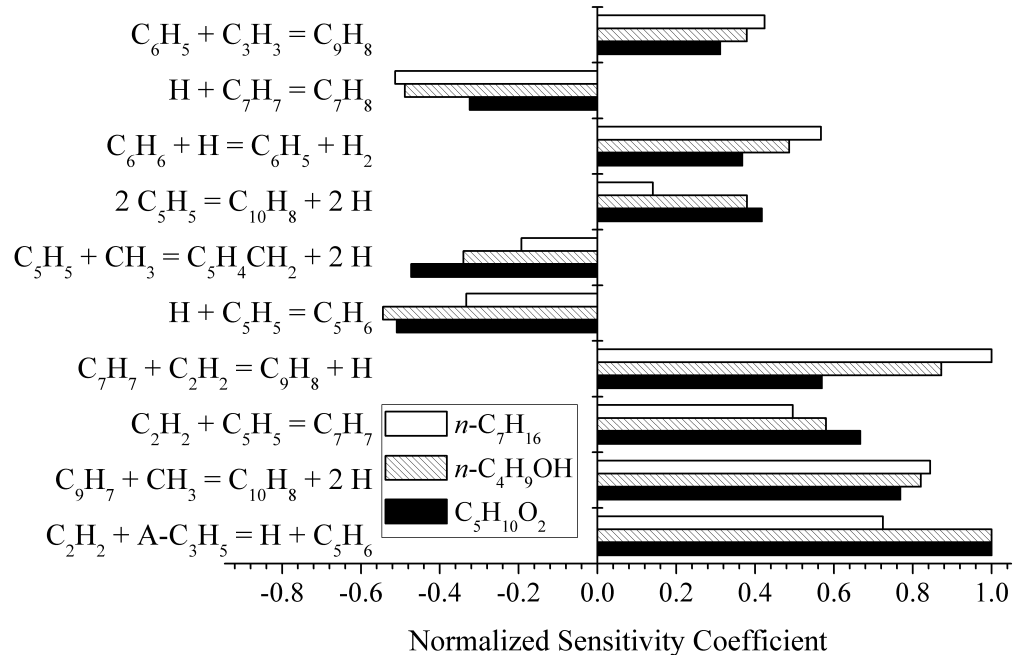
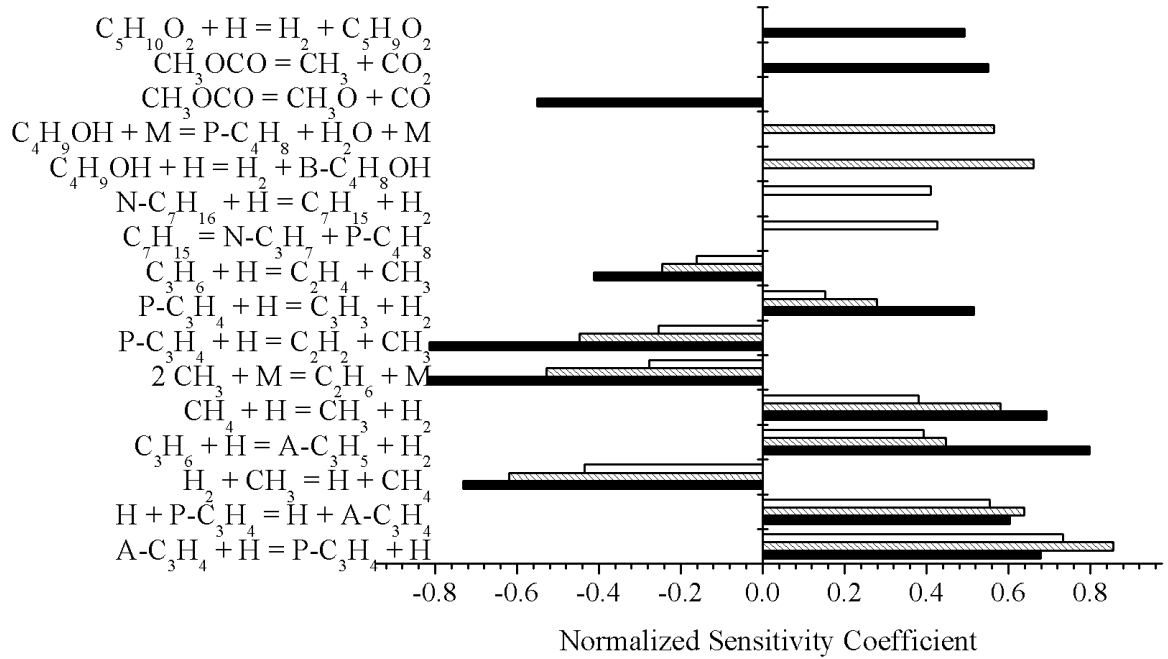


Figure 4.10: Sensitivity of the maximum naphthalene mass fraction to kinetics at the strain rate of  $16 \text{ s}^{-1}$  and  $X_{O_2} = 0.2$ . Top: Intermediate chain radical reactions. Bottom: Ring formation reactions.

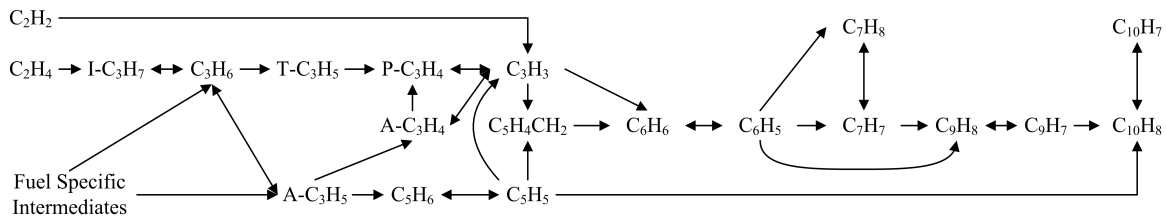


Figure 4.11: Chemical pathways for naphthalene formation at the strain rate of  $16 \text{ s}^{-1}$  and  $X_{O_2} = 0.2$ .

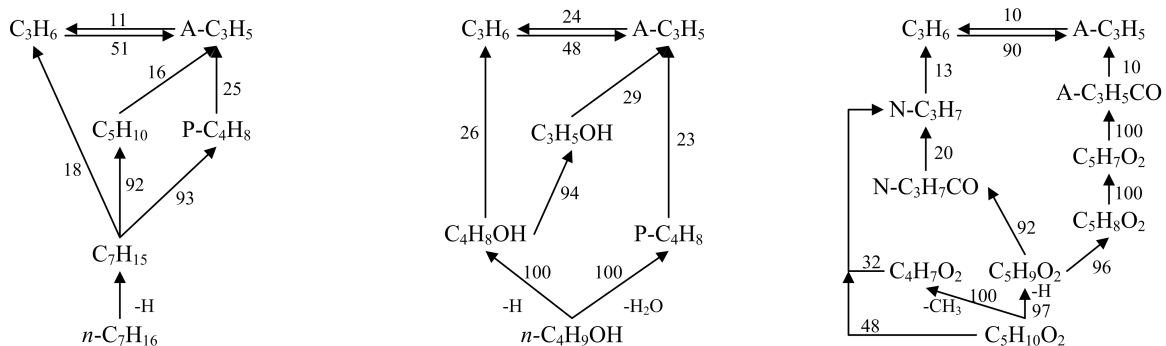


Figure 4.12: Fuel specific pathways for  $\text{C}_3\text{H}_6$  and  $\text{A-C}_3\text{H}_5$  formation at the strain rate of  $16 \text{ s}^{-1}$  and  $X_{O_2} = 0.2$ . From left to right:  $n$ -heptane,  $n$ -butanol, and methyl butanoate. The numbers indicate the relative contribution (in percentages) to the formation of the “downstream” species.

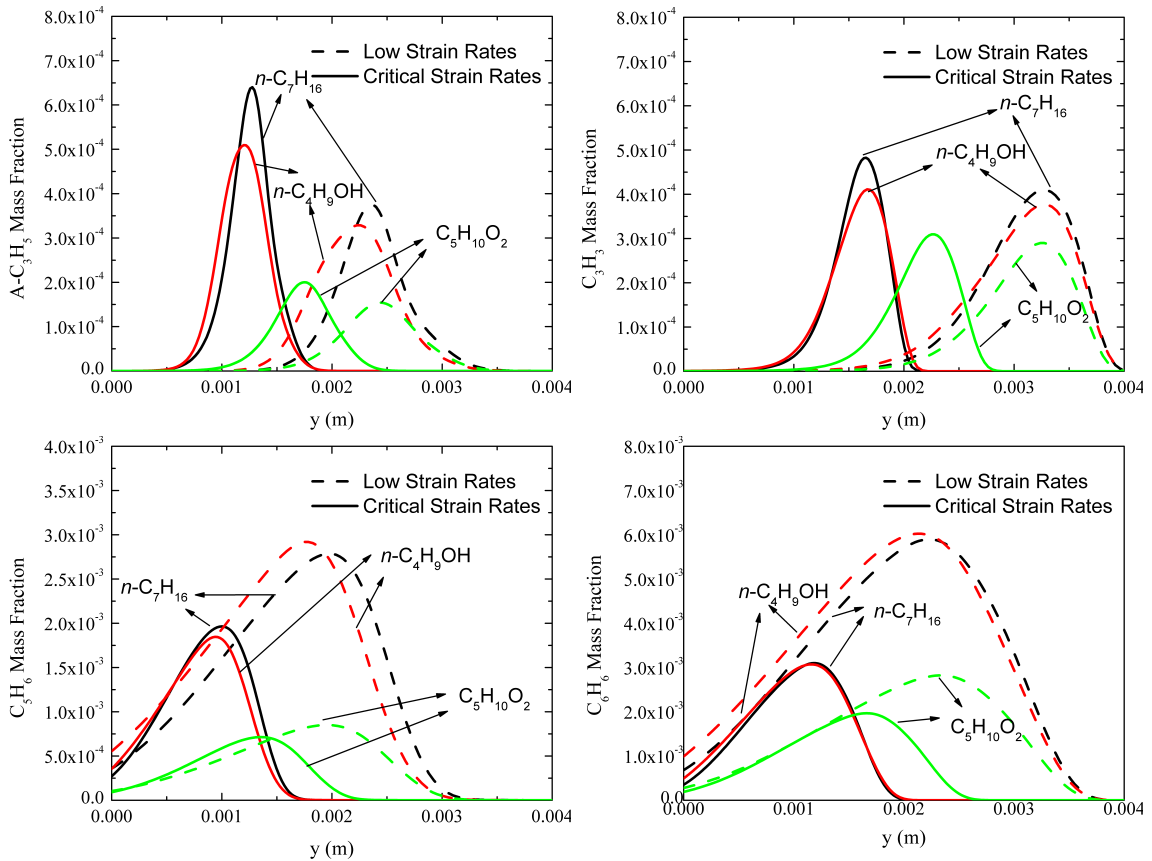


Figure 4.13: Key intermediate species profiles at low strain rates ( $16 \text{ s}^{-1}$ ) and CSRs:  $X_{O_2} = 0.2$ .

# Chapter 5

## Soot Evolution in Turbulent Bluff Body Flames

In practical combustion systems, the flow pattern is often turbulent and complex. To bridge the gap between laminar studies that focuses more on chemical kinetics in sooting flames and real gas turbine studies, in this chapter, a nonpremixed turbulent ethylene/hydrogen sooting flame in a bluff body configuration is presented. Since Mueller *et al.* [107] have experimentally and computationally investigated a turbulent nonpremixed bluff body ethylene flame, the current work that adopts the same experimental system is to elucidate the chemical and hydrodynamic effect of hydrogen addition to the ethylene fuel stream in soot evolution. As reviewed in Chapter 1.2.3, laminar nonpremixed sooting flame studies have shown that hydrogen addition overall suppress soot formation, due to dilution and the change of local C/H ratio. In the current work, however, in addition to this chemical effect, to maintain the same heat release rate and similar Reynolds number as the ethylene bluff body flame [107], a faster central jet is needed, which will change the fuel to coflow air momentum flux ratio and affect the hydrodynamics.

Therefore, the objective of this chapter is threefold: first, to understand the evolution of soot in the hydrogen added ethylene bluff body flame utilizing a combination of experimental and computational results; second, to assess differences between hydrogen added and neat ethylene flames and further validate the LES model; and, third, to differentiate between the hydrodynamic and chemical effects of hydrogen addition.

## 5.1 Experimental Methodology

The collaborative experimental investigation was performed at the University of Adelaide, which is briefly introduced here for completeness. The experimental setup is similar to previous bluff body studies [26, 24] and was kept the same as the previous ethylene case [107]. In brief, the outer diameter of the bluff body ( $D_B$ ) is 50 mm, and the diameter ( $D_J$ ) of the central fuel jet is 3.6 mm, from which an ethylene/hydrogen mixture (2:1 by volume) issued at 102.1 m/s. The heat release rate of the flame was kept the same at 42 kW to maintain similar thermal effects on the flow field. The central jet Reynolds number is 28,400, which is 8% smaller than that of the previous study with a Reynolds number of 30,900 and a jet velocity of 74.2 m/s [107]. The bluff body burner was mounted in a contraction with an exit cross section of 150 by 150 mm<sup>2</sup>, from which air coflow issued at 23 m/s, which is the same as in the previous study.

The 1064 nm beam from an Nd:YAG laser was used for laser-induced incandescence (LII) excitation. The laser sheet had a height of 80 mm through the measurement volume and had a thickness of 0.3 mm. The operating LII fluence was kept at 0.9 J/cm<sup>2</sup> to ensure the independence of the signal to variations in the fluence caused by laser extinction [127, 134]. In addition, data were only extracted from the laser-in side of the measurement to avoid non-linear influences of beam steering [145]. A Gaussian

distribution of the spatial fluence with a 8% standard deviation was achieved. All images presented in this work have been clipped at the edges where the laser sheet was found to exhibit low fluence.

The LII signal was filtered at  $430 \pm 10$  nm and detected with an intensified CCD camera. A short gate width of 40 ns was used to reduce the size-dependent sensitivity of the signal [7]. The LII signal has been calibrated by laser extinction measurements as previously reported [107]. With this system, the in-plane resolution of the images is 0.26 mm/pixel in each direction, and the detection threshold is about 3 ppb.

The data presented in this work have been corrected for background interference and detector attenuation. According to the previous ethylene bluff body study, the estimated measurement uncertainty is about 25%.

## 5.2 Computational Methodology

The modeling of soot-chemistry-turbulence interactions is aided by a statistical soot model, briefly summarized in Sec. 4.2.2, a modified Radiation Flamelet/Progress Variable (RFPV) combustion model for sooting flames, and a presumed subfilter PDF for closure. Complete details of the integrated LES model for sooting turbulent nonpremixed flames can be found in Mueller and Pitsch [109] and the references therein.

In brief, the thermochemical states, such as temperature, species mass fractions ( $Y_k$ ), and other derived quantities, are obtained from tabulated chemistry, described with the RFPV model of Ihme and Pitsch [63] with modifications for soot by Mueller and Pitsch [109]. A detailed analysis of differential diffusion is provided by Dally *et al.* [25] for the same configuration as the current study. In that work, unity Lewis number flamelets were found to reproduce the temperature and stable species more accurately than detailed transport. Therefore, the same unity Lewis number as-

sumption was made in the current study. Solutions of the steady and unsteady (for radiation) flamelet equations are parameterized by the mixture fraction ( $Z$ ), a reaction progress variable ( $C = Y_{\text{CO}_2} + Y_{\text{CO}} + Y_{\text{H}_2\text{O}} + Y_{\text{H}_2}$ ), and a heat loss parameter ( $H$ ) to account for heat losses due to radiation. Due to significant unsteady effects for PAH [6], the mass fractions for these species deviate from their steady values in the flamelet database. Therefore, an additional transport equation for a lumped PAH species is solved, as introduced and discussed in Mueller and Pitsch [109].

The closure for filtered quantities such as density, gas-phase source terms, and soot source terms are achieved with a presumed subfilter PDF model by Mueller and Pitsch [109, 108]. The joint subfilter PDF of the mixture fraction, progress variable, heat loss parameter, and soot moments ( $\tilde{P}(Z, C, H, M_i)$ ) can be modeled by the product of the thermochemical subfilter PDF,  $\tilde{P}(Z, C, H)$ , and the soot subfilter PDF,  $\tilde{P}(M_i)$ , due to the time scale decoupling of the gas-phase and soot evolution [108]. The thermochemical PDF is modeled with a beta distribution for the mixture fraction [20]. Convolution of the flamelet database with the PDF is done *a priori* and tabulated as a function of the filtered mixture fraction, subfilter mixture fraction variance, filtered progress variable, and filtered heat loss parameter. The subfilter mixture fraction variance is obtained from the solution of a transport equation for the filtered square of the mixture fraction with a linear relaxation model [64] for the subfilter scalar dissipation rate. The soot subfilter PDF is modeled with a double delta distribution [108], which requires solving an additional transport equation for the filtered square of the number density.

In summary, the continuity equation, momentum equations, and transport equations for  $\tilde{Z}$ ,  $\tilde{Z}^2$ ,  $\tilde{C}$ ,  $\tilde{H}$ ,  $\tilde{Y}_{\text{PAH}}$ ,  $\overline{M}_{0,0}$ ,  $\overline{M}_{1,0}$ ,  $\overline{M}_{0,1}$ ,  $\overline{N}_0$ , and  $\overline{M_{0,0}^2}$  are solved in the simulation. Specifically, for sooting flames, the filtered transport equations for the mixture fraction, square of the mixture fraction, progress variable, heat loss parameter, lumped PAH mass fraction, soot moments (and weight of the delta function  $N_0$ ),

and square of the number density are given by

$$\frac{\partial \bar{\rho} \tilde{Z}}{\partial t} + \frac{\partial \bar{\rho} \tilde{u}_i \tilde{Z}}{\partial x_i} = \frac{\partial}{\partial x_i} \left( \bar{\rho} \tilde{u}_i \tilde{Z} - \bar{\rho} \tilde{u}_i \widetilde{Z} \right) + \frac{\partial}{\partial x_i} \left( \bar{\rho} \tilde{D}_Z \frac{\partial \tilde{Z}}{\partial x_i} \right) + \bar{m}_Z , \quad (5.1)$$

$$\begin{aligned} \frac{\partial \bar{\rho} \tilde{Z}^2}{\partial t} + \frac{\partial \bar{\rho} \tilde{u}_i \tilde{Z}^2}{\partial x_i} &= \frac{\partial}{\partial x_i} \left( \bar{\rho} \tilde{u}_i \tilde{Z}^2 - \bar{\rho} \tilde{u}_i \widetilde{Z}^2 \right) + \frac{\partial}{\partial x_i} \left( \bar{\rho} \tilde{D}_Z \frac{\partial \tilde{Z}^2}{\partial x_i} \right) \\ &\quad - 2\bar{\rho} \tilde{D}_Z \frac{\partial \tilde{Z}}{\partial x_i} \frac{\partial \tilde{Z}}{\partial x_i} - \bar{\rho} \tilde{\chi}_{\text{sgs}} - \bar{\rho} \tilde{Z}^2 + 2\dot{m}_Z \bar{Z} , \end{aligned} \quad (5.2)$$

$$\frac{\partial \bar{\rho} \tilde{C}}{\partial t} + \frac{\partial \bar{\rho} \tilde{u}_i \tilde{C}}{\partial x_i} = \frac{\partial}{\partial x_i} \left( \bar{\rho} \tilde{u}_i \tilde{C} - \bar{\rho} \tilde{u}_i \widetilde{C} \right) + \frac{\partial}{\partial x_i} \left( \bar{\rho} \tilde{D}_C \frac{\partial \tilde{C}}{\partial x_i} \right) + \overline{\left( \frac{\dot{m}_{\Sigma Y_i^C}}{C^*} \right)} , \quad (5.3)$$

$$\frac{\partial \bar{\rho} \tilde{H}}{\partial t} + \frac{\partial \bar{\rho} \tilde{u}_i \tilde{H}}{\partial x_i} = \frac{\partial}{\partial x_i} \left( \bar{\rho} \tilde{u}_i \tilde{H} - \bar{\rho} \tilde{u}_i \widetilde{H} \right) + \frac{\partial}{\partial x_i} \left( \bar{\rho} \tilde{D}_H \frac{\partial \tilde{H}}{\partial x_i} \right) + \bar{\rho} \bar{H} + \bar{q}_{\text{RAD}} , \quad (5.4)$$

$$\begin{aligned} \frac{\partial \bar{\rho} \tilde{Y}_{\text{PAH}}}{\partial t} + \frac{\partial \bar{\rho} \tilde{u}_i \tilde{Y}_{\text{PAH}}}{\partial x_i} &= \frac{\partial}{\partial x_i} \left( \bar{\rho} \tilde{u}_i \tilde{Y}_{\text{PAH}} - \bar{\rho} \tilde{u}_i \widetilde{Y}_{\text{PAH}} \right) \\ &\quad + \frac{\partial}{\partial x_i} \left( \bar{\rho} \tilde{D}_{\text{PAH}} \frac{\partial \tilde{Y}_{\text{PAH}}}{\partial x_i} \right) + \bar{m}_{\text{PAH}} , \end{aligned} \quad (5.5)$$

$$\frac{\partial \bar{M}_{x,y}}{\partial t} + \frac{\partial \tilde{u}_i^* \bar{M}_{x,y}}{\partial x_i} = \frac{\partial}{\partial x_i} \left( \tilde{u}_i^* \bar{M}_{x,y} - \bar{u}_i^* M_{x,y} \right) + \bar{M}_{x,y} , \quad (5.6)$$

and

$$\frac{\partial \bar{M}_{0,0}^2}{\partial t} + \frac{\partial \tilde{u}_i^* \bar{M}_{0,0}^2}{\partial x_i} = \frac{\partial}{\partial x_i} \left( \tilde{u}_i^* \bar{M}_{0,0}^2 - \bar{u}_i^* M_{0,0}^2 \right) - \bar{M}_{0,0}^2 \frac{\partial \tilde{u}_i^*}{\partial x_i} + 2\overline{M_{0,0} \dot{M}_{0,0}} , \quad (5.7)$$

respectively. Detailed descriptions of these equations can be found in Mueller *et al.* [109]. All of the subfilter stresses and scalar fluxes are closed with dynamic models [50] with Lagrangian averaging [99]. The unfiltered soot source terms are closed with HMOM, and the filtered density, gas-phase source terms, and soot source terms are closed with the presumed subfilter PDF.

The simulation details are similar to the previous ethylene bluff body flame [107]. Flamelet solutions were computed using FlameMaster [121] with the chemical mech-

anism, including PAH, of Pitsch and co-workers [8, 110]. The soot and combustion models were implemented in NGA [29]. The continuity and momentum equations are discretized with a centered, second-order scheme, and the scalar equations are discretized with a bounded QUICK scheme [60]. The computational domain is discretized on a structured, non-uniform grid, with  $384 \times 192 \times 64$  points in the axial, radial, and circumferential directions, respectively. Following from the results of a boundary condition sensitivity study for the neat ethylene case, turbulence intensity in the central jet is increased by 10% compared to the reported experimental condition (fully developed turbulent pipe flow), and a turbulent boundary layer condition is specified for the coflow.

## 5.3 Results and Discussion

### 5.3.1 Overall Flame Structure

The overall structure of the turbulent nonpremixed ethylene/hydrogen bluff body flame is shown and compared with the neat ethylene counterpart in Fig. 5.1. Qualitatively, three distinct regions are identified: a sooting recirculation zone ( $x/D_B < 1.0$ ), a non-sooting, high-strain neck region ( $1.0 < x/D_B < 2.0$ ), and a sooting jet-like region. Quantitatively, the clipped, time-averaged LII images of soot volume fraction are also compared. Soot is formed close to the bluff body, where the residence time is long and turbulence intensity is low. No detectable soot is convected into nor formed in the high-strain neck region. Further downstream in the jet-like region, where the scalar dissipation rate decreases as mixing proceeds, soot formation once again occurs. Since the burner is equivalent and the Reynolds number sufficiently large, the overall flame lengths are similar, but the recirculation zone of the hydrogen added flame appears shorter, based on the soot volume fraction measurements.

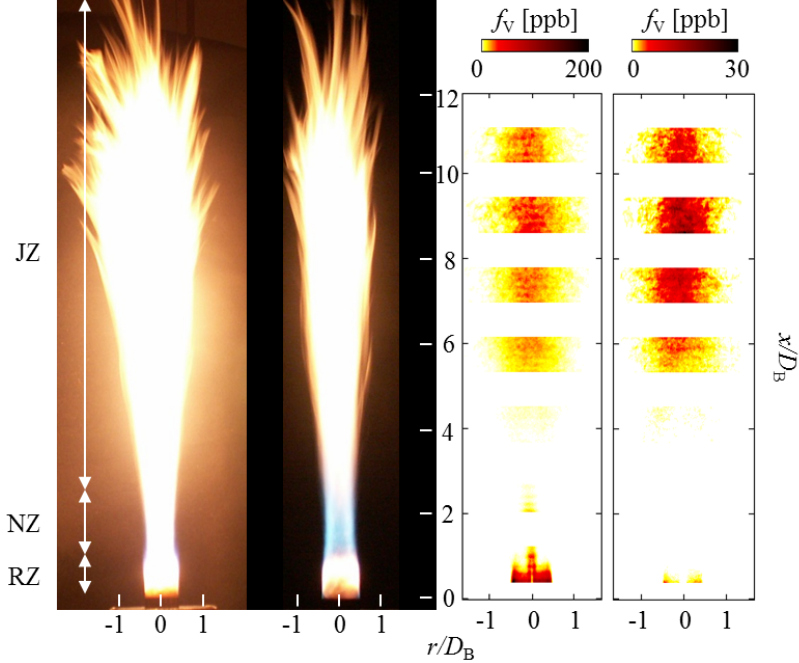


Figure 5.1: Photographs of the neat ethylene (left) and ethylene/hydrogen (right) bluff body flame and the corresponding collages of the time-averaged LII images of the soot volume fraction distribution. Three distinct regions are identified as follows: RZ (recirculation zone), NZ (neck zone), and JZ (jet-like zone).

Although the two flames share similar flow and soot formation patterns, the ethylene/hydrogen flame is significantly less sooting than the neat ethylene flame. As demonstrated in Fig. 5.2, the axial profiles of the radially integrated soot volume fraction ( $\text{ppm}\cdot\text{mm}^2$ ) are compared for the two flames. Two distinct maxima are observed for both flames and correspond to the upstream recirculation zone and downstream jet-like zone. Furthermore, the reduction in the integrated soot volume fraction is more pronounced in the recirculation zone than in the downstream jet-like region. Specifically, according to both Figs. 5.1 and 5.2, the soot reduction in the recirculation zone is more than an order of magnitude, while, in the jet-like zone, the reduction is about a factor of four to six. The difference in the soot reduction with hydrogen addition indicates different dominant soot reduction mechanisms and different roles that hydrogen addition plays in these two regions.

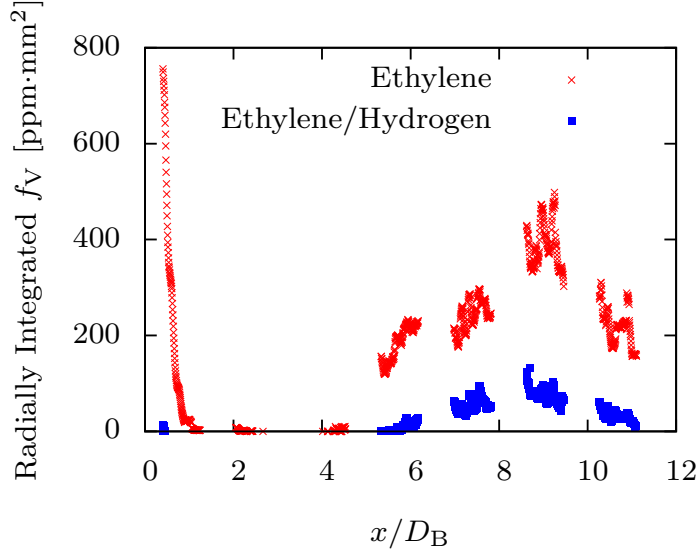


Figure 5.2: Total soot volume per unit height obtained from the radial integration of the time-averaged soot volume fraction from the LII measurements at each height. For clarity, only every second measurement point is shown.

### 5.3.2 Effects of Hydrogen Addition

Two effects of hydrogen addition are potentially relevant: chemical and hydrodynamic effects. Chemically, due to the reduced C/H ratio, PAH formation will be inhibited in the hydrogen added flame, and, therefore, soot formation is inhibited. This chemical effect is an intrinsic property of the fuel mixture, which is less dependent on the specific flow geometry compared to the hydrodynamic effect. Hydrodynamically, since the fuel jet velocity is increased, the fuel jet to air coflow momentum flux ratio is also increased from 10.1 to 13.2. As Dally *et al.* [25] demonstrated, the increase in the fuel jet momentum flux decreases the strength of the mixture in the outer vortex in the recirculation zone, further inhibiting soot formation. The relative significance of these two effects in the two sooting regions of the flames are analyzed in this section.

To first quantify the chemical effect, steady flamelets at a moderate scalar dissipation rate ( $\chi_{st} = 1 \text{ s}^{-1}$ ) were calculated, and the total PAH mass fraction is shown in Fig. 5.3. PAH forms at rich mixture fractions (the stoichiometric mixture fraction for both cases is about 0.06, differing by less than 5%) and peaks at  $Z = 0.2$ . The

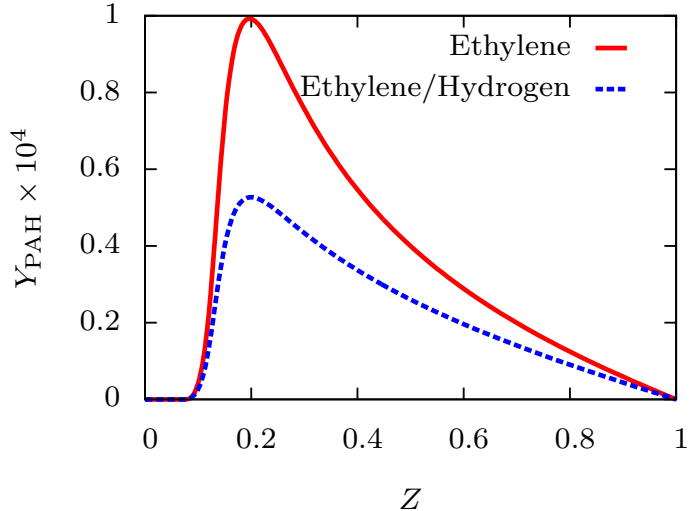


Figure 5.3: PAH mass fraction profiles calculated with steady flamelets at  $\chi = 1 \text{ s}^{-1}$ .

maximum  $Y_{\text{PAH}}$  decreases by a factor of two with hydrogen addition. The scalar dissipation rate of  $1 \text{ s}^{-1}$  was chosen because the representative value in the flame is of this order; however, the quantitative trend is not very sensitive to this choice. At higher scalar dissipation rates, such as  $10 \text{ s}^{-1}$ , PAH reduction with hydrogen addition is approximately the same, about a factor of 2.5. At lower scalar dissipation rates, PAH shows substantial departure from the steady flamelet model [6], so such scaling would not be expected to apply. In the soot model adopted in the LES, PAH-based soot formation and growth, which has been shown to dominate in turbulent jet flames [6, 1, 2, 109, 107], scales as the square of the PAH mass fraction. Therefore, this chemical effect is expected to result in a reduction of soot volume fraction by a factor of four in the jet-like region. This reduction is consistent with the experimental measurements, suggesting that chemical effects are primarily responsible for soot suppression in the downstream jet-like region.

Conversely, noting that the chemical effect predicted by the steady flamelet solution is less than the total soot reduction in the recirculation zone, soot evolution in this region is further analyzed with LES. Radial profiles of the time-averaged soot

volume fraction are shown in Fig. 5.4 for both cases and at two axial locations in the recirculation zone. Qualitatively, two distinct sooting peaks are found in the radial profiles. Mueller *et al.* [107] found in the ethylene bluff body flame that the inner and outer peak corresponds to the PAH-based growth and acetylene-based surface growth pathway, respectively. Quantitatively, the calculated soot volume fraction of the ethylene case is slightly underpredicted but within experimental uncertainty [107]. For the hydrogen added case, the calculated soot volume fraction appears to be overpredicted. However, the mean soot volume fraction from the LES is only slightly higher than the experimental detection limit of 3 ppb. Therefore, the soot volume fraction measured with LII may be low by as much as 3 ppb, which easily accounts for the discrepancy between the measurements and LES. An additional explanation could be that the recirculation zone is slightly too rich in the LES compared to the experiment, for which experimental diagnostics are only recently available [12] and have not been applied to this flame.

Hydrogen addition not only induces chemical effects through modification of the fuel stream C/H ratio but also hydrodynamically influences mixing, that is, the local mixture fraction, as well as residence time in the recirculation zone. The residence time effect is first estimated by comparing the streamline patterns in the recirculation zone of the two flames, as shown in Fig. 5.5. In both flames, the circulation vortex appears as single vortex near the outer shear layer between the air coflow and the recirculation zone due to sufficiently large jet/coflow momentum flux ratio [24, 25]. The location and structure of these two vortices are almost identical. Estimating residence time [26] by dividing the length of the recirculation zone by the coflow velocity (identical between these flames), it is found that residence time in the recirculation zone is similar between these two flames. Therefore, differences in residence time plays little role in dictating the difference in soot volume fraction in the recirculation

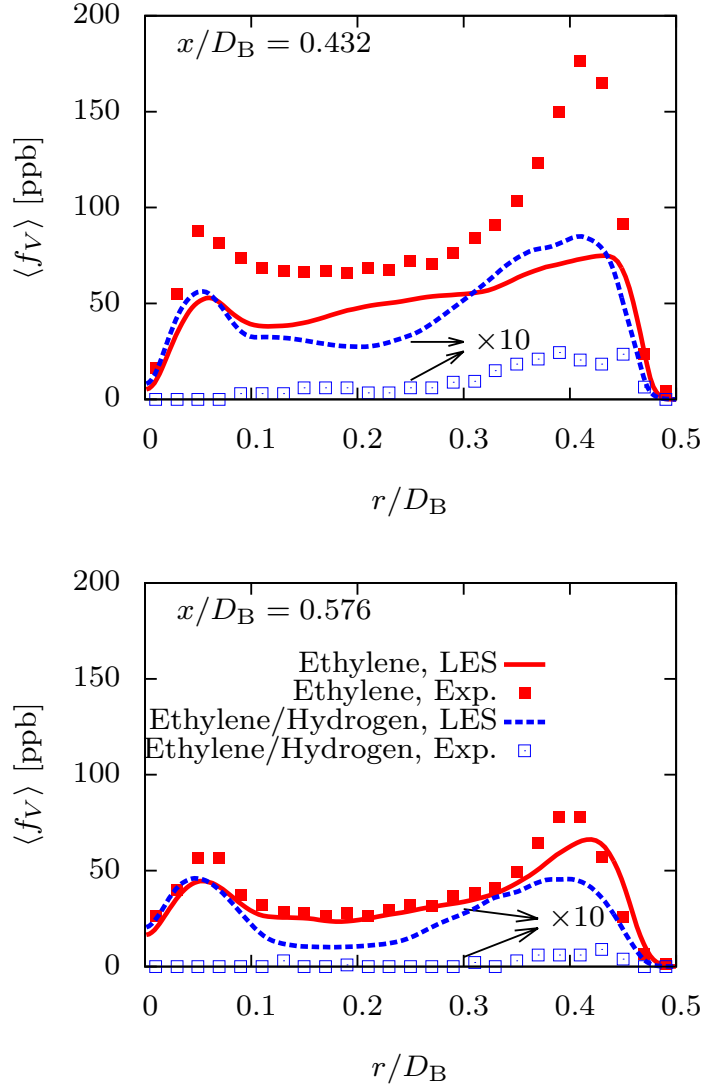


Figure 5.4: Radial profiles of the time-averaged soot volume fraction. Only every fourth experimental measurement point is shown for clarity. The ethylene flame is reproduced from [107], and the ethylene/hydrogen flame is from this work. Both experimental and computational results for the ethylene/hydrogen flame are scaled up by a factor of ten.

zone in the two flames, and the difference beyond the chemical effects must be a result of different degrees of mixing in the recirculation zone.

The recirculating motion of the outer vortex transports rich mixture fraction from the fuel jet to the recirculation zone. As discussed above, the increase of the fuel/coflow momentum flux ratio (about 30%) inhibits such transport, resulting in a

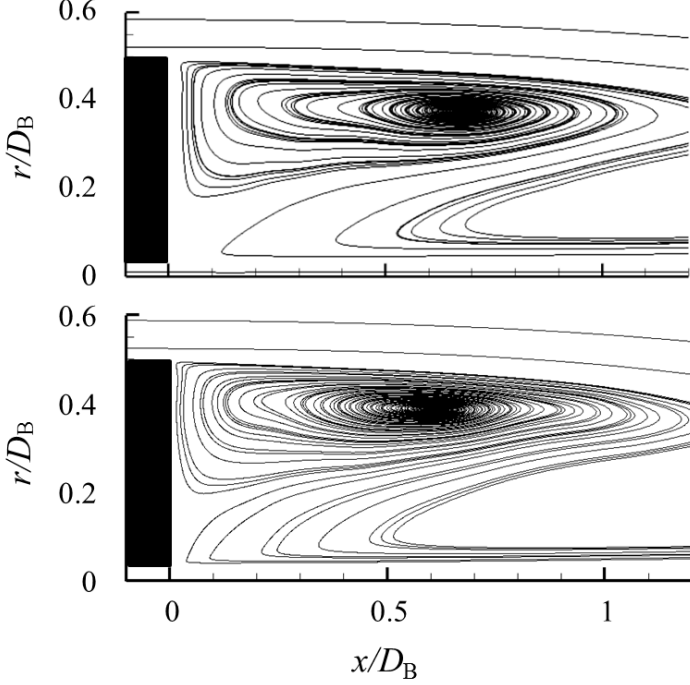


Figure 5.5: Streamlines in the recirculation zone of the neat ethylene flame (top) and ethylene/hydrogen flame (bottom) in the LES.

leaner recirculation zone than the neat ethylene case (recall that the stoichiometric mixture fraction is essentially the same for the two mixtures). The mixture fraction radial profiles from LES as well as the characteristic time scales of the soot formation and oxidation processes from a lightly strained ( $\chi_{\text{st}} = 1 \text{ s}^{-1}$ ) steady flamelet solution are shown in Fig. 5.6. The characteristic time scales of the acetylene-based growth and oxidation processes remain the same, while that of the PAH-based growth slows down due to reduced PAH concentration as discussed previously. Additionally, as expected, the mixture fraction profile near the bluff body surface is affected substantially by hydrogen addition. As shown in Fig. 5.6, in the recirculation zone, the mean mixture fraction decreases by 25% with hydrogen addition. Consequently, the mixture fraction shifts from where PAH-based growth is favored ( $Z \sim 0.18$ ) to where oxidation becomes nearly as fast as acetylene-based surface growth ( $Z \sim 0.11$ ), suppressing soot formation and growth. Note that soot formation and oxidation are also sensitive to temperature, which is influenced by mixture fraction, gas-phase radiation,

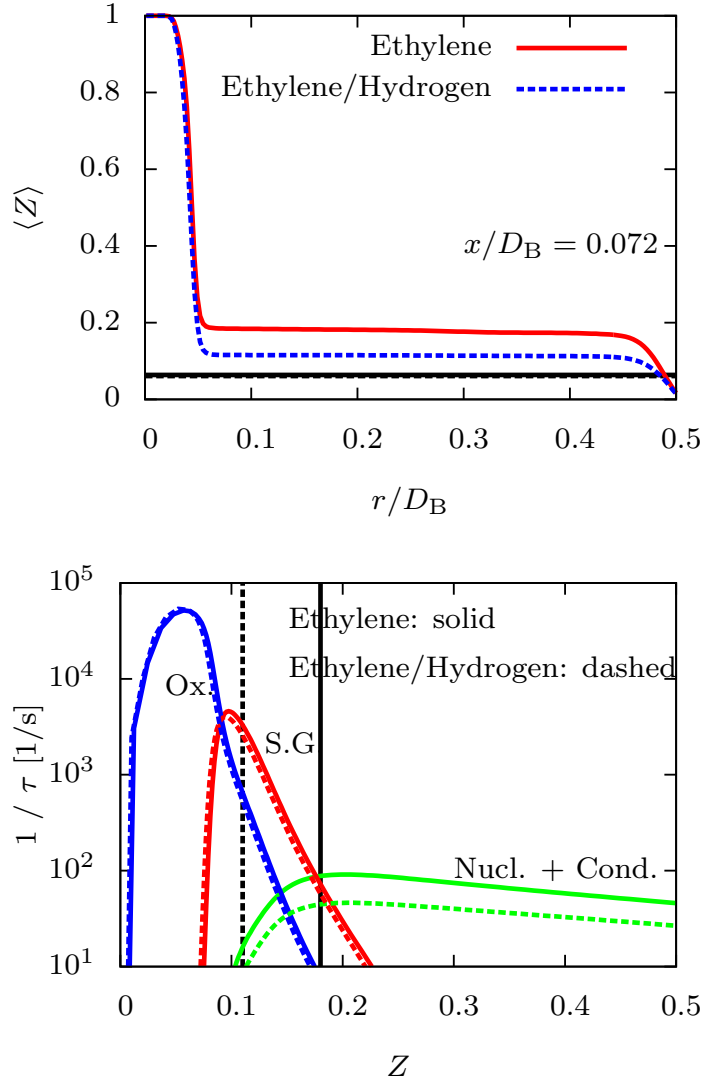


Figure 5.6: Top: radial profile of the time-averaged mixture fraction in the LES at different heights. Black horizontal lines correspond to the stoichiometric mixture fractions of these two flames and almost overlap. Bottom: characteristic inverse time scales of the soot processes from the steady flamelet calculations at  $\chi_{st} = 1 \text{ s}^{-1}$ . Vertical lines correspond to the mixture fraction in the flat regions of the radial plot.

and soot radiation. Due to the relatively low soot loading (ppb), soot radiation is negligible compared to gas-phase radiation, which depends on mixture fraction as well as residence time (same in both flames). Therefore, the leaning in the recirculation zone due to hydrodynamic effects account for the further inhibited soot formation in addition to the chemical effect.

The PAH-based, acetylene-based, and oxidation source terms are shown in Fig. 5.7 to elucidate the evolution of soot. Soot nucleation mainly occurs near the inner shear layer between the fuel jet and recirculation zone where mixture fraction is high. Some of this soot is entrained by the recirculation zone and transported back upstream toward the bluff body then radially outward toward the outer shear layer by the recirculation vortex. This trend is consistent with the neat ethylene case [107]. In the neat ethylene flame, acetylene-based surface growth becomes dominant in the outer shear layer close to the stoichiometric mixture fraction contour, and oxidation is almost negligible except close to the downstream neck zone. However, due to the lean shift of the mean mixture fraction near the bluff body in the hydrogen added flame, oxidation becomes comparable to the acetylene-based growth. Consequently, soot nucleation in the recirculation zone of the hydrogen added flame is first suppressed due to reduced PAH concentration, and soot surface growth competes with soot oxidation, resulting in a less sooting recirculation zone than the neat ethylene flame.

## 5.4 Summary

In this chapter, the effects of hydrogen addition on soot evolution in a nonpremixed bluff body configuration were studied experimentally and computationally and compared with the neat ethylene counterpart. The PAH and soot models are the same as in the laminar study presented in Chapter 4, however, turbulence-chemistry interactions show coupling effects on soot evolution, which can be differentiated and quantified as chemical effects and hydrodynamic effects. While the chemical effects can be estimated with lower-dimensional laminar flamelets, the hydrodynamic effects need to be revealed with three-dimensional high-fidelity modeling with the integrated LES model for sooting flames.

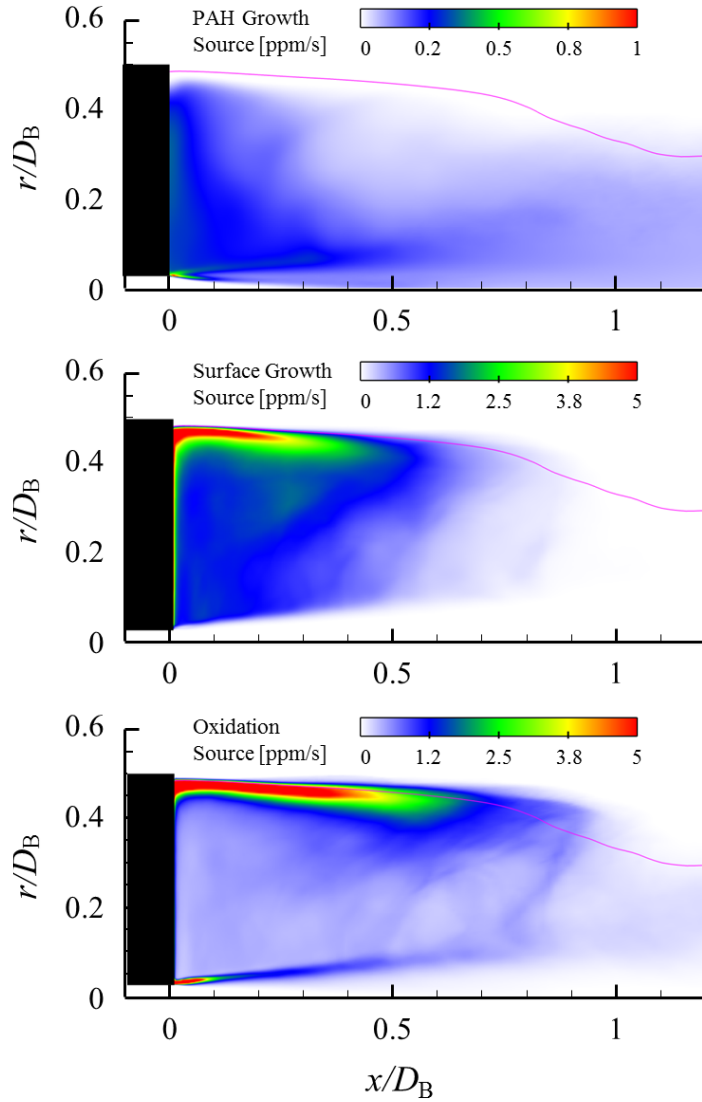


Figure 5.7: Time-averaged soot volume fraction source term [ppm/s] in the recirculation zone of the ethylene/hydrogen flame in the LES. The magenta lines correspond to the stoichiometric mixture fraction contours.

In the jet-like region of the bluff body flame, the chemical effect due to reduced C/H ratio is dominant in soot reduction. However, in the recirculation zone of the bluff body flame, hydrogen addition not only reduces the formation of PAH but also results in leaner mixture fraction. Consequently, soot formation is inhibited while oxidation is promoted, resulting in a significantly less sooting recirculation zone compared to a neat ethylene case. Comparison between experimental and computational

results further validate the integrated LES and demonstrate the necessity of adopting high-fidelity chemical, soot, and turbulent models to reasonably predict turbulent sooting flames in complex flow configurations.

# Chapter 6

## Conclusions

This dissertation represents several advancements in the understanding of the chemistry-transport coupling in flame dynamics and emissions. In particular, two core topics are mainly focused on: flame stabilization and soot evolution in reacting flows at engine relevant conditions. To unravel the coupling effects of chemical kinetics and flow dynamics, for both topics, foundational studies on chemical kinetics are first conducted in relatively simple, one-dimensional, laminar counterflow or stagnation-flow configurations, facilitated with the combination of experiments and computations. Complexities from the flow conditions are gradually brought in to elucidate the interactions between chemistry and transport at elevated temperatures and pressures or turbulent conditions. Major contributions from this dissertation are summarized below.

### 6.1 Major Contributions

#### 6.1.1 Characterization of Nonpremixed Cool Flames

In Chapter 2, experimental substantiation was acquired for the computationally predicted existence of low-temperature, NTC-affected, weakly burning nonpremixed

flames in the counterflow configuration. In particular, the filtered PMT imaging demonstrated the presence of the signature CH<sub>2</sub>O chemiluminescence in the counterflowing heated air stream against nitrogen-diluted DME, while sensitive infrared imaging determined the corresponding ignition temperature. Extensive experimentation then demonstrated that the low-temperature reactivity was enhanced with increasing air temperature, decreasing strain rate of the flow, and was insensitive to the DME concentration in the fuel stream. Accompanying computations substantiated the experimental results, and further corroborated the essential NTC chemistry governing the observed phenomena.

Furthermore, for the first time, the hysteretic ignition and extinction behavior of the nonpremixed cool flame was experimentally observed and quantified at elevated pressures. Results further show that, although low-temperature chemistry is crucial for the initiation and sustain of the cool flame, the dominant chemical pathways shift from reactions responsible for low-temperature radical runaway to cool flame heat release reactions upon ignition. The heat release from the cool flame is able to sustain itself at lower oxidizer boundary temperature and, therefore, results in the hysteresis temperature window between ignition and extinction.

Increasing ambient pressure and/or oxygen concentration in the oxidizer stream promotes the heat release from low-temperature chemistry and extends the hysteresis between ignition and extinction. Although the influences on the cool flame ignition temperature were well predicted by computation, the influences on extinction were significantly overpredicted. Possible reasons for such discrepancies were discussed, including the uncertainties from experiments and chemical models. The need for improved comprehensiveness of the chemical kinetics model is emphasized.

### 6.1.2 Demonstration of Autoignition-Affected Flame Dynamics

In Chapter 3, computations of two-dimensional nonpremixed DME flames in heated air coflows were presented. The computations were conducted at 30 atmospheres to observe the influence of NTC chemistry on the stabilization mechanism. The stabilization of steady flames was first studied, and the effects of boundary temperature and velocity were investigated.

The heat release rate profile and characteristic species profiles for low- and high-temperature chemistry, autoignition, and partially premixed flame propagation were examined. Further investigation based on Chemical Explosive Mode Analysis and Lagrangian Flamelet Analysis enabled the determination of the evolution of the controlling chemical pathways and the stabilization mechanism.

For fixed fuel and coflow velocities of 3.2 m/s and varying boundary temperatures, the 700 K case was characterized as *kinetically* stabilized, for, neglecting the diffusion processes along mixture fraction iso-contours, the one-dimensional LFA agrees with the two-dimensional CFD responses. As the boundary temperature increases, the leading point of the heat release profile shifts to richer mixture fractions and then shifts back due to the NTC effect on the autoignition process and the coupling between autoignition and premixed flame propagation chemistry. Stabilization is also affected by both inhomogeneous autoignition and premixed flame propagation, as in the 800 and 900 K cases. The 1100 K case was characterized as *kinematically* stabilized, for it exhibits the classical triple flame structure, with stabilization achieved due to the balance between the premixed flame propagation velocity and the local incoming flow velocity.

For fixed boundary temperature of 900 K and varying fuel and coflow velocities, at 2.4 m/s, the lifted flame appears to be the classical triple flame stabilized by the balance between the local flame speed and incoming flow velocity, and it is

therefore characterized as *kinematically* stabilized. As the inlet velocity increases, such a balance cannot be achieved at certain mixture fractions. Instead, inhomogeneous autoignition becomes the dominant combustion mode. As a consequence, the multibrachial structure is stabilized by both premixed flame propagation and inhomogeneous autoignition and is characterized as multimode stabilized. At 8.0 m/s, the *kinematic* balance cannot be achieved anywhere in the flow field due to lack of back diffusion. A *kinetically* stabilized inhomogeneous autoignition front is formed where diffusion processes along the mixture fraction iso-contours are negligible compared to the gradient direction. In the *kinetically* stabilized autoignition front, NTC chemistry plays an important role, dictating the stabilization point. This point occurs at the mixture fraction with the shortest ignition delay time, which is a compromise of the first stage autoignition delay time and heat release from low temperature chemistry. Conversely, the *kinematically* stabilized flames are less affected by NTC chemistry, with only a minor effect on the local flame speed resulting from the upstream accumulation of heat and radicals.

An extended two-dimensional stabilization regime diagram was constructed, considering both transport (inlet velocity) and chemical (coflow boundary temperature) effects. The stabilization regime diagram includes frozen flow, kinetically stabilized, autoignition-propagation-coupled stabilized, kinematically stabilized, and burner stabilized regimes. At high coflow boundary temperatures or low inlet velocities, the classical tribrachial flame structure is achieved, and autoignition contributes less to the stabilization due to reduced heat and radical accumulation. The kinematic balance between the local flow speed and flame propagation speed is the dominant stabilization mechanism. On the contrary, kinetic stabilization is achieved at lower coflow temperatures or higher inlet velocities as autoignition becomes dominant. Due to the transition of the dominant chemical pathways during autoignition, the kinetically stabilized structure is usually multibrachial.

The unsteady effects on flame dynamics in oscillating flows were then investigated with the comparisons with the steady cases. The inlet velocity oscillates between 2.4 and 8.0 m/s at 25, 50, and 100 Hz. Flame dynamics in such oscillating flows and frequency effects on the hydrodynamics-chemistry coupling were analyzed.

The heat release rate profiles were examined to describe the thermal structure. The morphology of the thermal structure transitions between tribrachial and multibrachial. The multibrachial structure is favored when the inlet velocity is higher, although there is hysteresis during the transition. Such structures agree well with the steady cases, which correspond to different combustion modes: tribrachial flame and autoignition. Normalized displacement velocity was defined to differentiate these two modes in the current study and compare with the steady cases.

According to the steady results, the normalized displacement velocity for a tribrachial flame is around unity and is larger for autoignition. The same criterion was applied to the unsteady cases to elucidate the evolution of combustion mode. As the inlet velocity decreases, autoignition is the dominant combustion process until flame chemistry takes over around the most upstream location and slowest inlet velocity. The tribrachial flame is convected downstream as the flow velocity increases. The radical and heat accumulation upstream of the tribrachial flame finally results in autoignition, showing a sudden increase in the normalized displacement velocity.

Oscillation frequency effects on the hydrodynamics-chemistry coupling were analyzed by examining the profiles of temperature, methyoxy methylperoxy radical, and hydrogen peroxide during the oscillation process. It is found that, at the three frequencies investigated, the tribrachial structure does not have sufficient time to reach steady state, and the transition from tribrachial flame to a multibrachial autoignition front occurs over a finite induction time as velocity increases. Consequently, the decreasing-velocity and increasing-velocity cycles have different normalized displacement velocities and hence demonstrate hysteresis. At lower frequencies, such

hysteresis is less pronounced, for longer relaxation time is allowed to approach the quasi-steady state condition.

NTC chemistry represented by methyoxy methylperoxy radical accumulation and depletion has shorter time scale and therefore is able to respond to the hydrodynamic changes. However, autoignition and flame establishment have comparable time scales to the oscillation period and are therefore coupled with the flow dynamics. At lower oscillation frequencies, chemical kinetics is closer to reaching the two steady-state conditions with the maximum and minimum boundary velocities.

### 6.1.3 Characterization of Nonpremixed Sooting Limits

In Chapter 4, *n*-heptane, *n*-butanol, and methyl butanoate were chosen as diesel, bioalcohol, and biodiesel surrogates of interest due to their similar volatilities and consequent potential applications in diesel fuel blending. Their sooting limits were measured experimentally with the stagnation-flow apparatus. Computations were conducted for the same configuration using detailed PAH chemistry and a detailed soot model based on the Hybrid Method of Moments (HMOM). Argon dilution was adopted to keep the thermal environment for the three fuel cases essentially the same in order to elucidate the chemical effects. Both experimental and computational results show the critical strain rates of the three fuels, based on the absolute soot volume fraction, increase with increasing oxygen mole fraction in the oxidizer due to the thermal effect. Moreover, although *n*-heptane and *n*-butanol show similar sooting propensities, methyl butanoate produces significantly less soot.

Sensitivity and reaction path analysis was performed for naphthalene, the first PAH species from which soot forms. This analysis revealed that, despite different sooting tendencies, the three fuels shared similar PAH chemical pathways. C<sub>5</sub>, C<sub>6</sub>, C<sub>7</sub> and C<sub>9</sub> rings as well as naphthalene are formed sequentially through the combination of C<sub>3</sub> and smaller chain radicals resulting from fuel cracking processes. Due to the

fuel bound oxygen in methyl butanoate, less and shorter chain radicals are available for soot formation, compared with the other fuels, such that methyl butanoate forms the least soot and has the lowest critical strain rates.

The strain rate effects on soot formation were also examined. Despite different sooting propensities, for all three fuels, C<sub>5</sub> and C<sub>6</sub> ring formation reactions are the rate-limiting steps. Their concentrations drop as the residence time is reduced, such that the downstream PAH chemistry is consequently inhibited, resulting in the sooting limits.

#### **6.1.4 Demonstration of Hydrogen-Affected Soot Emissions**

In Chapter 5, a sooting turbulent bluff body stabilized ethylene/hydrogen flame was studied both experimentally and computationally and compared with a previously analyzed neat ethylene counterpart [107]. Laser-induced incandescence (LII) measurement of soot volume fraction was conducted at the University of Adelaide. An integrated Large Eddy Simulation (LES) model was adopted to elucidate the interactions between soot, turbulence, and chemistry. The statistical soot model was based on the Hybrid Method of Moments (HMOM), considering detailed nucleation, condensation, particle collision, surface growth, oxidation, and fragmentation processes that influence soot evolution. The combustion model for the gas-phase was based on the Radiation Flamelet/Progress Variable (RFPV) model with modifications to account for the removal of Polycyclic Aromatic Hydrocarbon (PAH) from the gas-phase. A presumed PDF was utilized to model unresolved subfilter scale interactions.

Similar to the neat ethylene bluff body flame, three distinct flow regions were observed experimentally: a sooting recirculation zone, a non-sooting, high-strain neck region, and a sooting jet-like zone. Although the ethylene/hydrogen case is significantly less sooting than the neat ethylene counterpart overall, soot reduction in the recirculation zone near the bluff body is more pronounced than in the downstream

jet-like region. Both chemical and hydrodynamic effects were identified as reasons for this decrease.

The chemical effect was first quantified from a steady flamelet calculation. Due to the hydrogen addition, PAH mass fraction was found to decrease by a factor of two, indicating a factor of four decrease in the PAH-based growth rate that includes both nucleation and PAH condensation. This is consistent with the soot reduction in the downstream jet-like region, where PAH-based growth is dominant. Therefore, the chemical effect is dominant in this region.

The hydrodynamic effect was then analyzed, since both the experimental measurements and LES calculations demonstrated additional soot reduction in the recirculation zone, which could not be explained with the chemical effect alone. The streamline patterns in the recirculation zone of the two flames are similar according to LES, and therefore, differences in residence time plays little role in the difference in soot volume fraction in the recirculation zone.

Conversely, in the experiment, to attain the same heat release rate and similar Reynolds number in the hydrogen added flame as the neat ethylene flame, the central jet velocity was increased. This increase in the fuel to air coflow momentum flux ratio entrains less fuel into the recirculation zone near the bluff body surface, compared to the neat ethylene flame. Due to the leaner mixture fraction in the recirculation zone, soot nucleation and surface growth is inhibited and soot oxidation is promoted. This hydrodynamic effect together with the chemical effect accounts for the soot reduction in the recirculation zone.

## 6.2 Recommendations for Future Work

While this dissertation has advanced the understanding of the coupling effects of chemistry and transport in flame dynamics and soot emissions, the understanding

itself has in turn generated a plethora of interesting and relevant questions, the resolution of which would further extend the frontier of combustion science. With due modesty, the author of this dissertation presents in the following some of these challenging questions in the hope of stimulating further research leading to closure.

- **Foundational Studies on Cool Flames:** As demonstrated in Chapter 2, the nonpremixed cool flame has distinctive states of ignition and extinction. In a previous study by Zhao *et al.* [168], the laminar propagation speeds of premixed cool flames were measured in a counterflow configuration. It is quite clear that, just like the traditional hot flame, the cool flame is a new type of flame that can also propagate and has limiting phenomena. Consequently, other foundational studies on cool flames, such as flammability limits and flame instabilities, should be pursued. Such studies will not be trivial, mainly due to two reasons: limited experimental data and less accurate chemical models. As demonstrated in Chapter 2, the experimental detection of cool flames is already very challenging, which also limits the development of low-temperature chemical models. Much effort is needed in the quantification of low-temperature species in cool flames and providing validation targets for chemical model development.
- **Flame Dynamics in Turbulent Flows:** Although Chapter 3 represents a useful contribution to the understanding of nonpremixed flames at autoignitive conditions, practical engines conditions are turbulent. In such flows, the unsteady motion of eddies and enhanced temperature and species dissipation can strongly influence stabilization. Therefore, further investigation is required to understand the role of turbulence in the stabilization of such flames and determine whether the stabilization mechanism is modified. In terms of computational study, direct numerical simulation (DNS) for turbulent reacting flows at elevated pressures will be computationally expensive. Therefore, large eddy simulation (LES) is a reasonable choice. The combustion model in LES will

then need to be able to capture the multi-modal combustion characteristics, as demonstrated in Chapter 3. In terms of experimental study, high pressure experiments are needed to provide potential experimental substantiation of these predicted multibrachial structures in laminar flows. However, maintaining laminar air coflows at elevated temperatures and pressures and with large flow rates is also very challenging. Moving on to turbulent studies, experimental techniques that can characterize different combustion modes need to be developed, such as iso-surface-tracking, which can be utilized to quantify the propagation speed of the reacting front and compared to the displacement velocity in computations. To capture the low-temperature reactivity, online characterization of the low-temperature species such as formaldehyde would be helpful, however, it will be challenging to differentiate between the low-temperature and high-temperature chemistry, for formaldehyde is also an important intermediate species during high-temperature oxidation processes.

- **Validation and Development of Soot Models:** As the regulation on soot emission has become very stringent, accurate soot prediction for practical combustion devices is needed. To achieve this goal, two main issues need to be solved. First, soot and gas-phase measurements are needed for chemical and combustion model development. Since soot particles have strong black body effects, laser measurements of gaseous species are typically not available in high-loading sooting flames. Especially in turbulent sooting flames, simultaneous measurements of soot, velocity, and other scalars are very rare. Second, the development of soot models should be further advanced. As discussed in Chapter 4, well controlled laminar experiments can provide useful validation targets for soot model development. Having sufficient confidence in the PAH and soot models, turbulent flames with low soot loading could be pursued, where optical access to scalar and velocity measurements allow the investigation of the

turbulence-chemistry interactions, which will be beneficial for LES model development. Furthermore, since soot particles are strong radiators in the flame, radiative heat transfer between soot and the ambient gas needs to be quantified using more accurate models than the optically thin model for some conditions. Coupling the radiation model with the current combustion and soot models can be challenging. Again, low soot loading laminar flames with well-characterized flow and temperature fields can initiate the investigation, and complexities from large hydrocarbon fuels, flow configuration, and turbulence can be brought in gradually.

# Bibliography

- [1] A. Attili, F. Bisetti, M. E. Mueller, and H. Pitsch. Formation, growth, and transport of soot in a three-dimensional turbulent non-premixed jet flame. *Combust. Flame*, 161:1849–1865, 2014.
- [2] A. Attili, F. Bisetti, M. E. Mueller, and H. Pitsch. Damköhler number effects on soot formation and growth in turbulent nonpremixed flames. *Proc. Combust. Inst.*, 35:1215–1223, 2015.
- [3] R. L. Axelbaum and C. K. Law. Soot formation and inert addition in diffusion flames. *Proc. Combust. Inst.*, 23:1517–1523, 1991.
- [4] P. Berta, S. K. Aggarwal, and I. K. Puri. An experimental and numerical investigation of *n*-heptane/air counterflow partially premixed flames and emission of NO<sub>x</sub> and PAH species. *Combust. Flame*, 145:740–764, 2006.
- [5] A. Bhagatwala, Z. Luo, H. Shen, J. A. Sutton, T. Lu, and J. H. Chen. Numerical and experimental investigation of turbulent DME jet flames. *Proc. Combust. Inst.*, 35:1157–1166, 2015.
- [6] F. Bisetti, G. Blanquart, M. E. Mueller, and H. Pitsch. On the formation and early evolution of soot in turbulent nonpremixed flames. *Combust. Flame*, 159:317–335, 2012.
- [7] H. Bladh and P. E. Johnsson, J. Bengtsson. On the dependence of the laser-induced incandescence (LII) signal on soot volume fraction for variations in particle size. *Appl. Phys. B*, 90:109–125, 2008.
- [8] G. Blanquart, P. Pepiot, and H. Pitsch. Chemical mechanism for high temperature combustion of engine relevant fuels with emphasis on soot precursors. *Combust. Flame*, 156:588–607, 2009.
- [9] G. Blanquart and Heinz Pitsch. A joint volume-surface-hydrogen multi-variate model for soot formation. In H. Bockhorn, A. D’Anna, A. Sarofim, and H. Wang, editors, *Combustion Generated Fine Carbonaceous Particles*, pages 439–466. KIT Scientific Publishing, 2009.
- [10] J. Buckmaster. Edge-flames. *Prog. Energy Combust. Sci.*, 28:435–475, 2002.

- [11] M. Bui-Pham and K. Seshadri. Comparison between experimental measurements and numerical calculations of the structure of heptane-air diffusion flames. *Combust. Sci. Technol.*, 79:293–310, 1991.
- [12] O. R. H. Buxton, R. A. Burns, and N. T. Clemens. Simultaneous krypton PLIF, LII and PIV measurements in a sooting jet flame. *51st AIAA Aerospace Sciences Meeting*, pages 2013–0479, 2013.
- [13] J. Camacho, S. Lieb, and H. Wang. Evolution of size distribution of nascent soot in *n*- and *i*-butanol flames. *Proc. Combust. Inst.*, 34:1853–1860, 2013.
- [14] B. C. Choi and S. H. Chung. Autoignited laminar lifted flames of methane, ethylene, ethane, and *n*-butane jets in coflow air with elevated temperature. *Combust. Flame*, 157(12):2348–2356, 2010.
- [15] B. C. Choi and S. H. Chung. Autoignited laminar lifted flames of methane/hydrogen mixtures in heated coflow air. *Combust. Flame*, 159(4):1481–1488, 2012.
- [16] B. C. Choi, K. N. Kim, and S. H. Chung. Autoignited laminar lifted flames of propane in coflow jets with tribrachial edge and mild combustion. *Combust. Flame*, 156(2):396–404, 2009.
- [17] S. H. Chung. Stabilization, propagation and instability of tribrachial triple flames. *Proc. Combust. Inst.*, 31(1):877–892, 2007.
- [18] H. K. Ciezki and G. Adomeit. Shock-tube investigation of self-ignition of *n*-heptane-air mixtures under engine relevant conditions. *Combust. Flame*, 93(4):421–433, 1993.
- [19] S. D. Cohen, A. C. Hindmarsh, and P. F. Dubois. CVODE, a stiff/nonstiff ODE solver in C. *Comput. Phys.*, 10(2):138–143, 1996.
- [20] A. W. Cook and J. J. Riley. A subgrid model for equilibrium chemistry in turbulent flows. *Phys. Fluids*, 6:2868–2870, 1994.
- [21] H. J. Curran, S. L. Fischer, and F. L. Dryer. Reaction kinetics of dimethyl ether. II: low-temperature oxidation in flow reactors. *Int. J. Chem. Kinet.*, 32(12):741–759, 2000.
- [22] H. J. Curran, W. J. Pitz, C. K. Westbrook, P. Dagaut, J.-C. Boettner, and M. Cathonnet. A wide range modeling study of dimethyl ether oxidation. *Int. J. Chem. Kinet.*, 30(3):229–241, 1998.
- [23] P. Dagaut, M. Reuillon, and M. Cathonnet. Experimental study of the oxidation of *n*-heptane in a jet stirred reactor from low to high temperature and pressures up to 40 atm. *Combust. Flame*, 101:132–140, 1995.

- [24] B. B. Dally, D. F. Fletcher, and A. R. Masri. Flow and mixing fields of turbulent bluff-body jets and flames. *Combust. Theor. Model.*, 2:193–219, 1998.
- [25] B. B. Dally, A. R. Masri, R. S. Barlow, and G. J. Fiechtner. Instantaneous and mean compositional structure of bluff-body stabilized nonpremixed flames. *Combust. Flame*, 114:119–148, 1998.
- [26] B. B. Dally, A. R. Masri, R. S. Barlow, G. J. Fiechtner, and D. F. Fletcher. Measurements of NO in turbulent non-premixed flames stabilized on a bluff body. *Proc. Combust. Inst.*, 26:2191–2197, 1996.
- [27] H. Davy. Some new experiments and observations on the combustion of gaseous mixtures, with an account of a method of preserving a continued light in mixtures of inflammable gases and air without flame. *Philos. Trans. R. Soc. Lond.*, 107:77–86, 1817.
- [28] P. Dearden and R. Long. Soot formation in ethylene and propane diffusion flames. *J. Appl. Chem.*, 18:243–251, 1968.
- [29] O. Desjardins, G. Blanquart, G. Balarac, and H. Pitsch. High order conservative finite difference scheme for variable density low Mach number turbulent flows. *J. Comput. Phys.*, 227(15):7125–7159, 2008.
- [30] H. Di, X. He, P. Zhang, Z. Wang, M. S. Wooldridge, C. K. Law, C. Wang, S. Shuai, and J. Wang. Effects of buffer gas composition on low temperature ignition of *iso*-octane and *n*-heptane. *Combust. Flame*, 161:2531–2538, 2014.
- [31] G. Dixon-Lewis, T. David, P. H. Gaskell, S. Fukutani, H. Jinno, J. A. Miller, R. J. Kee, M. D. Smooke, N. Peters, E. Effelsberg, J. Warnatz, and F. Behrendt. Calculation of the structure and extinction limit of a methane-air counterflow diffusion flame in the forward stagnation region of a porous cylinder. *Proc. Combust. Inst.*, 20:1893–1904, 1985.
- [32] J. W. Dold. Flame propagation in a nonuniform mixture: Analysis of a slowly varying Triple Flame. *Combust. Flame*, 76(1):71–88, 1989.
- [33] K. Donaldson, L. Tran, L. A. Jimenz, R. Duffin, D. E. Newby, N. Mills, W. MacNee, and V. Stone. Combustion-derived nanoparticles: A review of their toxicology following inhalation exposure. *Part. Fibre Toxicol.*, 2:1–14, 2005.
- [34] D. X. Du, R. L. Axelbaum, and C. K. Law. Experiments on the sooting limits of aerodynamically-strained diffusion flames. *Proc. Combust. Inst.*, 22:387–394, 1989.
- [35] D. X. Du, R. L. Axelbaum, and C. K. Law. The influence of carbon dioxide and oxygen as additives on soot formation in diffusion flames. *Proc. Combust. Inst.*, 23:1501–1507, 1991.

- [36] D. X. Du, R. L. Axelbaum, and C. K. Law. Soot formation in strained diffusion flames with gaseous additives. *Comb. Flame*, 102:11–20, 1995.
- [37] S. B. Dworkin, B. C. Connelly, A. M. Schaffer, B.A. V. Bennett, M. B. Long, M. D. Smooke, M. P. Puccio, B. McAndrews, and J. H. Miller. Computational and experimental study of a forced, time-dependent, methane-air coflow diffusion flame. *Proc. Combust. Inst.*, 31:971–978, 2007.
- [38] H. El-Asrag and S. Menon. Large eddy simulation of soot formation in a turbulent nonpremixed jet flame. *Combust. Flame*, 156:385–395, 2009.
- [39] T. I. Farouk, M. C. Hicks, and F. L. Dryer. Multistage oscillatory "cool flame" behavior for isolated alkane droplet-combustion in elevated pressure microgravity condition. *Proc. Combust. Inst.*, 35:1701–1708, 2015.
- [40] Q. Feng, A. Jalali, A. M. Fincham, Y. L. Wang, T. T. Tsotsis, and F. N. Egolfopoulos. Soot formation in flames of model biodiesel fuels. *Combust. Flame*, 159:1876–1893, 2012.
- [41] S. L. Fischer, F. L. Dryer, and H. J. Curran. Reaction kinetics of dimethyl ether. I: high-temperature pyrolysis and oxidation in flow reactors. *Int. J. Chem. Kinet.*, 32(12):713–740, 2000.
- [42] C. G. Fotache, T. G. Kreutz, D. L. Zhu, and C. K. Law. An Experimental Study of Ignition in Nonpremixed Counterflowing Hydrogen versus Heated Air. *Combust. Sci. Technol.*, 109:373–393, 1995.
- [43] C. G. Fotache, C. J. Sung, and C. K. Law. Mild oxidation regimes and multiple criticality in nonpremixed hydrogen-air counterflow. *Combust. Flame*, 112:457–471, 1998.
- [44] M. Frenklach and S. J. Harris. Aerosol dynamics modeling using the method of moments. *J. Coll. Int. Sci.*, 118:252–261, 1987.
- [45] M. Frenklach and H. Wang. Detailed modeling of soot particle nucleation and growth. *Proc. Combust. Inst.*, 23:1559–1566, 1991.
- [46] S. K. Friedlander. *Smoke, Dust, and Haze: Fundamentals of Aerosol Dynamics*. Oxford University Press, New York, 2000.
- [47] P. J. M. Frijters and R. S. G. Baert. Oxygenated fuels for clean heavy-duty diesel engines. *Int. J. Veh. Des.*, 41:242–255, 2006.
- [48] S. Gail, S. M. Sarathy, M. J. Thomson, P. Diévert, and P. Dagaut. Experimental and chemical kinetic modeling study of small methyl esters oxidation: Methyl(e)-2-butenoate and methyl butanoate. *Combust. Flame*, 155:635–650, 2008.
- [49] A. G. Gaydon. *The Spectroscopy of Flames*. Chapman and Hall, 1974.

- [50] M. Germano, U. Piomelli, P. Moin, and W. H. Cabot. A dynamic subgrid-scale eddy viscosity model. *Phys. Fluids A*, 3:1760–1765, 1991.
- [51] S. Ghosal and L. Vervisch. Theoretical and numerical study of a symmetrical triple flame using the parabolic flame path approximation. *J. Fluid Mech.*, 415:227–260, 2000.
- [52] V. Giovangigli and M. D. Smooke. Calculation of extinction limits for premixed laminar flames in a stagnation point flow. *J. Comput. Phys.*, 68(2):327–345, 1987.
- [53] M. S. Graboski and R. L. McCormick. Combustion of fat and vegetable oil derived fuels in diesel engines. *Prog. Energy Combust.*, 24:125–164, 1998.
- [54] J. F. Griffiths, J. P. MacNamara, C. G. W. Sheppard, D. A. Turton, and B. J. Whitaker. The relationship of knock during controlled autoignition to temperature inhomogeneities and fuel reactivity. *Fuel*, 81:2219–2225, 2002.
- [55] J. F. Griffiths and S. K. Scott. Thermokinetic interactions: fundamentals of spontaneous ignition and cool flames. *Prog. Energy Combust. Sci.*, 13:161–197, 1987.
- [56] W. L. Grosshandler. RADCAL: A narrow-band model for radiation calculations in a combustion environment. *NIST technical note*, 1402, 1993.
- [57] Ö. L. Gülder, D. R. Snelling, and R. A. Sawchuk. Influence of hydrogen addition to fuel on temperature field and soot formation in diffusion flames. *Proc. Combust. Inst.*, 26:2351–2358, 1996.
- [58] H. Guo, F. Liu, G. J. Smallwood, and Ö. L. Gülder. Numerical study on the influence of hydrogen addition on soot formation in a laminar ethylene-air diffusion flame. *Combust. Flame*, 145:324–338, 2006.
- [59] L. J. Hartley and J. W. Dold. Flame propagation in a nonuniform mixture: Analysis of a propagating triple-flame. *Combust. Sci. Technol.*, 80(1-3):23–46, 1991.
- [60] M. Herrmann, G. Blanquart, and V. Raman. Flux corrected finite volume scheme for preserving scalar boundedness in reacting large-eddy simulations. *AIAA J.*, 44:2879–2886, 2006.
- [61] J. Herzler, L. Jerig, and P. Roth. Shock tube study of the ignition of lean *n*-heptane/air mixtures at intermediate temperatures and high pressures. *Proc. Combust. Inst.*, 30:1147–1153, 2005.
- [62] W. Hwang, J. Dec, and M. Sjoberg. Spectroscopic and chemical-kinetic analysis of the phases of HCCI autoignition and combustion for single- and two-stage ignition fuels. *Combust. Flame*, 154:387–409, 2008.

- [63] M. Ihme and H. Pitsch. Modeling of radiation and nitric oxide formation in turbulent nonpremixed flames using a flamelet/progress variable formulation. *Phys. Fluids*, 20:055110, 2008.
- [64] M. Ihme and H. Pitsch. Prediction of extinction and reignition in nonpremixed turbulent flames using a flamelet/progress variable model. 2. Application in LES of sandia flames D and E. *Combust. Flame*, 155:90–107, 2008.
- [65] H. G. Im and J. H. Chen. Structure and propagation of triple flames in partially premixed hydrogen-air mixtures. *Combust. Flame*, 119:436–454, 1999.
- [66] E. J. Jensen and O. B. Toon. The potential impact of soot particles from aircraft exhaust on cirrus clouds. *Geophys. Res. Lett.*, 24:249–252, 1997.
- [67] K. A. Jensen, J. M. Suo-Antilla, and L. G. Blevins. Measurement of soot morphology, chemistry, and optical properties in the visible and near-infrared spectrum in the flame zone and overfire region of large JP-8 pool fires. *Combust. Sci. Technol.*, 179:2453–2487, 2007.
- [68] Y. Ju, J. K. Lefkowitz, C. B. Reuter, S. H. Won, X. Yang, S. Yang, W. Sun, Z. Jiang, and Q. Chen. Plasma assisted low temperature combustion. *Plasma Chem. Plasma Process*, 36:85–105, 2016.
- [69] P. N. Kīoni, K. N. C. Bray, D. A. Greenhalgh, and B. Rogg. Experimental and numerical studies of a triple flame. *Combust. Flame*, 116(1-2):192–206, 1999.
- [70] E. W. Kaiser, T. J. Wailington, M. D. Hurley, J. Platz, H. J. Curran, W. J. Pitz, C. K. Westbrook, and T. J. Wallington. Experimental and modeling study of premixed atmospheric-pressure dimethyl ether-air flames. *J. Phy. Chem. A*, 104(35):8194–8206, 2000.
- [71] A. Kazakov, H. Wang, and M. Frenklach. Detailed modeling of soot formation in laminar premixed ethylene flames at a pressure of 10 bar. *Combust. Flame*, 100:111–120, 1995.
- [72] R. J. Kee, F. M. Rupley, and J. A. Miller. A Fortran computer code package for the evaluation of gas-phase viscosities, conductivities, and diffusion coefficients, Report No. SAND 83-8209, Sandia National Laboratories, 1983.
- [73] R. J. Kee, F. M. Rupley, and J. A. Miller. CHEMKIN-II A Fortran chemical kinetics package for the analysis of gas phase chemical kinetics, Report No. SAND 89-8009B, Sandia National Laboratories, 1989.
- [74] R. J. Kee, F. M. Rupley, and J. A. Miller. CHEMKIN Collection, Release 3.6, Reaction Design, Inc., San Diego, CA, 2000.
- [75] S. Kikui, T. Kamada, H. Nakamura, T. Tezuka, S. Hasegawa, and K. Maruta. Characteristics of *n*-butane weak flames at elevated pressures in a micro flow reactor with a controlled temperature profile. *Proc. Combust. Inst.*, 35:3405–3412, 2015.

- [76] M. K. Kim, S. H. Won, and S. H. Chung. Effect of velocity gradient on propagation speed of tribrachial flames in laminar coflow jets. *Proc. Combust. Inst.*, 31(1):901–908, 2007.
- [77] D. N. Koert, D. L. Miller, and N. P. Cernansky. Experimental studies of propane oxidation through the negative temperature coefficient region at 10 and 15 atmospheres. *Combust. Flame*, 96:34–49, 1994.
- [78] S. L. Kokjohn, R. M. Hanson, D. A. Splitter, and R. D. Reitz. Fuel reactivity controlled compression ignition (RCCI): a pathway to controlled high-efficiency clean combustion. *Int. J. Engine Res.*, 12:209–226, 2011.
- [79] T. G. Kreutz, M. Nishioka, and C. K. Law. The role of kinetic versus thermal feedback in nonpremixed ignition of hydrogen versus heated air. *Combust. Flame*, 99(3-4):758–766, 1994.
- [80] A. Krisman, E. R. Hawkes, M. Talei, A. Bhagatwala, and J. H. Chen. Polybrachial structures in dimethyl ether edge-flames at negative temperature coefficient conditions. *Proc. Combust. Inst.*, 35:999–1006, 2015.
- [81] C. K. Law. *Combustion Physics*. Cambridge University Press, New York, 2006.
- [82] C. K. Law and P. Zhao. NTC-affected ignition in nonpremixed counterflow. *Combust. Flame*, 159(3):1044–1054, 2012.
- [83] B. J. Lee and S. H. Chung. Stabilization of lifted tribrachial flames in a laminar nonpremixed jet. *Combust. Flame*, 109(1-2):163–172, 1997.
- [84] S.-Y. Lee, S. R. Turns, and R. J. Santoro. Measurements of soot, OH, and PAH concentrations in turbulent ethylene/air jet flames. *Combust. Flame*, 156:2264–2275, 2009.
- [85] D. O. Lignell, J. H. Chen, and P. J. Smith. Three-dimensional direct numerical simulation of soot formation and transport in a temporally evolving nonpremixed ethylene jet flame. *Combust. Flame*, 155:316–333, 2008.
- [86] D. O. Lignell, J. H. Chen, P. J. Smith, T. Lu, and C. K. Law. The effect of flame structure on soot formation and transport in turbulent nonpremixed flames using direct numerical simulation. *Combust. Flame*, 151(1-2):2–28, 2007.
- [87] W. Liu, A. P. Kelley, and C. K. Law. Flame propagation and counterflow nonpremixed ignition of mixtures of methane and ethylene. *Combust. Flame*, 157(5):1027–1036, 2010.
- [88] W. Liu, A. P. Kelley, and C. K. Law. Non-premixed ignition, laminar flame propagation, and mechanism reduction of *n*-butanol, *iso*-butanol, and methyl butanoate. *Proc. Combust. Inst.*, 33:995–1002, 2011.

- [89] W. Liu, J. A. Koch, and C. K. Law. Nonpremixed ignition of C<sub>7</sub>-C<sub>16</sub> normal alkanes in stagnating liquid pool. *Combust. Flame*, 158:2145–2148, 2011.
- [90] W. Liu, C. K. Law, and T. F. Lu. Multiple criticality and staged ignition of methane in the counterflow. *Int. J. Chem. Kinet.*, 41(12):764–776, 2009.
- [91] W. Liu, D. Zhu, N. Wu, and C. K. Law. Ignition of *n*-heptane pool by heated stagnating oxidizing flow. *Combust. Flame*, 157:259–266, 2010.
- [92] X. Liu, S. Osher, and T. Chan. Weighted Essentially Non-oscillatory Schemes. *J. Comput. Phys.*, 115(1):200–212, 1994.
- [93] T. Lu and C. K. Law. Toward accommodating realistic fuel chemistry in large-scale computations. *Prog. Energy Combust. Sci.*, 35:192–215, 2009.
- [94] T. F. Lu, C. S. Yoo, J. H. Chen, and C. K. Law. Three-dimensional direct numerical simulation of a turbulent lifted hydrogen jet flame in heated coflow: a chemical explosive mode analysis. *J. Fluid Mech.*, 652:45–64, 2010.
- [95] X. Lu, D. Han, and Z. Huang. Fuel design and management for the control of advanced compression-ignition combustion modes. *Prog. Energy Combust. Sci.*, 37:741–783, 2011.
- [96] D. L. Marchisio and R. O. Fox. Solution of population balance equations using the Direct Quadrature Method of Moments. *J. Aerosol Sci.*, 36:43–73, 2005.
- [97] C. S. McEnally and L. D. Pfefferle. Fuel decomposition and hydrocarbon growth processes for oxygenated hydrocarbons: butyl alcohols. *Proc. Combust. Inst.*, 30:1363–1370, 2005.
- [98] C. S. McEnally and L. D. Pfefferle. Sooting tendencies of oxygenated hydrocarbons in laboratory-scale flames. *Environ. Sci. Technol.*, 45:2498–2503, 2011.
- [99] C. Meneveau, T. S. Lund, and W. H. Cabot. A Lagrangian dynamic subgrid-scale model of turbulence. *J. Fluid Mech.*, 319:353–385, 1996.
- [100] P. Mitchell and M. Frenklach. Monte Carlo simulation of soot aggregation with simultaneous surface growth: Why primary particles appear spherical. *Proc. Combust. Inst.*, 27:1507–1514, 1998.
- [101] P. Mitchell and M. Frenklach. Particle aggregation with simultaneous surface growth. *Phys. Rev. E*, 67:061407–1–061407–11, 2003.
- [102] G. Mittal, M. Chaos, C. J. Sung, and F. L. Dryer. Dimethyl ether autoignition in a rapid compression machine: Experiments and chemical kinetic modeling. *Fuel Process. Technol.*, 89:1244–1254, 2008.
- [103] R. K. Mohammed, M. A. Tanoff, M. D. Smooke, A. M. Schaffer, and M. B. Long. Computational and experimental study of a forced, timevarying, axisymmetric, laminar diffusion flame. *Proc. Combust. Inst.*, 27:693–702, 1998.

- [104] M. E. Mueller, G. Blanquart, and H. Pitsch. Hybrid Method of Moments for modeling soot formation and growth. *Combust. Flame*, 156:1143–1155, 2009.
- [105] M. E. Mueller, G. Blanquart, and H. Pitsch. A joint Volume-Surface model of soot aggregation with the method of moments. *Proc. Combust. Inst.*, 32:785–792, 2009.
- [106] M. E. Mueller, G. Blanquart, and H. Pitsch. Modeling the oxidation-induced fragmentation of soot aggregates in laminar flames. *Proc. Combust. Inst.*, 33:667–674, 2011.
- [107] M. E. Mueller, Q. N. Chan, N. H. Qamar, Bassam Dally, and H. Pitsch. Experimental and computational study of soot evolution in a turbulent nonpremixed bluff body ethylene flame. *Combust. Flame*, 160:1298–1309, 2013.
- [108] M. E. Mueller and H. Pitsch. LES subfilter modeling of soot-turbulence interactions. *Phys. Fluids*, 23:115104, 2011.
- [109] M. E. Mueller and H. Pitsch. LES model for sooting turbulent nonpremixed flames. *Combust. Flame*, 159:2166–2180, 2012.
- [110] K. Narayanaswamy, G. Blanquart, and H. Pitsch. A consistent chemical mechanism for oxidation of substituted aromatic species. *Combust. Flame*, 157:1879–1898, 2010.
- [111] V. Nayagam, D. L. Dietrich, P. V. Ferkul, M. C. Hicks, and F. A. Williams. Can cool flames support quasi-steady alkane droplet burning? *Combust. Flame*, 159:3583–3588, 2012.
- [112] V. Nayagam, D. L. Dietrich, M. C. Hicks, and F. A. Williams. Cool-flame extinction during *n*-alkane droplet combustion in microgravity. *Combust. Flame*, 162:2140–2147, 2015.
- [113] K. G. Neoh, J. B. Howard, and A. F. Sarofim. Soot oxidation in flames. In *Particulate Carbon Formation during Combustion*, pages 162–282. Plenum Press, 1981.
- [114] U. Niemann, R. Seiser, and K. Seshadri. Ignition and extinction of low molecular weight esters in nonpremixed flows. *Combust. Theory Model.*, 14:875–891, 2010.
- [115] M. Nishioka, C. K. Law, and T. Takeno. A flame-controlling continuation method for generating S-curve responses with detailed chemistry. *Combust. Flame*, 104:328–342, 1996.
- [116] Y. Ohta and M. Furutani. Identification of cool and blue flames in compression ignition. *Arch. Combust.*, 11:43–52, 1991.
- [117] S. H. Park and S. N. Rogak. A one-dimensionalmodel for coagulation, sintering, and surface growth of aerosol agglomerates. *Aerosol Sci. Tech.*, 37:947–960, 2003.

- [118] P. Pepiot, H. Pitsch, R. Malhotra, S. R. Kirby, and A. L. Boehman. Structure group analysis for soot reduction tendency of oxygenated fuels. *Combust. Flame*, 154:191–205, 2008.
- [119] N. Peters. *Turbulent Combustion*. Cambridge University Press, 2000.
- [120] C. D. Pierce. *Progress-variable Approach for Large-Eddy Simulation of Turbulent Combustion*. PhD thesis, Stanford University, 2001.
- [121] H. Pitsch. FlameMaster, A C++ computer program for 0D combustion and 1D laminar flame calculations.
- [122] H. Pitsch, M. Chen, and N. Peters. Unsteady flamelet modeling of turbulent hydrogen-air diffusion flames. *Proc. Combust. Inst.*, 27(1):1057–1064, 1998.
- [123] H. Pitsch and N. Peters. A consistent flamelet formulation for non-premixed combustion considering differential diffusion effects. *Combust. Flame*, 114(1–2):26–40, 1998.
- [124] T. Plessing, P. Terhoeven, N. Peters, and M. S. Mansour. An experimental and numerical study of a laminar triple flame. *Combust. Flame*, 115(3):335–353, 1998.
- [125] B. E. Poling, J. M. Prausnitz, and J. P. O’Connell. *The Properties of Gases and Liquids*. McGraw-Hill, New York, Fifth edition, 2000.
- [126] S. B. Pope. The evolution of surfaces in turbulence. *Int. J. Eng. Sci.*, 26(5):445–469, 1988.
- [127] N. H. Qamar, Z. T. Alwahabi, Q. N. Chan, G. J. Nathan, D. Roekaerts, and K. D. King. Soot volume fraction in a piloted turbulent jet non-premixed flame of natural gas. *Combust. Flame*, 156:1339–1347, 2009.
- [128] N. H. Qamar, G. J. Nathan, Z. T. Alwahabi, and K. D. King. The effect of global mixing on soot volume fraction: measurement in simple jet, precessing jet, and bluff body flames. *Proc. Combust. Inst.*, 30:1493–1500, 2005.
- [129] X. Qin and Y. Ju. Measurements of burning velocities of dimethyl ether and air premixed flames at elevated pressures. *Proc. Combust. Inst.*, 30:233–240, 2005.
- [130] G. R. Ruetsch, L. Vervisch, and A. Liñán. Effects of heat release on triple flames. *Phys. Fluids*, 7(6):1447, 1995.
- [131] M. Sánchez-Sanz, B. A. V. Bennett, M. D. Smooke, and A. Liñán. Influence of Strouhal number on pulsating methane-air coflow jet diffusion flames. *Combust. Theory Modell.*, 14:453–478, 2010.
- [132] S. M. Sarathy, M. J. Thomson, C. Togbé, P. Dagaut, F. Halter, and C. Mounaim-Rousselle. An experimental and kinetic modeling study of *n*-butanol combustion. *Combust. Flame*, 156:852–864, 2009.

- [133] C. A. Schuetz and M. Frenklach. Nucleation of soot: molecular dynamics simulations of pyrene dimerization. *Proc. Combust. Inst.*, 29:2307–2314, 2002.
- [134] C. Schulz, B. F. Kock, M. Hofmann, H. Michelsen, S. Will, B. Bougie, R. Suntz, and G. Smallwood. Laser-induced incandescence: recent trends and current questions. *Appl. Phys. B*, 83:333–354, 2006.
- [135] J. H. Seinfeld and S. N. Pandis. *Atmospheric Chemistry and Physics: From Air Pollution to Climate Change*. John Wiley & Sons, New York, 1998.
- [136] R. Seiser, H. Pitsch, K. Seshadri, W. J. Pitz, and H. J. Curran. Extinction and autoignition of n-heptane in counterflow configuration. *Proc. Combust. Inst.*, 28:2029–2037, 2000.
- [137] K. Seshadri, S. Humer, and R. Seiser. Activation-energy asymptotic theory of autoignition of condensed hydrocarbon fuels in non-premixed flows with comparison to experiment. *Combust. Theory Model.*, 12:831–855, 2008.
- [138] C. R. Shaddix, J. E. Harrington, and K. C. Smyth. Quantitative measurements of enhanced soot production in a flickering methan/air diffusion flame. *Combust. Flame*, 99:723–732, 1994.
- [139] R. Shan, C. S. Yoo, J. H. Chen, and T. Lu. Computational diagnostics for n-heptane flames with chemical explosive mode analysis. *Combust. Flame*, 159(10):3119–3127, 2012.
- [140] R. S. Sheinson and F. W. Williams. Chemiluminescence spectra from cool and blue flames: Electronically excited formaldehyde. *Combust. Flame*, 21(2):221–230, 1973.
- [141] E. J. Silke, H. J. Curran, and J. M. Simmie. The influence of fuel structure on combustion as demonstrated by the isomers of heptane: a rapid compression machine study. *Proc. Combust. Inst.*, 30:2639–2647, 2005.
- [142] R. R. Skaggs and J. H. Miller. Tunable diode laser absorption measurement of carbon monoxide and temperature in a time-varying methane-air non-premixed flame. *Proc. Combust. Inst.*, 26:1181–1188, 1996.
- [143] M. D. Smooke, I. K. Puri, and K. Seshadri. A comparison between numerical calculations and experimental measurements of the structure of a counterflow diffusion flame burning diluted methane in diluted air. *Proc. Combust. Inst.*, 21:1783–1792, 1988.
- [144] A. W. Strawa and B. J. Cantwell. Investigation of an excited jet diffusion flame at elevated pressure. *J. Fluid Mech.*, 200:309–336, 1989.
- [145] Z. W. Sun, Z. T. Alwahabi, D. H. Gu, S. M. Mahmoud, G. J. Nathan, and B. B. Dally. Planar laser-induced incandescence of turbulent soot flames: the influence of beam steering and signal trapping. *Appl. Phys. B*, 119:731–743, 2015.

- [146] J. E. Temme, P. M. Allison, and J. F. Driscoll. Low frequency combustion instabilities imaged in a gas turbine combustor flame tube. *50th AIAA Aerospace Sciences Meeting*, AIAA 2012-0542.
- [147] P. A. Tesner. Formation of dispersed carbon by thermal decomposition of hydrocarbons. *Proc. Combust. Inst.*, 7:546–553, 1958.
- [148] H. Tsuji and I. Yamaoka. Structure analysis of counterflow diffusion flames in the forward stagnation region of a porous cylinder. *Proc. Combust. Inst.*, 13:723–731, 1971.
- [149] U. Vandsburger, I. M. Kennedy, and I. Glassman. Sooting counter-flow diffusion flames with varying velocity gradients. *Proc. Combust. Inst.*, 20:1105–1112, 1985.
- [150] S. S. Vasu, D. F. Davidson, and R. K. Hanson. Jet fuel ignition delay times: shock tube experiments over wide conditions and surrogate model predictions. *Combust. Flame*, 152:125–143, 2008.
- [151] P. S. Veloo, P. Dagaut, C. Togbe, G. Dayma, S. M. Sarathy, C. K. Westbrook, and F. N. Egolfopoulos. Jet-stirred reactor and flame studies of propanal oxidation. *Proc. Combust. Inst.*, 34(1):599–606, 2013.
- [152] L. Waldmann and K. H. Schmitt. Thermophoresis and diffusiophoresis of aerosols. In C. N. Davies, editor, *Aerosol Science*. Academic Press, 1966.
- [153] H. Wang. Formation of nascent soot and other condensed-phase materials in flames. *Proc. Combust. Inst.*, 33:41–67, 2011.
- [154] Y. Wang and S. H. Chung. Effect of strain rate on sooting limits in counterflow diffusion flames of gaseous hydrocarbon fuels: Sooting temperature index and sooting sensitivity index. *Combust. Flame*, 161:1224–1234, 2014.
- [155] Y. L. Wang, Q. Feng, F. N. Egolfopoulos, and T. T. Tsotsis. Studies of C<sub>4</sub> and C<sub>10</sub> ester flames. *Combust. Flame*, 158:1507–1519, 2011.
- [156] C. K. Westbrook. Chemical kinetics of hydrocarbon ignition in practical combustion systems. *Proc. Combust. Inst.*, 28:1563–1577, 2000.
- [157] C. K. Westbrook, W. J. Pitz, and H. J. Curran. Chemical kinetic modeling study of the effects of oxygenated hydrocarbons on soot emissions from diesel engines. *J. Phys. Chem. A*, 110:6912–6922, 2006.
- [158] S. H. Won, B. Jiang, P. Dievart, C. H. Sohn, and Y. Ju. Self-sustaining *n*-heptane cool diffusion flames activated by ozone. *Proc. Combust. Inst.*, 35:881–888, 2015.

- [159] D. Wong, C. A. Schuetz, and M. Frenklach. Molecular dynamics of PAH dimerization. In H. Bockhorn, A. D'Anna, A. Sarofim, and H. Wang, editors, *Combustion Generated Fine Carbonaceous Particles*, pages 247–257. KIT Scientific Publishing, 2009.
- [160] Y. Xuan and G. Blanquart. Effects of aromatic chemistry-turbulence interactions on soot formation in a turbulent non-premixed flame. *Proc. Combust. Inst.*, 35:1911–1919, 2015.
- [161] C. S. Yoo and H. G. Im. Transient soot dynamics in turbulent nonpremixed ethylene-air counterflow flames. *Proc. Combust. Inst.*, 31:701–708, 2007.
- [162] C. S. Yoo, Z. Luo, T. Lu, H. Kim, and J. H. Chen. A DNS study of ignition characteristics of a lean *iso*-octane/air mixture under HCCI and SACI conditions. *Proc. Combust. Inst.*, 34:2985–2993, 2013.
- [163] C. S. Yoo, R. Sankaran, and J. H. Chen. Three-dimensional direct numerical simulation of a turbulent lifted hydrogen jet flame in heated coflow: flame stabilization and structure. *J. Fluid Mech.*, 640:453–481, 2009.
- [164] J. Zhang, C. R. Shaddix, and R. W. Schefer. Design of "model-friendly" turbulent non-premixed jet burners for  $C_{2+}$  hydrocarbon fuels. *Rev. Sci. Instrum.*, 82:074101, 2011.
- [165] B. Zhao, Z. Yang, M. V. Johnston, and H. Wang. Particle size distribution function of incipient soot in laminar premixed ethylene flames: Effect of flame temperature. *Proc. Combust. Inst.*, 30:1441–1448, 2005.
- [166] H. Zhao, R. Stone, and B. Williams. Investigation of the soot formation in ethylene laminar diffusion flames when diluted with helium or supplemented by hydrogen. *Energy Fuels*, 28:2144–2151, 2014.
- [167] P. Zhao and C. K. Law. The role of global and detailed kinetics in the first-stage ignition delay in NTC-affected phenomena. *Combust. Flame*, 160(11):2352–2358, 2013.
- [168] P. Zhao, W. Liang, S. Deng, and C. K. Law. Initiation and propagation of laminar premixed cool flames. *Fuel*, 166:477–487, 2016.
- [169] Z. Zhao, M. Chaos, A. Kazakov, and F. L. Dryer. Thermal decomposition reaction and a comprehensive kinetic model of dimethyl ether. *Int. J. Chem. Kinet.*, 40(1):1–18, 2008.
- [170] X. L. Zheng. *Studies on ignition of hydrogen and hydrocarbons*. PhD thesis, Princeton University, USA, 2006.
- [171] X. L. Zheng, T. F. Lu, C. K. Law, C. K. Westbrook, H. J. Curran, T. Berces, and F. L. Dryer. Experimental and computational study of nonpremixed ignition of dimethyl ether in counterflow. *Proc. Combust. Inst.*, 30:1101–1109, 2005.